UNIVERSIDADE FEDERAL DE MINAS GERAIS
Instituto de Ciências Exatas (ICEx)
Programa de pós-graduação em Física

Lucas Felipe Bezerra de Melo Oliveira

THEORY, EXPERIMENT, AND FUNDAMENTAL ASPECTS OF QUANTUM STATE DISCRIMINATION WITH FIXED RATES OF INCONCLUSIVE OUTCOMES

Belo Horizonte

2025

Lucas Felipe Bezerra de Melo Oliveira

THEORY, EXPERIMENT, AND FUNDAMENTAL ASPECTS OF QUANTUM STATE DISCRIMINATION WITH FIXED RATES OF INCONCLUSIVE OUTCOMES

Tese apresentada ao Departamento de Física do Instituto de Ciências Exatas da Universidade Federal de Minas Gerais, como requisito parcial para a obtenção do grau de Doutor em Ciências, na área de concentração Física.

Orientador: Leonardo Teixeira Neves

Belo Horizonte

2025

Dados Internacionais de Catalogação na Publicação (CIP)

O48t Oliveira, Lucas Felipe Bezerra de Melo.
Theory, experiment, and fundamental aspects of quantum state discrimination with fixed rates of inconclusive outcomes / Lucas Felipe Bezerra de Melo Oliveira. – 2025.
126 f. : il.

Orientador: Leonardo Teixeira Neves.
Tese (doutorado) – Universidade Federal de Minas Gerais, Departamento de Física.
Bibliografia: f. 108-118.

1. Mecânica quântica. 2. Coerência. 3. Dualidade. I. Título. II. Neves, Leonardo Teixeira. III. Universidade Federal de Minas Gerais, Departamento de Física.

CDU – 530.145 (043)

Ficha catalográfica elaborada por Romário Martins Ribeiro – CRB6 3595
Biblioteca Professor Manoel Lopes de Siqueira – Departamento de Física - UFMG

UNIVERSIDADE FEDERAL DE MINAS GERAIS

INSTITUTO DE CIÊNCIAS EXATAS

PROGRAMA DE PÓS-GRADUAÇÃO EM FÍSICA

FOLHA DE APROVAÇÃO

A presente tese, intitulada **"Theory, experiment, and fundamental aspects of quantum state discrimination with fixed rates of inconclusive outcomes",** de autoria de **LUCAS FELIPE BEZERRA DE MELO OLIVEIRA** submetida à Comissão Examinadora, abaixo-assinada, foi aprovada para obtenção do grau de **DOUTOR EM CIÊNCIAS, área de concentração Física,** em 21 de agosto de 2025.

Belo Horizonte, 21 de agosto de 2025.

Prof. Leonardo Teixeira Neves
Orientador do estudante
Departamento de Física /UFMG

Prof. Sebastião José Nascimento de Pádua
Departamento de Física /UFMG

Prof. Reinaldo Oliveira Vianna
Departamento de Física /UFMG

Prof. José Augusto Oliveira Huguenin
Departamento de Física/UFF

Prof. Jonas Maziero
Departamento de Física/UFSM

Documento assinado eletronicamente por **Jonas Maziero**, **Usuário Externo**, em 22/08/2025, às 10:58, conforme horário oficial de Brasília, com fundamento no art. 5º do Decreto nº 10.543, de 13 de novembro de 2020.

Documento assinado eletronicamente por **Reinaldo Oliveira Vianna**, **Professor do Magistério Superior**, em 22/08/2025, às 16:08, conforme horário oficial de Brasília, com fundamento no art. 5º do Decreto nº 10.543, de 13 de novembro de 2020.

Documento assinado eletronicamente por **Leonardo Teixeira Neves**, **Professor do Magistério Superior**, em 25/08/2025, às 10:27, conforme horário oficial de Brasília, com fundamento no art. 5º do Decreto nº 10.543, de 13 de novembro de 2020.

Documento assinado eletronicamente por **José Augusto Oliveira Huguenin**, **Usuário Externo**, em 27/08/2025, às 06:57, conforme horário oficial de Brasília, com fundamento no art. 5º do Decreto nº 10.543, de 13 de novembro de 2020.

Documento assinado eletronicamente por **Sebastião Jose Nascimento de Padua**, **Professor(a)**, em 04/09/2025, às 16:52, conforme horário oficial de Brasília, com fundamento no art. 5º do Decreto nº 10.543, de 13 de novembro de 2020.

A autenticidade deste documento pode ser conferida no site https://sei.ufmg.br/sei/controlador_externo.php?acao=documento_conferir&id_orgao_acesso_externo=0, informando o código verificador **4479976** e o código CRC **E9577057**.

Referência: Processo nº 23072.251043/2025-70 SEI nº 4479976

Acknowledgments

É um plano de 10 anos que finalmente chega ao fim. Em 2015, eu elaborei comigo mesmo que me tornaria doutor em Física com 27 anos. Quando concluímos um plano de longo prazo como esse, frequentemente nos pegamos repetindo perguntas como "e agora?". O início dessa história é uma tarde de 2020 na qual conheci o Clube da esquina. Desencadeada por uma epifania musical e suscetível à beleza do imprevisível, uma grande reação em cadeia trouxe-me até Minas. É imensurável o efeito dessa aventura em mim, e a quantidade de lugares e de pessoas que conheci nesse estado que tão bem me acolheu. Ao longo dessa transformação, eu me aproximo cada vez mais de mim mesmo. *For this is all a dream we dreamed one afternoon long ago.*

Sou extremamente grato ao Leo, meu orientador, que me ensinou não apenas física, mas também escrita científica, e sobre o que é ser um pesquisador. Nossas conversas sobre os Beatles e o Clube da esquina continuaram a minha imersão nessa história, contada através de epifanias musicais. Agradeço também à CAPES, pelo auxílio financeiro que me permitiu me dedicar integralmente ao doutorado.

Deixo um agradecimento especial aos amigos da terra original: Emerson, por me chamar para ouvir o vinil do Clube; Humberto, Guto, Juan, Lara e Joana, por virem escrever um verso comigo nessa outra parte do país. À minha namorada, Jenni, agradeço por estar comigo nessa jornada, e por me ajudar a concluí-la. Eu te amo. A minha maior sorte nessa aventura foi ter te conhecido.

"E agora?" A resposta pragmática seria "eu já estou trabalhando", mas a questão é mais filosófica do que isso. Fazendo jus à natureza humana, essa é uma pergunta que não precisa de resposta objetiva além da busca em si. Eu me proponho a sempre estar buscando, até que não precise mais. Me incluo no coro dos Beach boys para repetir que "essas coisas eu serei até morrer". Pois, no fim, somos poeira de estrelas se encontrando em um lugar ao longo do caminho.

E agora?
"Agora tudo é diferente e nada se repete"

Tenho o caminho do que sempre quis
E um saveiro pronto pra partir
Invento o cais
E sei a vez de me lançar.

Cais, Clube da esquina

If you feel safe in the area you're working in, you're not working in the right area. Always go a little further into the water than you feel you're capable of being in. Go a little bit out of your depth. And when you don't feel that your feet are quite touching the bottom, you're just about in the right place to do something exciting.

David Bowie

Abstract

Quantum mechanics forbids deterministic and error-free discrimination of nonorthogonal quantum states in a single-shot measurement. Due to this fundamental limitation, many strategies were devised to optimize the task and later became fundamental tools for quantum information processing. Most of these strategies involve outcomes that can be correct, incorrect, or inconclusive in identifying the state. Our work focuses on a general optimized measurement scheme that minimizes the error probability under the constraint of a *fixed rate of inconclusive outcomes* (FRIO). The optimal FRIO measurement is general in the sense that it encompasses other fundamental strategies as particular cases: at zero inconclusive rate, it reduces to the minimum-error (ME) measurement; at a critical inconclusive rate, it corresponds to optimal unambiguous discrimination (UD) for linearly independent states or to optimal maximum-confidence (MC) measurement for certain linearly dependent states. Between these two extremes, FRIO balances error and inconclusive rates, outperforming ME and UD/MC in their respective limitations.

In this thesis, we explore the theoretical, experimental, and fundamental aspects of the optimal FRIO measurement applied to the discrimination of N equiprobable *symmetric* pure states in any dimension $n \leq N$, a family of states of particular interest in quantum communication. On the theoretical side, we first derive analytical solutions for the strategy in this scenario. We then introduce a *concatenated* FRIO scheme, in which the remaining information from inconclusive outcomes is recovered via ME measurement (for $n > 2$), thereby increasing the overall probability of correct identifications compared to the standard scheme. On the experimental side, we present an optical implementation of the optimal FRIO measurement for $N = 2, 3, 5$, and 7 states of a qubit ($n = 2$) encoded in photonic spatial modes. In addition to successfully demonstrating the FRIO strategy and its extreme cases (ME and UD/MC) for a qubit, we show that our setup can be straightforwardly extended to qudits ($n > 2$). Finally, on the fundamental side, we investigate two distinct aspects. First, we characterize quantum coherence as a resource underlying both standard and concatenated FRIO measurements, and show that this approach has practical applications, particularly in secure quantum communication. Next, we derive entropic wave–particle duality relations for uniform N-path interferometers with symmetric which-way detector states, showing that the ME measurement yields the tightest bound, followed by concatenated and standard FRIO. We further show that the relation is saturated at nontrivial points only when the number of paths is non-prime, and identify the corresponding detector states. Our results bring theoretical and experimental advances to the field of quantum state discrimination and emphasize its importance from both practical and foundational standpoints.

Keywords: Quantum state discrimination · Fixed rate of inconclusive outcomes · Symmetric states · Photonic implementation · Quantum coherence · Wave-particle duality

Resumo

A mecânica quântica proíbe a discriminação determinística e sem erros de estados quânticos não ortogonais em uma única medição. Devido a esta limitação fundamental, muitas estratégias foram concebidas para otimizar a tarefa e posteriormente se tornaram ferramentas fundamentais para o processamento de informação quântica. A maioria destas estratégias envolve resultados que podem ser corretos, incorretos ou inconclusivos na identificação do estado. O enfoque do nosso trabalho é um esquema geral de medição otimizada que minimiza a probabilidade de erro sob a restrição de uma *taxa fixa de resultados inconclusivos* (FRIO). A medição FRIO ótima é geral uma vez que engloba outras estratégias fundamentais como casos particulares: a uma taxa nula de inconclusivos, reduz-se à medição de erro mínimo (ME); a uma taxa crítica de inconclusivos, corresponde à discriminação sem ambiguidade (UD) ótima para estados linearmente independentes ou à medição de máxima confiança (MC) ótima para certos estados linearmente dependentes. Entre estes dois extremos, o FRIO equilibra as taxas de erro e de inconclusivos, superando o ME e o UD/MC nas suas respectivas limitações.

Nesta tese, exploramos os aspectos teóricos, experimentais e fundamentais da medição FRIO ótima aplicada à discriminação de N estados puros *simétricos* equiprováveis em qualquer dimensão $n \leq N$, uma família de estados de particular interesse em comunicação quântica. Do ponto de vista teórico, derivamos soluções analíticas para a estratégia neste cenário. Em seguida, introduzimos um esquema FRIO *concatenado*, no qual a informação remanescente dos resultados inconclusivos é recuperada através da medição ME (para $n > 2$), aumentando assim a probabilidade global de identificações corretas em comparação com o esquema padrão. Do ponto de vista experimental, apresentamos uma implementação óptica da medição FRIO ótima para $N = 2, 3, 5$ e 7 estados de um qubit ($n = 2$) codificado em modos espaciais fotônicos. Além de demonstrar a estratégia FRIO e os seus casos extremos (ME e UD/MC) para um qubit, mostramos que a nossa estratégia pode ser diretamente estendida a qudits ($n > 2$). Finalmente, do ponto de vista fundamental, investigamos dois aspectos distintos. Em primeiro lugar, caracterizamos a coerência quântica como um recurso subjacente às medições FRIO padrão e concatenada, e mostramos que esta abordagem tem aplicações práticas, particularmente na comunicação quântica segura. Em seguida, derivamos relações entrópicas de dualidade onda-partícula para interferômetros uniformes de N caminhos com estados simétricos detetores de caminho, mostrando que a medição ME produz o limite mais restritivo, seguido de FRIO concatenado e padrão. Mostramos ainda que a relação é saturada em pontos não triviais apenas quando o número de caminhos não é primo, e identificamos os estados correspondentes do detector. Os nossos resultados trazem avanços teóricos e experimentais para o campo da discriminação de estados quânticos e enfatizam a sua importância dos pontos de vista prático e fundamental.

Palavras-chave: Discriminação de estados quânticos · Taxa fixa de resultados inconclusivos · Estados simétricos · Implementação fotônica · Coerência quântica · Dualidade onda-partícula

List of Figures

List of Tables

List of abbreviations and acronyms

DFT	Discrete Fourier Transform
FRIO	Fixed Rate of Inconclusive Outcomes
LCD	Liquid Crystal Display
MC	Maximum Confidence
ME	Minimum Error
POVM	Positive Operator-Valued Measure
SLM	Spatial Light Modulator
UD	Unambiguous Discrimination

Contents

Introduction

The problem of quantum state discrimination was introduced in the late 1960s and consists of designing a measurement strategy to optimally determine in which state a quantum system was prepared, given a set $\{\hat{\rho}_j\}$ of possible states with associated *a priori* probabilities $\{\eta_j\}$ [1–3]. If formulated in terms of a sender that transmits a message built from the “alphabet” $\{\hat{\rho}_j\}$ to a receiver that extracts it through measurements, we see that this problem is the essence of quantum communication [4, 5]. Furthermore, as it encompasses the measurement process in quantum theory, it naturally underlies many applications in quantum information processing and quantum foundations [6, 7].

When the quantum states are not mutually orthogonal, quantum theory forbids perfect discrimination between them. In this case, each discrimination strategy optimizes a different figure of merit to manage errors or inconclusive outcomes [6–9]. In the pioneering minimum-error (ME) measurement, each outcome is used to infer the received state and the average error probability is minimized [10–12]. On the other hand, the optimal unambiguous discrimination (UD) strategy enables error-free identifications of linearly independent states, with inconclusive results in a minimum fraction of trials [13–17]. More recently, a strategy analogous to UD was conceived to discriminate linearly dependent states. In the optimal maximum-confidence (MC) measurement [18], one maximizes the probability $P(\hat{\rho}_j|j)$, taken as our *confidence* in associating outcome j to state $\hat{\rho}_j$, and minimizes the rate of inconclusive results.

These state discrimination strategies were shown to be extreme and particular cases of a more general optimized measurement scheme in which the error rate is minimized under the constraint of a *fixed rate of inconclusive outcomes* (FRIO). The optimal FRIO strategy was proposed in Refs. [19, 20], and shown to be a scheme that interpolates between ME and optimal UD measurements. Thereafter, recent works also show that it interpolates between ME and optimal MC measurements when the maximum confidences are the same for all states in the set [21, 22]. In addition to generalizing fundamental discrimination strategies, the optimal FRIO measurement is useful in practical situations. For instance, in a quantum communication scenario where the error and the inconclusive rates must be kept below the levels set by the ME and optimal UD/MC strategies, respectively, the FRIO measurement provides a tunable strategy that balances these rates within desired bounds. Examples of the application of FRIO in this context were given for protocols like quantum teleportation [23] and dense coding [24] with nonmaximally entangled states.

In addition to theoretical progress, several experimental implementations have been carried out over the years. Taking into account only discrete spaces, all extreme discrimination strategies were experimentally demonstrated for two-dimensional quantum states (*qubits*). This includes implementations of the ME measurement for sets of two [25], three, and four [26] states, optimal UD for sets of two states [27, 28], and optimal MC for sets of three states [29]. For higher-dimensional states (*qudits*), demonstrations of ME [30] and optimal UD [31, 32] strategies have also been reported. The optimal FRIO strategy has only recently been implemented for the discrimination of two nonorthogonal qubit states with arbitrary *a priori* probabilities [33], and for sets comprising up to seven equally likely qubit states [34], as described in this thesis (Chapter 3).

In general, optimal measurements for quantum state discrimination are based on positive operator-valued measures (POVMs). For optimal FRIO, the corresponding POVM can be implemented in an assisted manner by coupling the main system to an auxiliary one (ancilla) and measuring both. This approach decomposes the measurement into two steps [23, 35–38]. First, an optimal *state separation* quantum map probabilistically modifies the distinguishability of the input states, yielding either more distinguishable outputs—with maximum success probability—or less distinguishable ones—with minimum failure rate. Then, a ME measurement is applied to discriminate the successful outputs, while the failure outputs are discarded, yielding inconclusive outcomes.

Interestingly, for qudits, the failure outputs often still carry useful information about the inputs, opening the possibility for further discrimination attempts. In this context, the procedure described above—where failure outputs are discarded—will be referred to as *standard* FRIO. In contrast, the scenario in which failure outputs are further discriminated using a suitable strategy will be called *concatenated* FRIO. Recovering information otherwise discarded in the standard approach has been shown to improve quantum communication protocols such as teleportation [39], entanglement swapping [40], dense coding, and quantum key distribution [24]. Recently, the concatenation between optimal UD and ME was experimentally demonstrated [41].

Despite the relevance of quantum state discrimination in quantum information science and quantum foundations, analytical solutions for the optimal measurement strategies discussed above remain scarce and are known only for a few specific scenarios. Among the analytically solvable cases, a notable example is the set of N symmetric, n-dimensional pure states ($N \geq n \geq 2$), prepared with equal *a priori* probabilities (i.e., $\eta_j = 1/N$ for all j). This family admits exact solutions for ME [42], optimal UD [43], MC [37], and FRIO [21] measurements, making it a valuable resource for many applications in quantum communications (see, e.g, [23, 24, 39, 40, 44–48]). In this thesis, we explore the theoretical, experimental, and fundamental aspects of the optimal FRIO measurement applied to the discrimination of such sets of symmetric states. The work is divided into two parts organized as follows:

Part I – Theory and experiment

Chapter 1 presents a review of the most important aspects of projective and generalized quantum measurements that will be useful for the subsequent developments in the thesis. We then revisit the ME, optimal UD, and FRIO strategies applied to the discrimination of two nonorthogonal qubit states prepared with arbitrary *a priori* probabilities, providing physical insights into the problem.

In Chapter 2, we introduce the family of equally likely symmetric states and revisit the known analytical solutions for their discrimination via ME and optimal UD/MC strategies. Next, we address the optimal FRIO strategy as a two-step process: first describing the state separation map and then combining it with the ME measurement. This construction provides a physical implementation of the strategy and enables the derivation of an analytical expression for its figure of merit. Finally, we introduce the concatenated FRIO strategy, in which the information contained in the failure outputs is recovered via ME, and show that this enhances the overall probability of correct identifications.

In Chapter 3, we explore the physical implementation of the optimal FRIO measurement developed in the previous chapter and apply it to the experimental discrimination of N nonorthogonal qubit states, for $N = 2, 3, 5$, and 7. The qubit states are encoded in photonic spatial modes, while polarization serves as an ancilla. These degrees of freedom are coupled via a spatial light modulator to assist in the state separation process. We show that, within experimental uncertainty, the error rates are minimized as the inconclusive rate is varied from zero to a critical value. Finally, we discuss how our setup can be straightforwardly adapted to implement the FRIO strategy for qudits.

Part II – Fundamental aspects

Chapter 4 addresses the role of quantum coherence, defined with respect to POVMs, as a resource for implementing the standard and concatenated FRIO measurements introduced in Chapter 2. We show that, in the state separation stage, the POVM coherence decomposes into contributions from the ancilla's coherence and the system-ancilla quantum discord, highlighting coherence as a more elementary resource than quantum correlations. We further demonstrate that the total coherence required for both standard and concatenated FRIO strategies splits into contributions from the separation and ME measurement stages, each weighted by their respective probabilities, thus leading to a higher coherence cost in the concatenated case. Finally, we interpret these results in the context of secure quantum communication.

In Chapter 5, we investigate wave-particle duality relations for a quantum system traversing an interferometer with N equally probable paths, where each path is tagged by a symmetric state of a quantum which-way detector. By characterizing the wave aspects through the system's coherence and the particle aspects via the mutual information obtained from detector-state discrimination, we employ the strategies introduced in Chapter 2 to derive entropic duality relations between these quantities. Our analysis shows that the ME measurement yields the tightest bound in the relation, followed by the concatenated FRIO and standard FRIO strategies. We further show that the relation is saturated at nontrivial points only when the number of paths is non-prime, and identify the corresponding detector states responsible for this behavior.

As each Chapter from 2 to 5 ends with a "Summary and outlook" section highlighting its specific contributions and perspectives, in the final chapter, Conclusion, we present our concluding remarks, integrating the overall findings of this thesis and outlining possible directions for future research.

Part I

Theory and Experiment

1 An introduction to quantum state discrimination

"Of the beginning, of the beginning."
Tomorrow Never Knows, The Beatles

This chapter introduces the basic aspects of the quantum measurement process and its application to the discrimination of nonorthogonal states, laying the groundwork for the problems explored in the following chapters. We begin by reviewing projective and generalized measurements, including Naimark's extension theorem as an approach to implement the latter. We then present a formal proof of the impossibility of perfectly discriminating nonorthogonal quantum states, highlighting the fundamental limitations imposed by quantum mechanics. Finally, focusing on the discrimination of two pure qubit states prepared with arbitrary *a priori* probabilities, we revisit the main optimal measurement strategies.

1.1 Projective and generalized quantum measurements

Measurement is the fundamental process by which information is extracted from a quantum system. It is therefore a key element for both understanding quantum theory and developing quantum technologies. In this section, we provide an overview of the definitions and basic properties of projective and generalized measurements that will be useful for the discussions presented in this thesis. For more details about quantum measurement theory, see Refs. [49,50].

1.1.1 Projective measurements

A projective measurement can be defined as:

Definition 1.1. *A set of operators* $\{\hat{\pi}_k, k \in \mathcal{S}\}$ *acting on a Hilbert space* $\mathcal{H}$*, with* $\mathcal{S}$ *representing the set of all possible outcomes of the measurement, corresponds to a projective measurement if: (I)* $\hat{\pi}_k$ *is positive semi-definite* $(\hat{\pi}_k \geq 0)$*, which implies that it is also hermitian*[1] $\left(\hat{\pi}_k = \hat{\pi}_k^\dagger\right)$*; (II) the set satisfies the completeness relation* $\left(\sum_{k\in\mathcal{S}} \hat{\pi}_k = \hat{I}\right)$*; (III)* $\hat{\pi}_k$ *is pairwise orthogonal* $(\hat{\pi}_k\hat{\pi}_\ell = \delta_{k\ell})$*, which implies that it is also idempotent* $(\hat{\pi}_k^2 = \hat{\pi}_k)$*.*

---

[1] An interested reader may solve the exercise 2.24 of Ref. [50].

For an arbitrary quantum state $\hat{\rho} \in \mathcal{B}(\mathcal{H})$, where $\mathcal{B}(\mathcal{H})$ is the space of bounded linear operators, the probability of obtaining the outcome k when implementing this measurement is given by

$$p_k = \text{Tr}(\hat{\pi}_k \hat{\rho}), \tag{1.1}$$

where Tr denotes the trace. Properties (I) and (II) provide the necessary conditions for p_k to be a probability: the former implies that it is a real nonnegative number, and the latter ensures that $\sum_{k \in \mathcal{S}} p_k = 1$. Property (III) limits the number of elements $\{\hat{\pi}_k\}$, and consequently the number of possible outcomes of the measurement, to the dimension of the Hilbert space $\mathcal{H}$. Given that the outcome k was obtained, the post-measurement state yields:

$$\hat{\rho}'_k = \frac{\hat{\pi}_k \hat{\rho} \hat{\pi}_k}{p_k}. \tag{1.2}$$

On the other hand, if the result of the measurement is not recorded, the post-measurement quantum state is given by

$$\hat{\rho}' = \sum_k \hat{\pi}_k \hat{\rho} \hat{\pi}_k = \sum_k p_k \hat{\rho}'_k. \tag{1.3}$$

1.1.2 Positive operator-valued measures

For a generalized quantum measurement, the requirement for the operators to be pairwise orthogonal [property (III) of definition 1.1] is lifted. Thus, unlike projective measurements, the number of outcomes in a generalized measurement is not limited by the dimension of the Hilbert space. This type of measurement can be treated using the positive operator-valued measure (POVM) formalism, defined as:

Definition 1.2. *A set of operators* $\{\hat{\Pi}_k, k \in \mathcal{S}\}$ *acting on a Hilbert space* $\mathcal{H}$*, with* $\mathcal{S}$ *being the set of all possible outcomes of the measurement, is called a positive operator-valued measure if: (I)* $\hat{\Pi}_k$ *is positive semi-definite* $\left(\hat{\Pi}_k \geq 0\right)$*; (II) the set satisfies the completeness relation* $\left(\sum_{k \in \mathcal{S}} \hat{\Pi}_k = \hat{I}\right)$.

The POVM elements $\hat{\Pi}_k$ can be represented by the detection (also known as Kraus) operators $\hat{A}_k$ as $\hat{\Pi}_k = \hat{A}_k^\dagger \hat{A}_k$. These operators generalize the projectors and can be written, up to an arbitrary unitary transformation $\hat{U}$, as $\hat{A}_k = \hat{U}\sqrt{\hat{\Pi}_k}$. Similar to Eq. (1.1), the probability of obtaining the outcome k when performing this measurement is given by

$$p_k = \text{Tr}(\hat{\Pi}_k \hat{\rho}) = \text{Tr}(\hat{A}_k \hat{\rho} \hat{A}_k^\dagger). \tag{1.4}$$

Again, properties (I) and (II) ensure that p_k is a probability. In this case, the post-measurement quantum state associated with the outcome k is given by

$$\hat{\rho}'_k = \frac{\hat{A}_k \hat{\rho} \hat{A}_k^\dagger}{p_k}. \tag{1.5}$$

On the other hand, if the result of the measurement is not recorded, the post-measurement quantum state is determined by

$$\hat{\rho}' = \sum_k \hat{A}_k \hat{\rho} \hat{A}_k^\dagger = \sum_k p_k \hat{\rho}_k'. \tag{1.6}$$

1.1.3 Naimark's theorem

POVMs are of great importance in quantum information science, since they enable more general measurement strategies to acquire information about the state of a quantum system, as we will show in the next section. The question now is how to perform this class of operations. Fortunately, it is possible to establish a correspondence between POVMs and projective measurements. This result follows from Naimark's theorem, which states that for any POVM on a Hilbert space $\mathcal{H}$, there exists a projective measurement on an extended Hilbert space $\mathcal{H}'$ that implements this POVM [49]. As a consequence, it guarantees that every POVM has a realizable experimental procedure, which involves attaching auxiliary degrees of freedom (ancilla) to the main system—thus expanding its Hilbert space—coupling them through a unitary operation and performing a projective measurement on the extended space. There are two ways to perform this procedure, corresponding to the two methods of extending the initial Hilbert space, as briefly described next.

Tensor product extension

In this scenario, the ancilla is either another quantum system or an additional degree of freedom of the main system, such that the extended space is the tensor product of the system's $(\mathcal{H}_{\mathsf{d}})$ and ancilla's $(\mathcal{H}_{\mathsf{a}})$ space,[2] i.e., $\mathcal{H}' = \mathcal{H}_{\mathsf{d}} \otimes \mathcal{H}_{\mathsf{a}}$. If $\dim(\mathcal{H}_{\mathsf{d}}) = n$ and $\dim(\mathcal{H}_{\mathsf{a}}) = n_a$, then $\dim(\mathcal{H}') = n \times n_a \equiv N'$. Now, let $\mathbf{\Pi} = \{\hat{\Pi}_j\}_{j=0}^{N-1}$ be an N-outcome POVM on $\mathcal{H}_{\mathsf{d}}$, where $N \leq N'$. To implement this POVM on an arbitrary $\hat{\rho}$, first, one attaches the ancilla in a fixed state, say $|\ell\rangle_{\mathsf{a}}$, via a tensor product, generating the global initial state $\hat{\rho}_{\mathsf{da}} = \hat{\rho} \otimes |\ell\rangle_{\mathsf{a}}\langle\ell|$. The system and the ancilla are then coupled through a suitable global unitary operation, $\hat{V}$, resulting in the state $\hat{\sigma}_{\mathsf{da}} = \hat{V}\hat{\rho}_{\mathsf{da}}\hat{V}^\dagger$. Finally, in an N-dimensional subspace of $\mathcal{H}'$, one can find a projective measurement $\{\hat{\varpi}_j\}_{j=0}^{N-1}$ that, when applied to $\hat{\sigma}_{\mathsf{da}}$, yields the same outcome probabilities as the POVM, i.e., $\mathrm{Tr}(\hat{\varpi}_j\hat{\sigma}_{\mathsf{da}}) = \mathrm{Tr}(\hat{\Pi}_j\hat{\rho}) = p_j$. The projectors $\hat{\varpi}_j$ can be written as $\hat{\varpi}_j = \hat{\pi}_j^{\mathsf{d}} \otimes |\ell(j)\rangle_{\mathsf{a}}\langle\ell(j)|$, where $\{\hat{\pi}_j^{\mathsf{d}}\}$ is a set of projectors on $\mathcal{H}_{\mathsf{d}}$ and $\{|\ell(j)\rangle_{\mathsf{a}}\langle\ell(j)|\}$ corresponds to the elements of the projective measurement on $\mathcal{H}_{\mathsf{a}}$ associated with the jth outcome.[3] The rank

---

[2] Here, we denote the main system and ancilla by the indices d and a, respectively, following the notation that will be adopted in Chapter 4, where this method will be particularly useful.

[3] If $N > n_a$, some elements of the projective measurement $\{|\ell\rangle_{\mathsf{a}}\langle\ell|\}_{\ell=0}^{n_a-1}$ on the ancilla space that constitute $\{\hat{\varpi}_j\}$ may appear more than once.

of each $\hat{\varpi}_j$ may vary between one and n. Using the cyclic property of the trace, we can write $p_j = \mathrm{Tr}(\hat{\pi}_j \hat{\rho}_{\mathsf{da}})$, where

$$\hat{\pi}_j = \hat{V}^\dagger \left(\hat{\pi}_j^{\mathsf{d}} \otimes |\ell(j)\rangle_{\mathsf{a}} \langle \ell(j)| \right) \hat{V}. \tag{1.7}$$

Thus, the POVM can be equivalently implemented as a projective measurement on the initial system-ancilla state in this rotated basis. Throughout this thesis, we present several examples in which this method is employed.

Direct sum extension

In this scenario, the n-dimensional Hilbert space of the system of interest, $\mathcal{H}_{\mathsf{d}}$, is actually a subspace of a larger N-dimensional space $\mathcal{H}'$. Thus, the ancilla consists of the $n_a = N - n$ unused dimensions of a subspace $\mathcal{H}_{\mathsf{a}}$ and the extended space is the direct sum $\mathcal{H}' = \mathcal{H}_{\mathsf{d}} \oplus \mathcal{H}_{\mathsf{a}}$. Now, let $\mathbf{\Pi} = \{\hat{\Pi}_j\}_{j=0}^{N-1}$ be an N-outcome POVM on $\mathcal{H}_{\mathsf{d}}$. To implement this POVM on an arbitrary $\hat{\rho}$, first, one couples the ancilla to the main system through a suitable unitary operation, $\hat{V}$, acting on $\mathcal{H}'$. The initial system-ancilla state is given by $\hat{\rho}_{\mathsf{da}} = \hat{\rho} \oplus \hat{0}_{\mathsf{a}}$, where $\hat{0}_{\mathsf{a}}$ denotes the zero operator on $\mathcal{H}_{\mathsf{a}}$. After applying the unitary, this state evolves to $\hat{\sigma}_{\mathsf{da}} = \hat{V} \hat{\rho}_{\mathsf{da}} \hat{V}^\dagger$. Finally, one can find a projective measurement $\{\hat{\varpi}_j\}_{j=0}^{N-1}$ that, when applied to $\hat{\sigma}_{\mathsf{da}}$, yields the same outcome probabilities as the POVM, i.e., $\mathrm{Tr}(\hat{\varpi}_j \hat{\sigma}_{\mathsf{da}}) = \mathrm{Tr}(\hat{\pi}_j \hat{\rho}_{\mathsf{da}}) = \mathrm{Tr}(\hat{\Pi}_j \hat{\rho}) = p_j$, where $\hat{\pi}_j = \hat{V}^\dagger \hat{\varpi}_j \hat{V}$. An explicit example illustrating this method will be presented in Chapter 3.

1.2 Optimal state discrimination: main strategies

Suppose that a quantum system may be in either of two pure states $\{|\psi_0\rangle, |\psi_1\rangle\}$ and that such states are nonorthogonal, i.e., $\langle \psi_0 | \psi_1 \rangle \neq 0$. Suppose further that we are given this system and asked what its quantum state is. In order to answer this question, we implement a measurement on the system and use the obtained outcome as a guide to identify its state. An error-free projective measurement would be of the form:

$$\hat{\pi}_k |\psi_j\rangle = \delta_{jk} |\psi_k\rangle, \tag{1.8}$$

for $j, k = 0, 1$. However, as the quantum states are nonorthogonal, this measurement is impossible. To see why this is true, let us insert the identity $\hat{I} = \hat{\pi}_0 + \hat{\pi}_1$ in the inner product:

$$\langle \psi_0 | \hat{I} | \psi_1 \rangle = \langle \psi_0 | \left(\hat{\pi}_0 + \hat{\pi}_1 \right) | \psi_1 \rangle = \langle \psi_0 | \hat{\pi}_0 | \psi_1 \rangle + \langle \psi_0 | \hat{\pi}_1 | \psi_1 \rangle = 0. \tag{1.9}$$

This contradicts the initial assumption of nonorthogonality, hence eliminating the existence of a measurement scheme like (1.8) for nonorthogonal states. This limitation, imposed by the laws of quantum theory, gave rise to intense research into optimal measurement strategies for discriminating such states (e.g., see reviews [6–9]), which later had a strong impact on quantum information and quantum communication [24, 35, 39, 40, 44–48, 51–55].

In this section, we introduce the most relevant strategies in the field of optimal quantum state discrimination, namely: minimum-error (ME) measurement, unambiguous discrimination (UD), and discrimination with fixed rate of inconclusive outcomes (FRIO). In particular, we consider the case of discriminating between two pure states of a qubit, which provides useful physical insights into the problem.

1.2.1 Minimum-error discrimination

Assume that an observer, in possession of a quantum system, knows in advance that it has been prepared in one of two possible states, $\hat{\rho}_0$ or $\hat{\rho}_1$, with probabilities η_0 and $\eta_1 = 1 - \eta_0$, respectively. Faced with the task of identifying the state and knowing the impossibility of doing so perfectly, the observer would like to implement a projective measurement that minimizes the average probability of error. Helstrom solved this problem in his pioneering work on quantum detection theory [1], and here we revisit his result.

Let $\{\hat{\pi}_0, \hat{\pi}_1\}$ be the set of operators that describe the projective measurement that will be performed to discriminate the states. The outcome associated with $\hat{\pi}_k$ leads the observer to identify the state as $\hat{\rho}_k$ (for $k = 0, 1$). Then, the average error probability in this identification is given by the following expression:

$$\begin{aligned} P_e &= \eta_0 \mathrm{Tr}(\hat{\rho}_0 \hat{\pi}_1) + \eta_1 \mathrm{Tr}(\hat{\rho}_1 \hat{\pi}_0) && (1.10) \\ &= \eta_0 - \mathrm{Tr}[(\eta_0 \hat{\rho}_0 - \eta_1 \hat{\rho}_1)\hat{\pi}_0] && (1.11) \\ &= \eta_1 + \mathrm{Tr}[(\eta_0 \hat{\rho}_0 - \eta_1 \hat{\rho}_1)\hat{\pi}_1], && (1.12) \end{aligned}$$

where we used $\hat{\pi}_0 + \hat{\pi}_1 = \hat{I}$ and $\mathrm{Tr}(\hat{\rho}_k) = 1$. Therefore, to minimize P_e, the optimized measurement scheme is the one that maximizes the quantity $\mathrm{Tr}[(\eta_0 \hat{\rho}_0 - \eta_1 \hat{\rho}_1)\hat{\pi}_0]$, or minimizes $\mathrm{Tr}[(\eta_0 \hat{\rho}_0 - \eta_1 \hat{\rho}_1)\hat{\pi}_1]$. To find that, let us address the spectral decomposition of the hermitian operator $\eta_0 \hat{\rho}_0 - \eta_1 \hat{\rho}_1$:

$$\eta_0 \hat{\rho}_0 - \eta_1 \hat{\rho}_1 = \sum_k \lambda_k |\lambda_k\rangle\langle\lambda_k|. \tag{1.13}$$

Its eigenvalues may be positive, negative, or zero. The error probability in Eq. (1.11) is minimized if $\hat{\pi}_0$ is the projector onto the positive-eigenvalue eigenvectors of $\eta_0 \hat{\rho}_0 - \eta_1 \hat{\rho}_1$, and in Eq. (1.12) if $\hat{\pi}_1$ is the projector onto the negative-eigenvalue eigenvectors. Using these conditions and adding the resulting equations, we obtain

$$P_e^{\min} = \frac{1}{2}\left(1 - \sum_k |\lambda_k|\right)$$
$$= \frac{1}{2}\left(1 - \|\eta_0\hat{\rho}_0 - \eta_1\hat{\rho}_1\|\right), \tag{1.14}$$

where $\|\hat{B}\| = \mathrm{Tr}\sqrt{\hat{B}^\dagger\hat{B}}$ is the trace norm of operator $\hat{B}$. Equation (1.14) gives the minimum error probability for discriminating between two states and is known as the *Helstrom bound*.

We now apply this result to the discrimination of two pure states of a qubit, given by

$$|\psi_0\rangle = \cos\theta|0\rangle + \sin\theta|1\rangle, \tag{1.15a}$$

$$|\psi_1\rangle = \cos\theta|0\rangle - \sin\theta|1\rangle, \tag{1.15b}$$

where $\theta \in [0, \pi/4]$ and $\{|0\rangle, |1\rangle\}$ is an orthonormal basis for the qubit space. In this case, it is easy to show that the eigenvalues of the operator in Eq. (1.13) are given by

$$\lambda_j = \frac{1}{2}\left[(\eta_0 - \eta_1) + (-1)^j\sqrt{1 - 4\eta_0\eta_1\alpha^2}\right], \tag{1.16}$$

where $j = 0, 1$, and

$$\alpha \equiv \langle\psi_0|\psi_1\rangle = \cos 2\theta \tag{1.17}$$

denotes the overlap between the states. Thus, using Eq. (1.14), the minimum error probability will be given by

$$P_e^{\min} = \frac{1}{2}\left(1 - \sqrt{1 - 4\eta_0\eta_1\alpha^2}\right). \tag{1.18}$$

As expected, this probability increases with the overlap between the states, as shown in the left panel of Fig. 1 for different values of η_0 shown in the inset; it vanishes for orthogonal states ($\alpha = 0$) and reaches its maximum for parallel states ($\alpha = 1$). Note in the plot that $P_e^{\min}$ is extremal if the states are equiprobable. Such a feature can also be observed in the right panel of Fig. 1, where we plot $P_e^{\min}$ in terms of the *a priori* probability η_0 for fixed overlaps shown in the inset. Evidently, the error probability vanishes if one of the two states is not produced ($\eta_0 = 0$ or $\eta_0 = 1$), as the discrimination becomes a trivial task.

From the conditions for minimizing P_e described earlier, $\hat{\pi}_0$ and $\hat{\pi}_1$ are projectors onto the eigenvectors $\{|\lambda_j\rangle\}$ associated with the eigenvalues $\{\lambda_j\}$ of $\eta_0\hat{\rho}_0 - \eta_1\hat{\rho}_1$, that is $\hat{\pi}_j = |\lambda_j\rangle\langle\lambda_j|$, where

$$|\lambda_j\rangle = \frac{\sqrt{1-\alpha^2}|0\rangle + \left[(\eta_1 - \eta_0)\alpha + (-1)^j\sqrt{1 - 4\eta_0\eta_1\alpha^2}\right]|1\rangle}{\sqrt{2}\sqrt{1 - 4\eta_0\eta_1\alpha^2 + 2(\eta_0 - \eta_1)\alpha\sqrt{1 - 4\eta_0\eta_1\alpha^2}}}. \tag{1.19}$$

Figure 2 depicts the ME measurement for two states of a qubit with fixed overlap $\alpha = 0.6$ and different values of η_0. Note that if the states are produced with equal *a priori* probabilities, i.e., $\eta_0 = \eta_1 = 1/2$, then the ME measurement is the projection onto $|\lambda_j\rangle = [|0\rangle + (-1)^j|1\rangle]/\sqrt{2}$, whatever the overlap between them [see Fig. 2(c)].

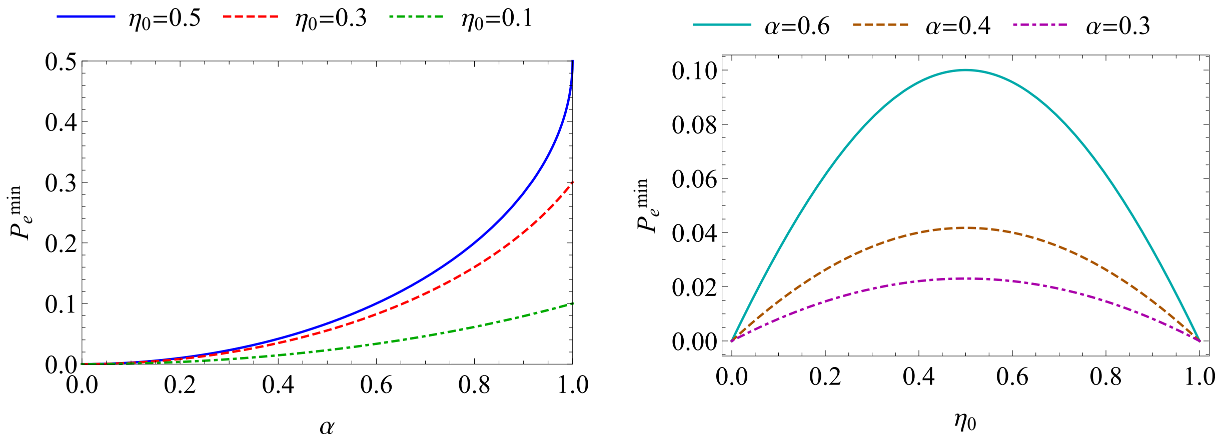

Figure 1 – Minimum error probability in the discrimination of two pure states of a qubit. Left: $P_e^{\min}$ as a function of the overlap for fixed *a priori* probabilities (shown in the inset). Right: $P_e^{\min}$ as a function of the *a priori* probability η_0 for fixed overlaps (shown in the inset).

1.2.2 Optimal unambiguous discrimination

As shown in the introduction of this section, an error-free discrimination between nonorthogonal states cannot be achieved using projective measurements. However, it is possible to fulfill the requirement $P_e = 0$ [Eq. (1.10)] by addressing generalized measurements, as long as we tolerate inconclusive results, i.e., results that do not provide any information about the states to be discriminated. This problem was introduced and analytically solved for two pure and equally

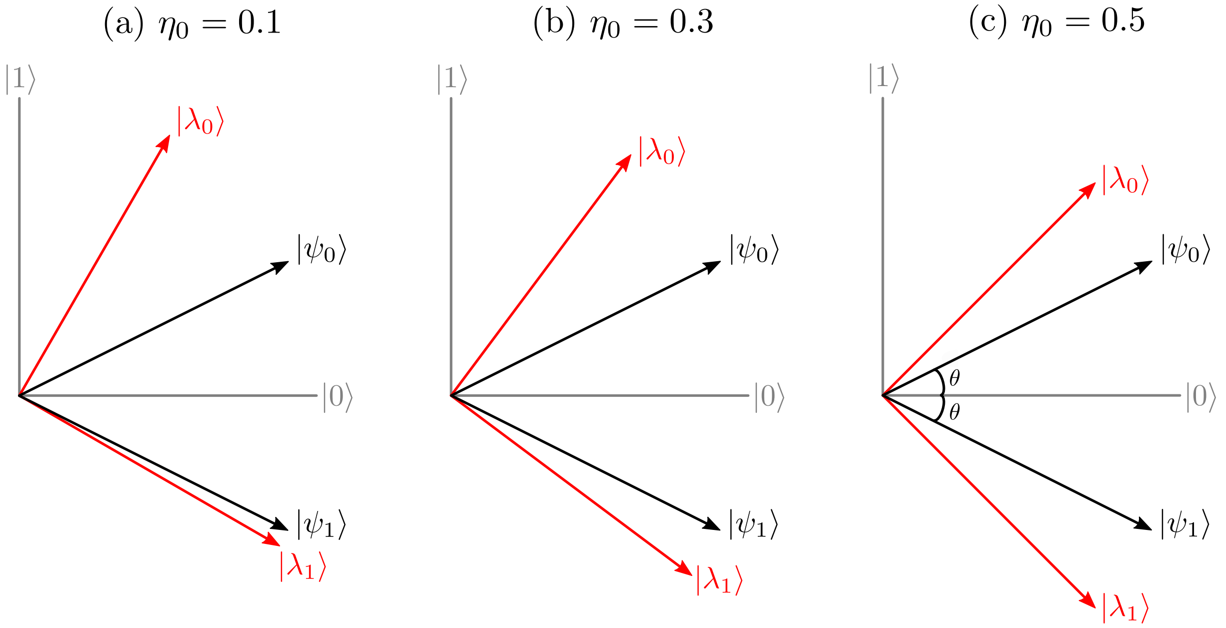
(a) $\eta_0 = 0.1$ (b) $\eta_0 = 0.3$ (c) $\eta_0 = 0.5$

Figure 2 – The states $\{|\psi_0\rangle, |\psi_1\rangle\}$ [Eq. (1.15)] with overlap $\alpha = 0.6$ and *a priori* probabilities $\{\eta_0, 1 - \eta_0\}$ are discriminated with minimum error by means of a projective measurement in the basis $\{|\lambda_0\rangle, |\lambda_1\rangle\}$ [Eq. (1.19)].

probable states of a qubit in the works of Ivanovic [13], Dieks [14], and Peres [15]. A few years later, Jaeger and Shimony generalized these findings for the case of arbitrary *a priori* probabilities [16]. Here, we review these results using Bergou's approach described in Ref. [9].

Let us again consider the two pure states $\{|\psi_0\rangle, |\psi_1\rangle\}$ given by Eq. (1.15), which have *a priori* probabilities $\{\eta_0, \eta_1\}$. Unambiguous discrimination between them is performed through a three-outcome POVM $\mathbf{\Pi} = \{\hat{\Pi}_0, \hat{\Pi}_1, \hat{\Pi}_?\}$, where the outcome associated with $\hat{\Pi}_j$ $(j = 0, 1)$ leads to the identification of $|\psi_j\rangle$ without error, with probability $p_j = \langle\psi_j|\hat{\Pi}_j|\psi_j\rangle$, while the outcome associated with $\hat{\Pi}_?$ leads to an inconclusive answer with probability $q_j = \langle\psi_j|\hat{\Pi}_?|\psi_j\rangle = 1 - p_j$. First, in order to ensure error-free identifications, we must have $\langle\psi_0|\hat{\Pi}_1|\psi_0\rangle = \langle\psi_1|\hat{\Pi}_0|\psi_1\rangle = 0$, which is achieved with operators given by

$$\hat{\Pi}_0 = \frac{1 - q_0}{|\langle\psi_0|\psi_1^\perp\rangle|^2}|\psi_1^\perp\rangle\langle\psi_1^\perp|, \tag{1.20a}$$

$$\hat{\Pi}_1 = \frac{1 - q_1}{|\langle\psi_0|\psi_1^\perp\rangle|^2}|\psi_0^\perp\rangle\langle\psi_0^\perp|, \tag{1.20b}$$

where

$$|\psi_0^\perp\rangle = \sin\theta|0\rangle - \cos\theta|1\rangle, \tag{1.21a}$$

$$|\psi_1^\perp\rangle = \sin\theta|0\rangle + \cos\theta|1\rangle, \tag{1.21b}$$

have support on the orthogonal subspaces of the corresponding states of Eqs. (1.15), i.e., $\langle\psi_j^\perp|\psi_j\rangle = 0$. Next, from the completeness relation, the inconclusive POVM element will be given by

$$\hat{\Pi}_? = \hat{I} - \hat{\Pi}_0 - \hat{\Pi}_1. \tag{1.22}$$

Under the constraint $\hat{\Pi}_? \geq 0$, the optimization task consists of minimizing the average probability of inconclusive outcomes

$$Q \equiv \mathrm{Tr}(\hat{\Pi}_?\hat{\rho}) = \eta_0 q_0 + \eta_1 q_1, \tag{1.23}$$

where $\hat{\rho} = \eta_0|\psi_0\rangle\langle\psi_0| + \eta_1|\psi_1\rangle\langle\psi_1|$ is the *a priori* state of the system. By calculating the eigenvalues of $\hat{\Pi}_?$ and using their nonnegativity, it can be shown that the following constraint is obtained [9]:

$$q_0 q_1 \geq \alpha^2, \tag{1.24}$$

where $\alpha = \langle\psi_0|\psi_1\rangle$ [see Eq. (1.17)]. Taking the minimum allowed by this constraint, we can rewrite Eq. (1.23) as $Q = \eta_0 q_0 + \eta_1\alpha^2/q_0$. Then, the minimization condition $\partial Q/\partial q_0 = 0$ leads to

$$q_j = \sqrt{\frac{1 - \eta_j}{\eta_j}}\alpha, \tag{1.25}$$

for $j = 0, 1$. The conditions $q_0, q_1 \leq 1$ impose a validity domain on the above solution (cases outside that domain need special consideration, which will be discussed below). Finally, the minimum probability of inconclusive outcomes can be calculated by substituting Eq. (1.25) into Eq. (1.23), yielding

$$Q_0 = 2\sqrt{\eta_0\eta_1}\alpha, \quad \text{if} \quad \frac{\alpha^2}{1+\alpha^2} \leq \eta_0 \leq \frac{1}{1+\alpha^2}. \tag{1.26}$$

As expected, the inconclusive rate increases with the overlap between the states; in particular, it equals the overlap when the states are equiprobable, which is known as the IDP limit, due to Ivanovic, Dieks, and Peres [13–15].

If the *a priori* probabilities are outside the domain of validity of solution (1.26), i.e., $\eta_0 < \frac{\alpha^2}{1+\alpha^2}$ or $\eta_0 > \frac{1}{1+\alpha^2}$, optimal UD can only be achieved by performing a projective measurement that perfectly identifies the most probable state. Assuming that $\eta_0 < \eta_1$, the optimal measurement takes the form:

$$\hat{\pi}_1 = |\psi_0^\perp\rangle\langle\psi_0^\perp|, \tag{1.27a}$$

$$\hat{\pi}_0 = \hat{\pi}_? = |\psi_0\rangle\langle\psi_0|. \tag{1.27b}$$

It is straightforward to show that $\langle\psi_1|\hat{\pi}_0|\psi_1\rangle = \alpha^2$ and $\langle\psi_0|\hat{\pi}_k|\psi_0\rangle = \delta_{k0}$, which implies

$$\begin{aligned} Q_{\eta_1} &= \text{Tr}\left[\hat{\rho}\hat{\pi}_0\right] \\ &= \eta_0 + \eta_1\alpha^2. \end{aligned} \tag{1.28}$$

Similarly, if $\eta_0 > \eta_1$, the optimal measurement will be $\{\hat{\pi}_0 = |\psi_1^\perp\rangle\langle\psi_1^\perp|, \hat{\pi}_1 = \hat{\pi}_? = |\psi_1\rangle\langle\psi_1|\}$, which gives $Q_{\eta_0} = \eta_1 + \eta_0\alpha^2$.

Summarizing the above results, the minimum inconclusive rate for implementing UD within each domain is given by

$$Q^{\text{UD}} \equiv \begin{cases} Q_0 = 2\sqrt{\eta_0\eta_1}\alpha, & \text{if} \quad \dfrac{\alpha^2}{1+\alpha^2} \leq \eta_0 \leq \dfrac{1}{1+\alpha^2}, \\ Q_{\eta_1} = \eta_0 + \eta_1\alpha^2, & \text{if} \quad \eta_0 < \dfrac{\alpha^2}{1+\alpha^2}, \\ Q_{\eta_0} = \eta_1 + \eta_0\alpha^2, & \text{if} \quad \eta_0 > \dfrac{1}{1+\alpha^2}. \end{cases} \tag{1.29}$$

This quantity is shown in the left panel of Fig. 3 as a function of the overlap for fixed *a priori* probabilities (shown in the inset), and in the right panel as a function of the *a priori* probability η_0 for fixed overlaps (shown in the inset). Similarly to the behavior of the error probability in the ME measurement (see Fig. 1), the inconclusive rate of optimal UD is extremal in the equiprobable scenario (represented by the blue solid line in the left panel of Fig. 3). Equation (1.29) shows that Q_{η_0} and Q_{η_1} are linear functions of η_0 in the ranges where the POVM does not exist. This

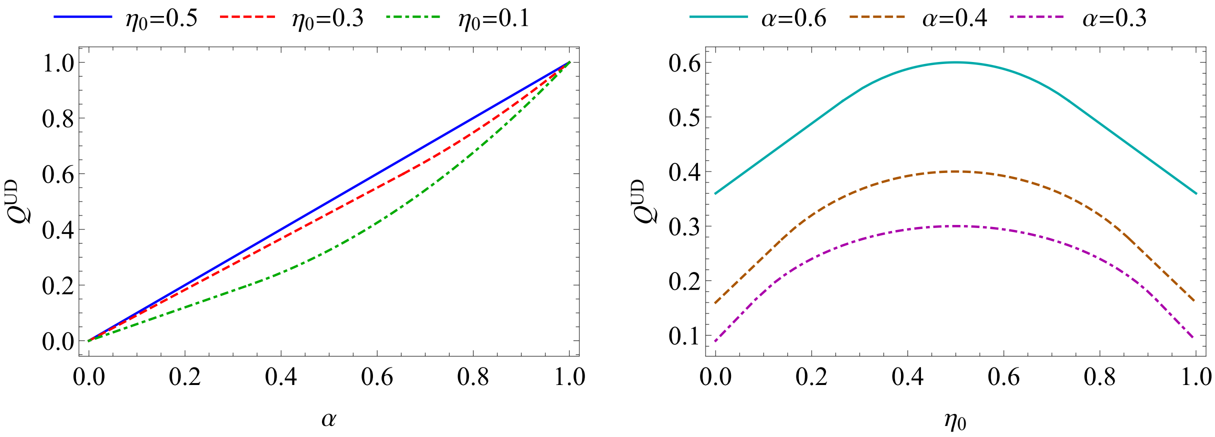

Figure 3 – Inconclusive rate in optimal UD for two pure states of a qubit [Eq. (1.29)]. Left: Q^{UD} as a function of the overlap between the states for fixed *a priori* probabilities (shown in the inset). Right: Q^{UD} as a function of the *a priori* probability η_0 for fixed overlaps (shown in the inset).

can be seen in the left panel of Fig. 3 and more clearly in Fig. 4, where, for a fixed overlap $\alpha = 0.6$, the ranges from Eq. (1.29) are represented by the shaded regions under the Q^{UD} curve. In region II, the optimal UD measurement corresponds to the three-outcome POVM, constructed from Eqs. (1.20)–(1.22) and (1.25). In contrast, optimal UD discrimination in regions I and III is carried out using a projective measurement in the bases $\{|\psi_0\rangle, |\psi_0^\perp\rangle\}$ and $\{|\psi_1\rangle, |\psi_1^\perp\rangle\}$, respectively, which only identifies the most probable state.

Unambiguous discrimination applies only to linearly independent states [17], as is the case with two nonorthogonal states of a qubit discussed here. However, a generalization

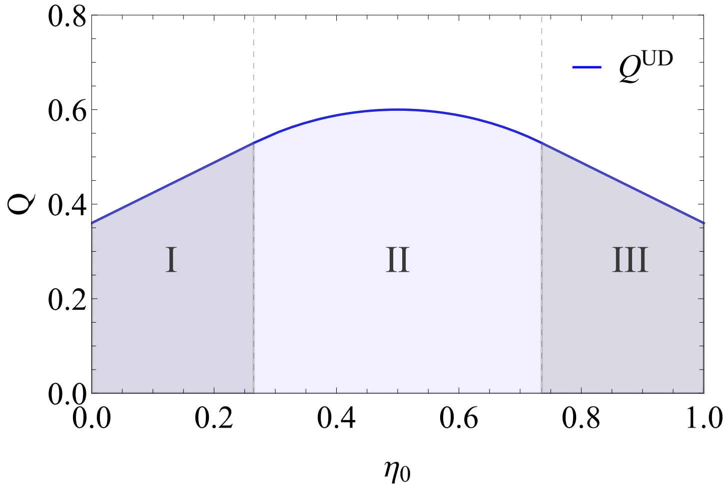

Figure 4 – Inconclusive rate in optimal UD for two pure states of a qubit [Eq. (1.29)] as a function of the *a priori* probability η_0 for a fixed overlap $\alpha = 0.6$. Shaded regions under the Q^{UD} curve correspond to the POVM regime (II) and projective measurement regimes (I and III) of the strategy. See text for details.

of optimal UD is possible, where linearly dependent states are identified with the maximum achievable confidence (lower than the 100% confidence provided by UD) and the minimum inconclusive rate [18]. This strategy, known as maximum-confidence measurement, will be described in detail in Chapter 2.

1.2.3 Optimal discrimination with fixed rate of inconclusive outcomes

A remarkable result in the field of quantum state discrimination is that the strategies presented so far—namely, ME and optimal UD—were shown to be extreme and particular cases of a more general optimized measurement scheme in which errors and inconclusive results are allowed [19, 20]. By minimizing the probability of errors under the constraint of a *fixed rate of inconclusive outcomes*, the so-called optimal FRIO strategy achieves lower error and inconclusive rates than ME and optimal UD, respectively. This problem was addressed and analytically solved for two pure states of a qubit with arbitrary *a priori* probabilities in [21]. Here, we review this result within the framework of Naimark's theorem, following Ref. [56].

Consider again the discrimination between the qubit states $\{|\psi_0\rangle, |\psi_1\rangle\}$ [Eq. (1.15)], prepared with probabilities $\{\eta_0, \eta_1\}$, and characterized by the overlap α, given by Eq. (1.17). Knowing that both erroneous and inconclusive answers are allowed, the observer prepares an ancilla qutrit[4] in some state $|k\rangle_a$ and entangles it with the qubit through a global unitary transformation, acting on the tensor product Hilbert space as

$$\hat{U}|\psi_0\rangle|k\rangle_a = \sqrt{p_0}|\phi_0\rangle|0\rangle_a + \sqrt{r_0}|\phi_1\rangle|1\rangle_a + \sqrt{q_0}|\phi_2\rangle|2\rangle_a, \tag{1.30a}$$

$$\hat{U}|\psi_1\rangle|k\rangle_a = \sqrt{r_1}|\phi_0\rangle|0\rangle_a + \sqrt{p_1}|\phi_1\rangle|1\rangle_a + \sqrt{q_1}|\phi_2\rangle|2\rangle_a, \tag{1.30b}$$

where $\{|0\rangle_a, |1\rangle_a, |2\rangle_a\}$ is an orthonormal basis for the qutrit space. By measuring the ancilla in this basis, the observer will identify the projections onto $|0\rangle_a$, $|1\rangle_a$, and $|2\rangle_a$ with the input state $|\psi_0\rangle$, $|\psi_1\rangle$, and an inconclusive answer, respectively. The probabilities of correct, erroneous, and inconclusive identifications are p_j, r_j, and q_j, respectively, and satisfy $p_j + r_j + q_j = 1$.

The FRIO optimization problem consists of minimizing $P_e = \eta_0 r_0 + \eta_1 r_1$ under the constraint that $Q = \eta_0 q_0 + \eta_1 q_1$ is fixed. According to the implementation in Eq. (1.30), an additional constraint is obtained by taking the inner product between (1.30a) and (1.30b):

$$\alpha = \sqrt{p_0 r_1} + \sqrt{p_1 r_0} + \sqrt{q_0 q_1}. \tag{1.31}$$

Thus, the observer's task is to optimize the unitary $\hat{U}$ to satisfy all these conditions.[5] In Appendix 6, the solution to this problem is presented using the Lagrange multiplier method.[6] The

---

[4] Three-dimensional quantum system.

[5] Note that if we impose the condition of error-free identifications, i.e., $r_0 = r_1 = 0$, then the constraint (1.31) becomes the equality of Eq. (1.24), enabling one to derive the solution of optimal UD.

[6] The same method can be applied to find the ME solution by setting $Q = 0$.

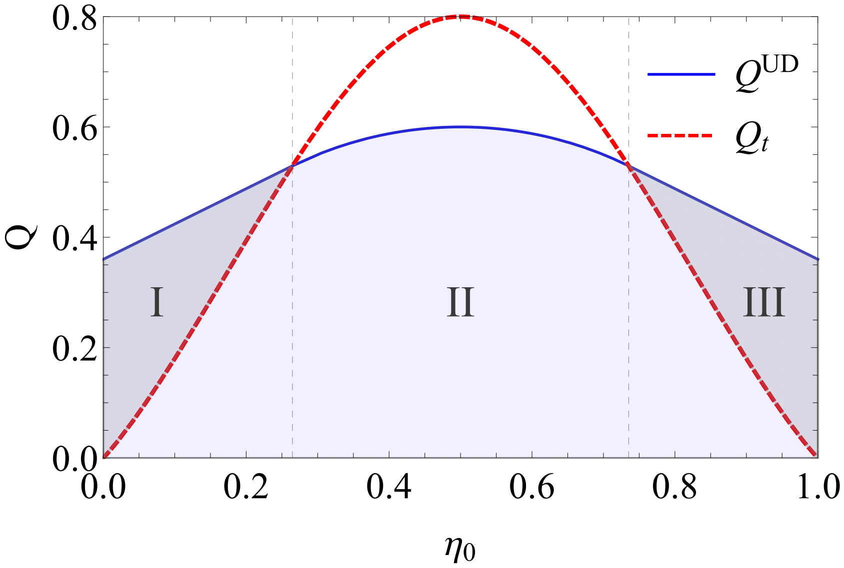

Figure 5 – Inconclusive rate Q^{UD} [Eq. (1.29)] and threshold rate Q_t [Eq. (1.33)] in optimal FRIO discrimination of two pure states of a qubit as a function of the *a priori* probability η_0 for a fixed overlap ($\alpha = 0.6$). The area of interest lies under the Q^{UD} curve. Q_t separates region II, where solution (1.34) is valid, from regions I and III, where solution (1.38) is valid.

optimal probabilities of inconclusive, erroneous, and correct outcomes are given by

$$q_i = \frac{Q}{2\eta_i}, \tag{1.32a}$$

$$r_i = \frac{1}{2}\left\{(1-q_i) - \frac{\left[(1-q_i)\bar{Q} - \frac{(Q_0-Q)^2}{2\eta_i}\right]}{\sqrt{\bar{Q}^2 - (Q_0-Q)^2}}\right\}, \tag{1.32b}$$

$$p_i = 1 - q_i - r_i, \tag{1.32c}$$

where $\bar{Q} = 1 - Q$ and Q_0 is given by Eq. (1.26). This solution is valid in three scenarios: (i) $\frac{\alpha^2}{1+\alpha^2} \leq \eta_0 \leq \frac{1}{1+\alpha^2}$ with $0 \leq Q \leq Q_0$; (ii) $\eta_0 < \frac{\alpha^2}{1+\alpha^2}$ with $Q \leq Q_t$; and (iii) $\eta_0 > \frac{1}{1+\alpha^2}$ with $Q \leq Q_t$, where

$$Q_t = \frac{2\eta_0\eta_1(1-\alpha^2)}{1-Q_0} \tag{1.33}$$

is a threshold rate [21]. In this domain of validity, represented by the shaded region II in the plot of Fig. 5, the optimal FRIO strategy is a three-outcome POVM, which is here implemented via tensor product extension, with the optimal unitary given by Eqs. (1.30) and (1.32). From Eq. (1.32b), the minimum error probability for a fixed value of Q is given by

$$P_e^{\min}(Q) = \frac{1}{2}\left[\bar{Q} - \sqrt{\bar{Q}^2 - (Q_0-Q)^2}\right]. \tag{1.34}$$

By setting $Q = 0$ in the above equation, we obtain the ME solution [Eq. (1.18)]. On the other hand, by setting $Q = Q_0$, we obtain $P_e^{\min} = 0$, which corresponds to optimal UD.

Similarly to optimal UD, in the shaded regions I and III of Fig. 5, the optimal FRIO strategy becomes a two-element projective measurement that prioritizes the identification of the most probable state, say $|\psi_1\rangle$. Using an ancilla qubit prepared in the state $|k\rangle_a$, the global unitary will be given by

$$\hat{U}|\psi_0\rangle|k\rangle_a = \sqrt{r_0}|\phi_1\rangle|1\rangle_a + \sqrt{q_0}|\phi_2\rangle|2\rangle_a, \tag{1.35a}$$

$$\hat{U}|\psi_1\rangle|k\rangle_a = \sqrt{p_1}|\phi_1\rangle|1\rangle_a + \sqrt{q_1}|\phi_2\rangle|2\rangle_a, \tag{1.35b}$$

where $\{|1\rangle_a, |2\rangle_a\}$ is an orthonormal basis for the qubit space. The projection of the ancilla onto $|1\rangle_a$, associated with the identification of $|\psi_1\rangle$, leads to a correct or erroneous outcome, while the projection onto $|2\rangle_a$ leads to an inconclusive outcome. The corresponding average probabilities are given by $P_c = \eta_1 p_1$, $P_e = \eta_0 r_0$, and $Q = 1 - P_e - P_c$, respectively. The conservation of the inner product gives the constraint

$$\alpha = \sqrt{r_0 p_1} + \sqrt{(1-r_0)(1-p_1)}, \tag{1.36}$$

which can be algebraically solved for p_1, yielding

$$p_1 = \left[\alpha\sqrt{r_0} + \sqrt{(1-\alpha^2)(1-r_0)}\right]^2. \tag{1.37}$$

Note that by setting $r_0 = 0$, we find $p_1 = 1 - \alpha^2$, leading to $Q = 1 - \eta_1 p_1 = Q_{\eta_1}$, which is the inconclusive rate of optimal UD in the projective measurement regime when $\eta_1 > \eta_0$ [second line of Eq. (1.29)]. To find $P_e^{\min}(Q)$ in this regime, we substitute $r_0 = P_e/\eta_0$ into Eq. (1.37) and invert the relation $Q = 1 - P_e - P_c$, obtaining

$$P_e^{\min}(Q) = \frac{\eta_0\bar{Q} + \gamma(1 - 2\eta_0 - 2\bar{Q}) - Q_0\sqrt{\gamma(Q\bar{Q} - \gamma)}}{1 - 4\gamma}, \tag{1.38}$$

where $\gamma = \eta_0\eta_1(1-\alpha^2)$. This solution is valid in two scenarios: $\eta_0 < \frac{\alpha^2}{1+\alpha^2}$ with $Q_t \leq Q \leq Q^{\text{UD}}$ (shaded region I of Fig. 5); and $\eta_0 > \frac{1}{1+\alpha^2}$ with $Q_t \leq Q \leq Q^{\text{UD}}$ (shaded region III of Fig. 5).

To conclude this subsection, we have described the optimal FRIO measurement that interpolates between the ME (for $Q = 0$) and optimal UD (for $Q = Q^{\text{UD}}$) strategies. In [21], it was shown that $P_e^{\min}(Q)$ is a non-increasing convex function, that is, it cannot increase with Q. In this way, optimal FRIO reduces the error rate compared to ME by allowing a nonzero rate of inconclusive outcomes; similarly, it will reduce this rate compared to optimal UD measurement at the expense of a higher error rate in the discrimination. All of these features can be seen in Fig. 6. In the left panel, we plot $P_e^{\min}$ as a function of η_0 for different values of Q (shown in the inset). It can be seen that if $\eta_0 \approx 0$ or $\eta_1 \approx 0$, the error rate tends to zero, since in this case the measurement outcomes are predominantly correct or inconclusive. In the right panel, we show how $P_e^{\min}$ decreases with Q for different *a priori* probabilities η_0 (shown in the inset). Note in particular that the error probability is maximum in the equiprobable scenario.

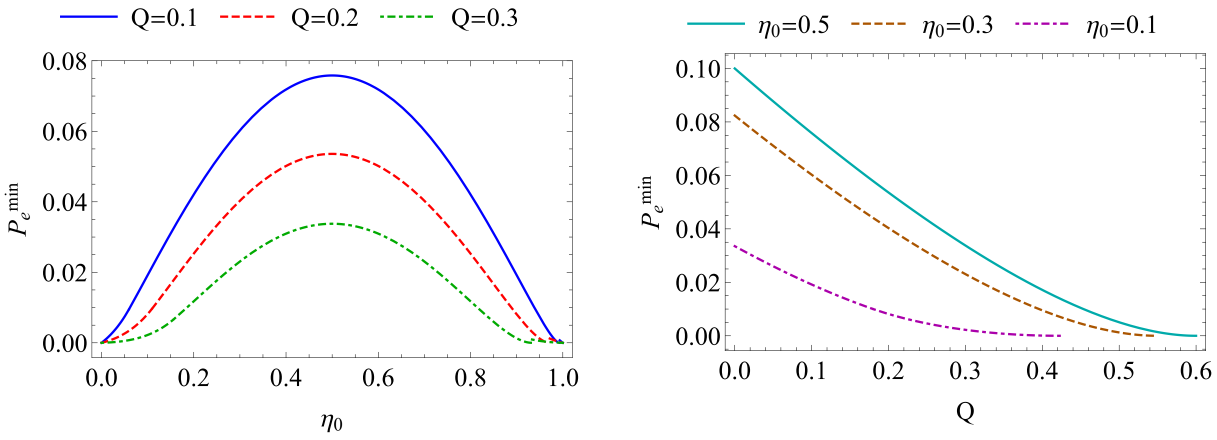

Figure 6 – Probability of error in optimal FRIO discrimination for two pure states of a qubit with a fixed overlap ($\alpha = 0.6$). Left: P_e^{min} as a function of the *a priori* probability η_0 for fixed inconclusive rates (shown in the inset). Right: P_e^{min} as a function of the inconclusive rate Q for fixed *a priori* probabilities (shown in the inset).

2 Discrimination of equiprobable symmetric states

> *"[...] by mathematical arguments you can show that it is possible to start from many apparently different starting points, and yet come to the same thing."*
>
> *The character of physical law, Richard Feynman*

In this chapter, we describe the discrimination between $N > 2$ equiprobable symmetric pure states in arbitrary dimensions. This family of states is of particular interest in quantum communication, as it admits analytical solutions not only for the main strategies discussed in the previous chapter, but also for the new ones that arise in scenarios more complex than the two-state case. First, we review the solutions available in the literature for ME and optimal maximum-confidence (MC) measurements, the latter being a generalization of optimal UD. Then, by approaching a general probabilistic strategy as a discrimination between conclusive and inconclusive events, followed by a ME measurement on the conclusive ones, we derive analytical solutions for the optimal FRIO measurement and show that it interpolates between ME and MC. Finally, we explore a feature that arises only in higher-dimensional systems: the concatenation of two or more optimal discrimination strategies. In particular, we discuss the concatenation of optimal FRIO and ME measurements, showing that it enhances the information gain compared to the optimal FRIO strategy alone.

2.1 N-state discrimination

2.1.1 Problem overview

In the general N-state discrimination problem, we consider a quantum system that is randomly prepared in one of the known states $\{\hat{\rho}_j\}_{j=0}^{N-1}$, with known *a priori* probabilities $\{\eta_j\}_{j=0}^{N-1}$, where $\sum_j \eta_j = 1$. As seen in the previous chapter, for any given measurement strategy, there are two classes of outcomes: conclusive and inconclusive. The former allows us to identify the state, and this identification may be correct or not. The latter does not allow us to identify any state. This scenario can be properly described by an $(N+1)$-outcome POVM $\{\hat{\Pi}_0, \dots, \hat{\Pi}_{N-1}, \hat{\Pi}_?\}$ (with $\sum_j \hat{\Pi}_j + \hat{\Pi}_? = \hat{I}$), where each element $\hat{\Pi}_j$ is associated with a conclusive identification of the state as $\hat{\rho}_j$, while $\hat{\Pi}_?$ is associated with an inconclusive answer. The process is characterized by the average probabilities of erroneous (P_e), correct (P_c), and inconclusive (Q) results, which are given by

$$P_e = \sum_{\substack{j,k=0 \\ j\neq k}}^{N-1} \eta_j \mathrm{Tr}(\hat{\rho}_j \hat{\Pi}_k), \tag{2.1a}$$

$$P_c = \sum_{j=0}^{N-1} \eta_j \mathrm{Tr}(\hat{\rho}_j \hat{\Pi}_j), \tag{2.1b}$$

$$Q = \sum_{j=0}^{N-1} \eta_j \mathrm{Tr}(\hat{\rho}_j \hat{\Pi}_?) = \mathrm{Tr}(\hat{\rho} \hat{\Pi}_?), \tag{2.1c}$$

and satisfy $P_e + P_c + Q = 1$, where $\hat{\rho} = \sum_{j=0}^{N-1} \eta_j \hat{\rho}_j$ is the *a priori* state. Clearly, P_e and P_c are related to the conclusive events. The goal now is to find the POVM that optimizes these probabilities according to a pre-established criterion, with each criterion leading to a different measurement strategy.

2.1.2 Equiprobable symmetric pure states of a qudit

Beyond the cases of two pure qubit states outlined in the previous chapter, deriving analytical solutions to the optimization problem posed by state discrimination becomes increasingly difficult as we move to larger sets or higher-dimensional systems (*qudits*). In these more general cases, few analytical results are known, and numerical optimization techniques are often used to obtain solutions [57, 58]. As mentioned in the Introduction, among the analytically solvable cases, the set of N symmetric, n-dimensional pure states ($N \geq n \geq 2$), prepared with equal *a priori* probabilities (i.e., $\eta_j = 1/N$ for all j), stands out. We now formally define this important family of states.

Let $\{|\alpha_j\rangle\}_{j=0}^{N-1}$ be a set of N symmetric states in an n-dimensional Hilbert space $\mathcal{H}$. The jth state in this set can be written as

$$|\alpha_j\rangle = \sum_{k\in\mathcal{I}} a_k \omega^{jk} |k\rangle, \tag{2.2}$$

where $\mathcal{I} = \{k | a_k \neq 0\}$, with $|\mathcal{I}| = n \leq N$, $a_k > 0$ for all $k \in \mathcal{I}$, and $\sum_{k\in\mathcal{I}} a_k^2 = 1$; $\omega = \exp(2\pi i/N)$ is a primitive Nth root of unity,[1] satisfying the orthogonality relation

$$\sum_{j=0}^{N-1} \omega^{j(k-k')} = N\delta_{k,k'}, \tag{2.3}$$

and $\{|k\rangle\}_{k=0}^{N-1}$ is an orthonormal basis spanning an N-dimensional Hilbert space. Thus, the symmetric states will be linearly independent (dependent) if $n = N$ ($n < N$). $|\alpha_0\rangle$ is often referred to as the *fiducial* state of the set, and all states represented by Eq. (2.2) are related to

---

[1] That is, $\omega^N = 1$ and $\omega^\ell \neq 1$ for all $1 \leq \ell < N$.

$|\alpha_0\rangle$ via a unitary operation $\hat{V}$, whose action is given by

$$|\alpha_j\rangle = \hat{V}|\alpha_{j-1}\rangle = \cdots = \hat{V}^j|\alpha_0\rangle, \tag{2.4a}$$

$$|\alpha_0\rangle = \hat{V}|\alpha_{N-1}\rangle, \tag{2.4b}$$

where

$$\hat{V} = \sum_{k\in\mathcal{I}} \omega^k |k\rangle\langle k|. \tag{2.5}$$

This symmetry under the action of $\hat{V}$ is what characterizes the states $\{|\alpha_j\rangle\}$ in Eq. (2.2) as *symmetric*. Note that Eqs. (2.4) imply that $\hat{V}^N = \hat{I}$, where $\hat{I}$ is the identity operator acting on $\mathcal{H}$.

2.2 Minimum-error discrimination of symmetric states

As a strategy that does not allow inconclusive results (i.e., $Q = 0$), the ME measurement is carried out with an N-outcome POVM, $\{\hat{\Pi}_j^{\text{ME}}\}_{j=0}^{N-1}$. For the equiprobable symmetric states introduced above, this POVM is given by [37, 42]

$$\hat{\Pi}_j^{\text{ME}} = \frac{n}{N}|u_j\rangle\langle u_j|, \tag{2.6}$$

where

$$|u_j\rangle = \frac{1}{\sqrt{n}} \sum_{k\in\mathcal{I}} \omega^{jk}|k\rangle \tag{2.7}$$

are the *uniform* symmetric states. When $n = N$, the POVM reduces to a projective measurement, as we saw in the two-state case.

Using $P_e = 1 - P_c$ together with Eqs. (2.1b), (2.2), (2.6), and (2.7), the minimum average probability of error for discriminating the states is given by

$$\begin{aligned} P_e^{\text{min}} &= 1 - \frac{1}{N}\sum_{j=0}^{N-1} \langle \alpha_j|\hat{\Pi}_j^{\text{ME}}|\alpha_j\rangle \\ &= 1 - \frac{1}{N}\left(\sum_{k\in\mathcal{I}} a_k\right)^2 . \end{aligned} \tag{2.8}$$

The expression above yields an N-state version of the Helstrom bound, under the requirement that the states to be discriminated are symmetric and equiprobable. Since the case $N = 2$ is trivially symmetric, we can immediately recover the result found in Sec. 1.2.1 [see Eq. (1.18)] for the equiprobable scenario:

$$\begin{aligned} P_e^{\text{min}} &= 1 - \frac{1}{2}(1 + 2a_0a_1) \\ &= \frac{1}{2}\left(1 - \sqrt{1-\alpha^2}\right), \end{aligned} \tag{2.9}$$

where $\alpha = \langle \alpha_0|\alpha_1\rangle$ is the overlap between the states.

2.3 Maximum-confidence discrimination of symmetric states

As mentioned in Sec. 1.2.2, the UD strategy is not applicable to linearly dependent quantum states [17]. In such cases, however, it is possible to design an analogous optimized measurement scheme whose conclusive outcomes identify the states in a given set with the maximum possible confidence,[2] while the inconclusive rate is minimum [18]. To describe the so-called optimal maximum-confidence (MC) measurement and its solution for equiprobable symmetric states, let us first mathematically define what confidence is:

Definition 2.1. *In the N-state discrimination problem stated in Sec. 2.1.1, given the N conclusive outcomes associated with the* POVM *elements $\{\hat{\Pi}_j\}_{j=0}^{N-1}$, the confidence C_j is defined as the probability that the prepared state was $\hat{\rho}_j$, given that the outcome of the measurement was j. According to Bayes' rule:*

$$C_j \equiv P(\hat{\rho}_j|j) = \frac{P(\hat{\rho}_j)P(j|\hat{\rho}_j)}{P(j)} = \frac{\eta_j \mathrm{Tr}\left(\hat{\rho}_j \hat{\Pi}_j\right)}{\mathrm{Tr}\left(\hat{\rho}\hat{\Pi}_j\right)}. \tag{2.10}$$

In the particular case of pure states, the POVM element that maximizes C_j is given by [18]

$$\hat{\Pi}_j = c_j \hat{\rho}^{-1}\hat{\rho}_j\hat{\rho}^{-1}, \tag{2.11}$$

where $c_j = \mathrm{Tr}(\hat{\Pi}_j\hat{\rho})/\mathrm{Tr}(\hat{\rho}^{-1}\hat{\rho}_j)$ is a nonnegative real weighting factor. By inserting this operator into Eq. (2.10), we obtain the maximum confidence

$$C_j^{\max} = \eta_j \mathrm{Tr}(\hat{\rho}_j\hat{\rho}^{-1}). \tag{2.12}$$

Equation (2.10) shows that c_j has no effect on the confidence. Therefore, each operator $\hat{\Pi}_j$ can only be determined up to an arbitrary multiplicative factor, allowing us to maximize C_j for each state independently. If these operators do not form a POVM for any choice of factors $\{c_j\}$, i.e., $\sum_j \hat{\Pi}_j < \hat{I}$, then an inconclusive result must be included, with the corresponding POVM element given by $\hat{\Pi}_? = \hat{I} - \sum_j \hat{\Pi}_j$. The MC measurement is further optimized by minimizing the inconclusive rate Q [see Eq. (2.1c)], subject to the constraint $\hat{\Pi}_? \geq 0$.

In the case of equiprobable symmetric states, using Eqs. (2.2) and (2.3), we have

$$\hat{\rho} = \frac{1}{N}\sum_{j=0}^{N-1} |\alpha_j\rangle\langle\alpha_j| = \sum_{k\in\mathcal{I}} a_k^2 |k\rangle\langle k| \quad \Rightarrow \quad \hat{\rho}^{-1} = \sum_{k\in\mathcal{I}} a_k^{-2}|k\rangle\langle k|. \tag{2.13}$$

By substituting $\hat{\rho}$ and $\hat{\rho}^{-1}$ into Eq. (2.12), we obtain

$$C_j^{\max} = \frac{n}{N} \equiv C^{\mathrm{MC}}. \tag{2.14}$$

---

[2] In UD, conclusive results identify each state with 100% confidence.

Thus, the maximum achievable confidence for identifying $|\alpha_j\rangle$ when outcome j is obtained is n/N for each state in the set. The corresponding POVM element is calculated from Eq. (2.11) to be

$$\hat{\Pi}_j^{\text{MC}} = c_j |\phi_j\rangle\langle\phi_j|, \tag{2.15}$$

where

$$|\phi_j\rangle = \sum_{k\in\mathcal{I}} a_k^{-1} \omega^{-jk} |k\rangle \tag{2.16}$$

are also symmetric states with respect to the unitary $\hat{V}$ given by Eq. (2.5). Using Eqs. (2.15) and (2.16), exploiting the symmetries in the problem, applying the constraint $\hat{\Pi}_? \geq 0$, and minimizing the inconclusive rate, it can be shown that [37] $c_j = a_{\text{min}}^2/N$ for all j,

$$\hat{\Pi}_? = \sum_{k\in\mathcal{I}} \left(1 - \frac{a_{\text{min}}^2}{a_k^2}\right) |k\rangle\langle k|, \tag{2.17}$$

and

$$Q^{\text{min}} = 1 - n a_{\text{min}}^2 \equiv Q^{\text{MC}}, \tag{2.18}$$

where $a_{\text{min}} \equiv \min\{a_k\}_{k\in\mathcal{I}}$.

For linearly independent symmetric states ($n = N$), Eq. (2.14) shows that $C_j^{\text{max}} = 1$ for each input. Thus, these states can be distinguished without error and with the minimum inconclusive rate given by Eq. (2.18), showing that optimal MC reduces to optimal UD [43] in this case. In particular, considering the two-state UD protocol described in Sec. 1.2.2, Eqs. (2.17) and (2.18) yield $\hat{\Pi}_? = (1 - \tan^2\theta)|0\rangle\langle 0|$ and $Q^{\text{UD}} = 1 - 2\sin^2\theta = \cos 2\theta = \alpha$, respectively.

It is also worth establishing a comparison between optimal MC and ME measurements, which can be done by evaluating the confidence achieved by the latter. In the case of equiprobable symmetric states, using the ME POVM from Eq. (2.6) in Eq. (2.10), we find that each state in the set is identified with the same confidence, $C^{\text{ME}} = P_c^{\text{max}} = 1 - P_e^{\text{min}}$, with P_e^{min} given by Eq. (2.8). Additionally, using the Cauchy-Schwarz inequality, we obtain

$$C^{\text{ME}} = \frac{1}{N}\left(\sum_{k\in\mathcal{I}} a_k\right)^2 \leq \frac{n}{N} = C^{\text{MC}}, \tag{2.19}$$

showing that the confidence achieved by the conclusive outcomes in the MC measurement is a tight upper bound for the confidence in the ME strategy. This inequality is saturated only when the symmetric states are uniform, i.e., $a_k = 1/\sqrt{n}$ for all $k \in \mathcal{I}$. In this case, $\hat{\Pi}_? = \hat{0}$ and $Q = 0$, and the two strategies coincide.

2.4 Optimal FRIO discrimination of symmetric states

As discussed in Sec. 1.2.3, the ME and optimal UD measurements are extreme and particular cases of the optimal FRIO strategy, in which the error probability P_e is minimized under the constraint that the rate of inconclusive results Q has a fixed value in the range $0 \leq Q \leq Q^{\text{UD}}$, yielding $P_e^{\min}(Q)$. In ME, where inconclusive results are not allowed, P_e is minimized subject to $Q = 0$ (and hence $\hat{\Pi}_? = \hat{0}$). In optimal UD, the measurement must provide the minimum rate of inconclusive outcomes $Q = Q^{\text{UD}}$ subject to $P_e^{\min}(Q^{\text{UD}}) = 0$. As shown in Ref. [22], the optimal MC measurement is also an extreme case of optimal FRIO for $Q = Q^{\text{MC}}$, but only when the maximum confidence $C_j^{\max}$ [Eq. (2.12)] is the same for each of the N states to be discriminated—a condition that holds for equiprobable symmetric states [see Eq. (2.14)]. Therefore, for the family of states considered in this work, we can state in general that the optimal FRIO measurement interpolates between the ME and optimal MC strategies within the range $0 \leq Q \leq Q^{\text{MC}}$, where MC corresponds to UD for linearly independent states.[3]

The state discrimination strategies outlined in this work yield conclusive outcomes with probability $1 - Q$. In this sense, ME is a deterministic strategy, whereas those with $Q > 0$ are probabilistic. Yet there is a fundamental connection between them: probabilistic strategies can be decomposed into a discrimination between conclusive and inconclusive events, followed by a ME measurement on the conclusive ones [35–38]. Here, we describe the optimal FRIO strategy for discriminating equiprobable symmetric states using this two-step approach, and derive analytical solutions for the probabilities given by Eq. (2.1). This approach will also play a key role in the studies presented in the remaining chapters of this thesis.

2.4.1 Optimal parametric separation of symmetric states

Quantum state separation is a probabilistic map that transforms pure states into more distinguishable pure states[4] [35, 59, 60]. This map can be physically implemented as a two-outcome POVM, where one outcome corresponds to a successful transformation and the other to failure, resulting in output states that are less distinguishable than the inputs.

In Ref. [23], the authors proposed an optimal state separation scheme for the equally likely symmetric states defined in Eq. (2.2). This scheme proceeds as follows. First, a two-dimensional ancilla prepared in a pure state $|1\rangle_a$ is attached to the main system, resulting in the bipartite state $|\alpha_j\rangle|1\rangle_a$. Next, both systems are coupled through a unitary operation acting on

---

[3] It is important to stress that, within the range $Q^{\text{MC}} < Q < 1$, the minimum error probability conditioned on obtaining a conclusive result for a fixed Q, namely $P_e^{\min}(Q)/(1 - Q)$, remains constant [22], and the corresponding MC measurement becomes suboptimal.

[4] If this were not a probabilistic map, one could apply it to transform nonorthogonal states into perfectly distinguishable orthogonal states in a deterministic way, thus contradicting the rules of quantum theory.

$\mathcal{H} \otimes \mathcal{H}_a$ as

$$\hat{\mathcal{U}}(\xi)|\alpha_j\rangle|1\rangle_a = \sqrt{P_s(\xi)}|\beta_j(\xi)\rangle|1\rangle_a + \sqrt{P_f(\xi)}|\tilde{\beta}_j\rangle|0\rangle_a. \tag{2.20}$$

In this expression, $\xi \in [0,1]$, $\{|0\rangle_a, |1\rangle_a\}$ is an orthonormal basis for $\mathcal{H}_a$, and the output states resulting from success and failure in the process are given, respectively, by

$$|\beta_j(\xi)\rangle = \sum_{k\in\mathcal{I}} b_k(\xi)\omega^{jk}|k\rangle, \tag{2.21a}$$

$$|\tilde{\beta}_j\rangle = \sum_{k\in\mathcal{I}} \tilde{b}_k\omega^{jk}|k\rangle, \tag{2.21b}$$

where the corresponding coefficients are

$$b_k^2(\xi) = (1-\xi)a_k^2 + \frac{\xi}{n}, \tag{2.22a}$$

$$\tilde{b}_k^2 = \frac{a_k^2 - a_{\text{min}}^2}{1 - na_{\text{min}}^2}; \tag{2.22b}$$

$P_s(\xi)$ $[P_f(\xi)]$ denotes the optimal success (failure) probability and is given by

$$P_s(\xi) = \frac{na_{\text{min}}^2}{(1-\xi)na_{\text{min}}^2 + \xi} = 1 - P_f(\xi), \tag{2.23}$$

where $a_{\text{min}} = \min\{a_k\}_{k\in\mathcal{I}}$. Finally, after this coupling, the ancilla is measured in the basis $\{|0\rangle_a, |1\rangle_a\}$: the projection onto $|1\rangle_a$ occurs with probability $P_s(\xi)$ and leads to the desired transformation $|\alpha_j\rangle \to |\beta_j(\xi)\rangle$, otherwise the process fails with probability $P_f(\xi)$ and $|\alpha_j\rangle \to |\tilde{\beta}_j\rangle$.

In the process outlined above, the parameter ξ sets the degree of separation of the states $|\beta_j(\xi)\rangle$. In the extreme cases, it is easy to verify that for $\xi = 0$, there is no change in the inputs ($|\beta_j(0)\rangle = |\alpha_j\rangle$), whereas for $\xi = 1$, the successfully transformed states become maximally distinguishable,[5] i.e., $|\beta_j(1)\rangle = |u_j\rangle$ [see Eq. (2.7)]. In the range $0 < \xi \leq 1$, we show in Appendix 6 that $|\langle\beta_i(\xi)|\beta_j(\xi)\rangle| < |\langle\alpha_i|\alpha_j\rangle|$ for all $i \neq j$, which implies that the states in $\{|\beta_j(\xi)\rangle\}$ are more distinguishable than those in $\{|\alpha_j\rangle\}$. We also demonstrate that this distinguishability increases monotonically with ξ. The successful separation occurs with the maximum probability $P_s(\xi)$, defined in Eq. (2.23).[6]

The states $\{|\tilde{\beta}_j\rangle\}_{j=0}^{N-1}$ resulting from a failure in the process are independent of ξ [see Eq. (2.21b)]. Denoting the multiplicity of a_{min} as μ, they will then span an $(n-\mu)$-dimensional space, since $1 \leq \mu \leq n$ of their coefficients vanish [see Eq. (2.22b)]. Therefore, when the separation fails with the minimum probability $P_f(\xi)$, the output states become less distinguishable

---

[5] For instance, when $N = n$, the states $\{|u_j\rangle\}$ are orthonormal.

[6] In the case of parallel input states ($a_k = \delta_{k,l}$), where no separation is possible, we have two scenarios: (i) if $\xi > 0$, we assume $a_{\text{min}} = 0$, which ensures that $P_s(\xi > 0) = 0$; (ii) if $\xi = 0$, $P_s(1) = 1$, but $\hat{\mathcal{U}} = \hat{I}$.

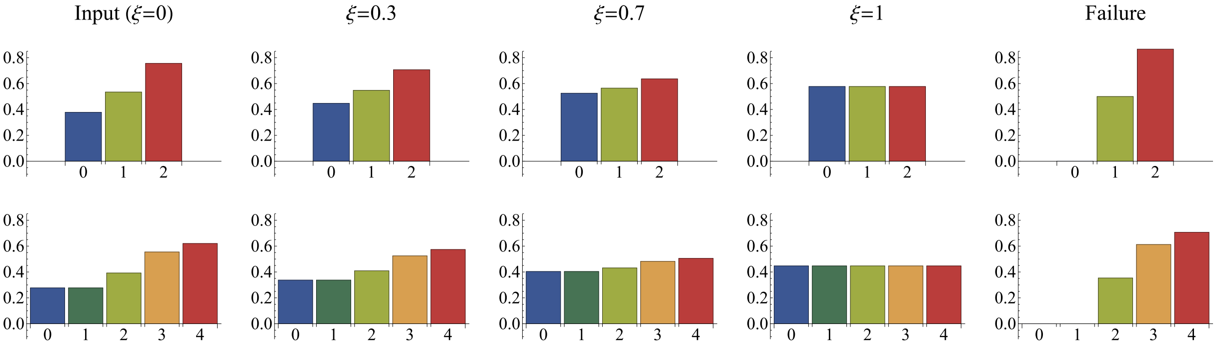

Figure 7 – Coefficients of the input states $\{a_k\}$ (first column), successful output states $\{b_k\}$ (from second to fourth columns), and failure output states $\{\tilde{b}_k\}$ (fifth column) for dimensions $n = 3$ (top row) and $n = 5$ (bottom row); we used separation parameters $\xi = 0.3, 0.7, 1$.

than the inputs (see Appendix 6), but will still carry information about them if $n - \mu > 1$. In Sec. 2.5, we explore the possibility of extracting this information.

The detection operators associated with the success and failure outcomes in the separation of equiprobable symmetric states are, respectively, given by

$$\hat{A}_s(\xi) = {}_a\langle 1|\hat{\mathcal{U}}(\xi)|1\rangle_a, \tag{2.24a}$$

$$\hat{A}_f(\xi) = {}_a\langle 0|\hat{\mathcal{U}}(\xi)|1\rangle_a \tag{2.24b}$$

where $\hat{\mathcal{U}}(\xi)$ is the unitary defined in Eq. (2.20). Thus, the two-outcome POVM on $\mathcal{H}$ that describes the process is $\mathbf{\Pi}_{\text{SEP}} = \{\hat{A}_s^\dagger(\xi)\hat{A}_s(\xi), \hat{A}_f^\dagger(\xi)\hat{A}_f(\xi)\}$.[7]

To illustrate the state separation protocol, we evaluate its effect on the coefficients of the output states resulting from success [Eq.(2.22a)] and failure [Eq.(2.22b)] outcomes. In the first column of Fig. 7, we plot the coefficients $\{a_k\}$ of the input states for dimensions $n = 3$ (top row) and $n = 5$ (bottom row). Columns two to four show the coefficients of the successful output states, $\{b_k(\xi)\}$, for $\xi = 0.3$, 0.7, and 1, respectively. Column five displays the coefficients of the failure output states, $\{\tilde{b}_k\}$, which are independent of ξ. In the case of success, the amplitudes larger than a_{min} are attenuated as ξ increases, and $\{b_k(\xi)\}$ approaches $1/\sqrt{n}$, which are the coefficients of a uniform state (see plots with $\xi = 1$). As discussed above, in the case of failure, the output states lie in an $(n - \mu)$-dimensional space. In the example with $n = 3$, we have $\mu = 1$, so the failure states are two-dimensional; for $n = 5$, we have $\mu = 2$, and the failure states span a three-dimensional space.

---

[7] The positivity of $\hat{A}^\dagger_{s(f)}(\xi)\hat{A}_{s(f)}(\xi)$ is straightforward to show. To demonstrate completeness, we proceed as follows: from the definition of the detection operators in Eq. (2.24), given an arbitrary state $|\psi\rangle \in \mathcal{H}$, we have $\hat{\mathcal{U}}(\xi)|\psi\rangle|1\rangle_a = \hat{A}_s(\xi)|\psi\rangle|1\rangle_a + \hat{A}_f(\xi)|\psi\rangle|0\rangle$. The unitarity of $\hat{\mathcal{U}}(\xi)$ implies that $\langle\psi|\hat{A}_s^\dagger(\xi)\hat{A}_s(\xi)|\psi\rangle + \langle\psi|\hat{A}_f^\dagger(\xi)\hat{A}_f(\xi)|\psi\rangle = \langle\psi|\psi\rangle$. Since this holds for all $|\psi\rangle \in \mathcal{H}$, it follows that $\hat{A}_s^\dagger(\xi)\hat{A}_s(\xi) + \hat{A}_f^\dagger(\xi)\hat{A}_f(\xi) = \hat{I}$.

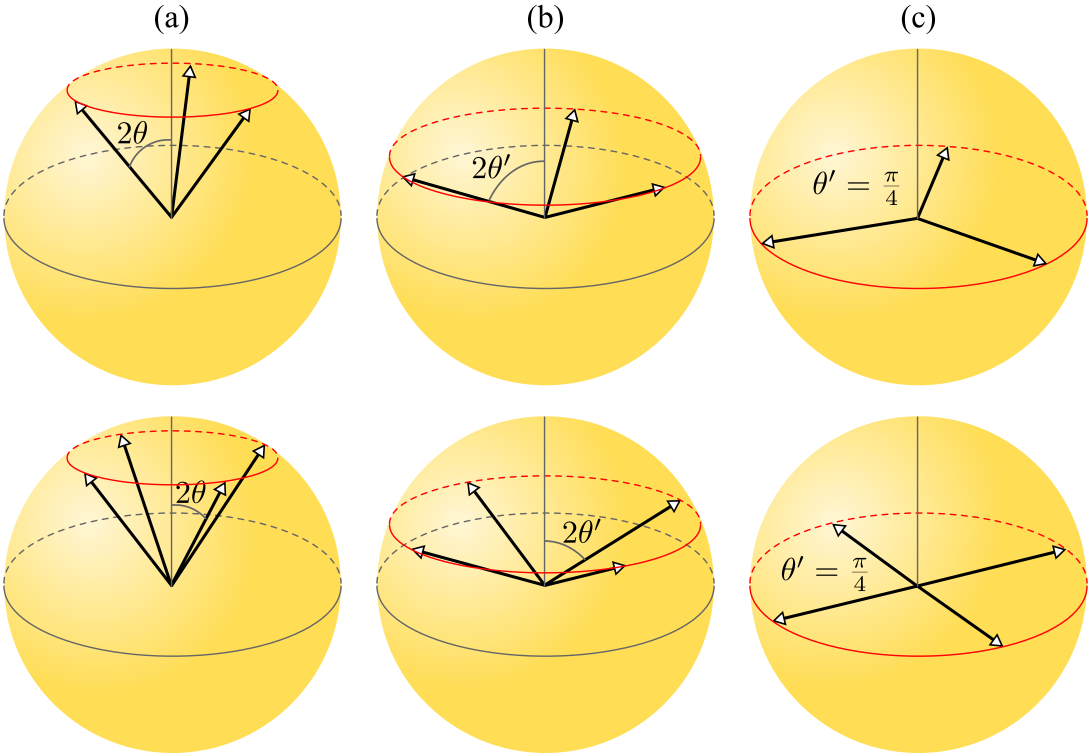

Figure 8 – Symmetric states of a qubit on the Bloch sphere for $N = 3$ (first row) and $N = 4$ (second row). (a) Input states [Eq. (2.25)]; (b) output states separated by $\theta < \theta' < \pi/4$ [Eq. (2.26)]; (c) output states maximally separated [Eq. (2.27)].

2.4.1.1 Qubit case

For the case of qubits, which will be experimentally addressed in the next chapter, the N symmetric states given in Eq. (2.2) can be expressed in terms of the polar angle on the Bloch sphere as

$$|\alpha_j(\theta)\rangle = \cos\theta|0\rangle + \omega^j \sin\theta|1\rangle, \tag{2.25}$$

where $0 \leq \theta \leq \pi/4$ and $\{|0\rangle, |1\rangle\}$ are the states at the poles of the sphere. Under the action of $\hat{V}^j = |0\rangle\langle 0| + \omega^j|1\rangle\langle 1|$, the fiducial state $|\alpha_0(\theta)\rangle$ is rotated around the z-axis of the Bloch sphere by an azimuthal angle $2\pi j/N$ while keeping its polar angle 2θ. The N states generated in this way are symmetrically distributed along the parallel of latitude $\pi/2 - 2\theta$ north of the Bloch sphere equator, as sketched in Fig. 8(a) for $N = 3$ (first row) and $N = 4$ (second row).

In the separation process, let us express the successfully transformed states as

$$|\beta_j(\theta')\rangle = \cos\theta'|0\rangle + \omega^j \sin\theta'|1\rangle, \tag{2.26}$$

where, using Eq. (2.22a), we find $\theta' = \arccos\left(\sqrt{(1-\xi)\cos^2\theta + \xi/2}\right)$. This angle ranges from θ to $\pi/4$ as ξ varies in the interval $[0, 1]$. Therefore, successful separation is characterized by an increase in the polar angle of the inputs, with the resulting symmetric states $|\beta_j(\theta')\rangle$ lying on a parallel of the Bloch sphere that is closer to the equator than before, as shown in Fig. 8(b). In particular, when $\theta' = \pi/4$, the separation is maximal and the output states become uniform:

$$|\beta_j(\pi/4)\rangle = \frac{1}{\sqrt{2}}(|0\rangle + \omega^j|1\rangle). \tag{2.27}$$

These states are located on the equator of Bloch sphere, as shown in Fig. 8(c).

By using Eqs. (2.22a), (2.25), and (2.26), we can write the separation parameter ξ as a function of the output polar angle θ':

$$\xi(\theta') = \frac{2(\sin^2\theta' - \sin^2\theta)}{\cos 2\theta}. \tag{2.28}$$

Then, using the above relation and the fact that $a_{\text{min}} = \sin\theta$, we can express the optimal success probability of state separation [Eq. (2.23)] in terms of the input and output polar angles, which yields

$$P_s(\theta') = \left(\frac{\sin\theta}{\sin\theta'}\right)^2. \tag{2.29}$$

Note that for $\theta' = \pi/4$, we have $P_s = 2\sin^2\theta = 1 - Q^{\text{MC}}$, which corresponds to the success probability of the optimal MC strategy.

The separation process fails with probability $P_f(\theta') = 1 - P_s(\theta')$. In this case, using Eq. (2.22b), we have $\tilde{b}_0 = 1$ and $\tilde{b}_1 = 0$, so that $|\alpha_j(\theta)\rangle \to |0\rangle$ for all j, which results in no information remaining about the input states.

2.4.2 Optimal FRIO discrimination as a two-step process

The successfully separated states, namely, $\{|\beta_j(\xi)\rangle\}_{j=0}^{N-1}$ given by Eq. (2.21a), also form a set of N equally likely symmetric states. Assume that one wants to discriminate them with a ME strategy, whose POVM is given by Eq. (2.6). Denoting the minimum average error probability in this case as $p_e^\beta(\xi)$, we obtain

$$\begin{aligned} p_e^\beta(\xi) &= 1 - \frac{1}{N}\sum_{j=0}^{N-1}\langle\beta_j(\xi)|\hat{\Pi}_j^{\text{ME}}|\beta_j(\xi)\rangle \\ &= 1 - \frac{1}{N}\left(\sum_{k\in\mathcal{I}} b_k(\xi)\right)^2. \end{aligned} \tag{2.30}$$

Using the above result, we now show that the optimal FRIO discrimination of N equiprobable symmetric states can be decomposed into two steps: an optimal state separation followed by a ME measurement on the successful outputs. This two-step process is represented by an $(N+1)$-outcome POVM $\mathbf{\Pi}_{\text{FRIO}} = \{\hat{\Pi}_0(\xi), \ldots, \hat{\Pi}_{N-1}(\xi), \hat{\Pi}^?(\xi)\}$, where the associated detection operators $\{\hat{A}_j(\xi)\}_{j=0}^{N-1}$ and $\hat{A}^?(\xi)$ are given by the compositions of the detection operators corresponding to each measurement in the sequence. Thus, using Eqs. (2.6) and (2.24), it follows that

$$\hat{A}_j(\xi) = \sqrt{\hat{\Pi}_j^{\text{ME}}}\hat{A}_s(\xi), \tag{2.31a}$$

$$\hat{A}^?(\xi) = \hat{A}_f(\xi) \tag{2.31b}$$

are the detection operators associated with a conclusive identification of the input state (whether it is correct or not) and an inconclusive answer, respectively. It is easy to verify that the operators $\{\hat{\Pi}_j(\xi) = \hat{A}_j^\dagger(\xi)\hat{A}_j(\xi)\}$ and $\hat{\Pi}^?(\xi) = [\hat{A}^?(\xi)]^\dagger \hat{A}^?(\xi)$ are positive semidefinite and satisfy $\sum_j \hat{\Pi}_j(\xi) + \hat{\Pi}^?(\xi) = \hat{I}$. Using this POVM and Eqs. (2.6), (2.20), (2.21a), and (2.22a) we obtain the average probabilities of Eq. (2.1) as functions of ξ, the degree of separation:

$$P_e(\xi) = P_s(\xi) p_e^\beta(\xi), \tag{2.32a}$$

$$P_c(\xi) = P_s(\xi)\left[1 - p_e^\beta(\xi)\right], \tag{2.32b}$$

$$Q(\xi) = P_f(\xi), \tag{2.32c}$$

where $P_s(\xi) = 1 - P_f(\xi)$ is given by Eq. (2.23).

Equations (2.32) make explicit the connection between the two steps and the optimal FRIO discrimination. After the separation, if no further measurement is carried out on the less distinguishable failure output states, no information about the inputs can be obtained. Thus, the inconclusive rate equals the failure probability of the separation step. On the other hand, a successful separation will lead to a conclusive outcome for the discrimination attempt, and indeed we see that $P_e(\xi) + P_c(\xi) = P_s(\xi)$. The fixed value of $Q \in [0, Q^{\text{MC}}]$ is set at the state separation stage by choosing $\xi \in [0, 1]$; from Eq. (2.23), we have $Q(0) = 0$ and $Q(1) = 1 - na_{\text{min}}^2 = Q^{\text{MC}}$.

In terms of the two-step process, the figure of merit of the optimal FRIO measurement, $P_e^{\text{min}}(Q)$, is given by

$$P_e^{\text{min}}(Q) = (1 - Q) p_e^\beta(Q). \tag{2.33}$$

To derive an explicit expression for this probability, we first isolate ξ in Eq. (2.23), obtaining $\xi(Q) = Q(1 - Q^{\text{MC}})/Q^{\text{MC}}(1 - Q)$. Then, using Eqs. (2.22a) and (2.30), we find

$$P_e^{\text{min}}(Q) = 1 - Q - \frac{1}{N}\left(\sum_{k\in\mathcal{I}} \sqrt{\frac{a_{\text{min}}^2 Q + a_k^2(Q^{\text{MC}} - Q)}{Q^{\text{MC}}}}\right)^2. \tag{2.34}$$

It is easy to verify that the ME and optimal MC strategies emerge as particular cases of the optimal FRIO for $Q = 0$ and $Q = Q^{\text{MC}}$, respectively. In the first case, we find the Helstrom bound, i.e., $P_e^{\text{min}}(0)$ is given by Eq. (2.8). In the second case

$$P_e^{\text{min}}(Q^{\text{MC}}) = (1 - Q^{\text{MC}})(1 - C^{\text{MC}}), \tag{2.35}$$

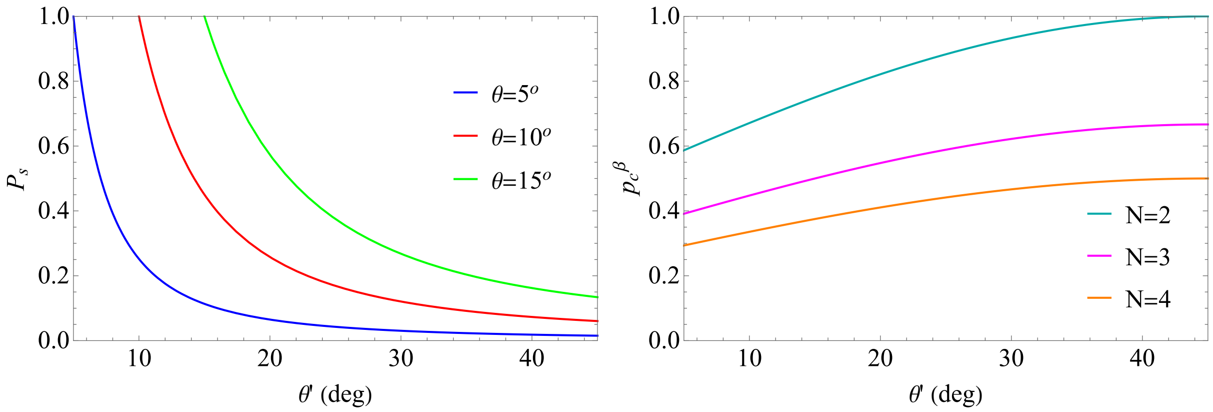

Figure 9 – Left: Average success probability of state separation (P_s) vs output angle (θ') [Eq. (2.29)] for the input angles θ shown in the inset. Right: Average probability of correctly discriminating the separated states ($p_c^\beta = 1 - p_e^\beta$) vs θ' [Eq. (2.37)] for N input states (see inset).

where $C^{\text{MC}} = n/N$ is the maximum confidence achieved for each of the N symmetric states [see Eq. (2.14)]. When $N = n$, the optimal UD strategy is recovered, for which the zero-error condition holds: $P_e^{\min}(Q^{\text{UD}}) = 0$. The solution given by (2.34) is valid in the range $0 \le Q \le Q^{\text{MC}}$. In the complementary interval, $Q^{\text{MC}} \le Q \le 1$, the convexity of $P_e^{\min}(Q)$ [21] implies that the solution is given by $P_e^{\min}(Q) = (1-Q)(1-C^{\text{MC}})$. Therefore, the minimum *relative* error rate $p_e^{(\beta)}(Q) = P_e^{\min}(Q)/(1-Q)$ becomes constant for $Q \ge Q^{\text{MC}}$, and Q^{MC} represents a critical value for the inconclusive rate. Above this threshold, the MC measurement is suboptimal: although it achieves maximum confidence, Q is no longer minimal.

Equation (2.34) shows that the error probability increases with the number of states to be discriminated. In the limit $N \to \infty$, we have

$$\lim_{N\to\infty} P_e^{\min}(Q) = 1 - Q, \tag{2.36}$$

so only erroneous or inconclusive answers can be obtained.

2.4.2.1 Qubit case

For symmetric qubit states, the separation process succeeds with probability $P_s(\theta')$ [Eq. (2.29)]. According to Eq. (2.30), the minimum average error probability for discriminating the successfully separated states (2.26), will be given by

$$p_e^\beta(\theta') = 1 - \frac{1}{N}(1 + \sin 2\theta'). \tag{2.37}$$

We now analyze the behavior of these two probabilities, from which $P_e(\theta')$, $P_c(\theta')$, and $Q(\theta')$ can be derived, as shown in Eqs. (2.32). In the left panel of Fig. 9, P_s is plotted as a function of

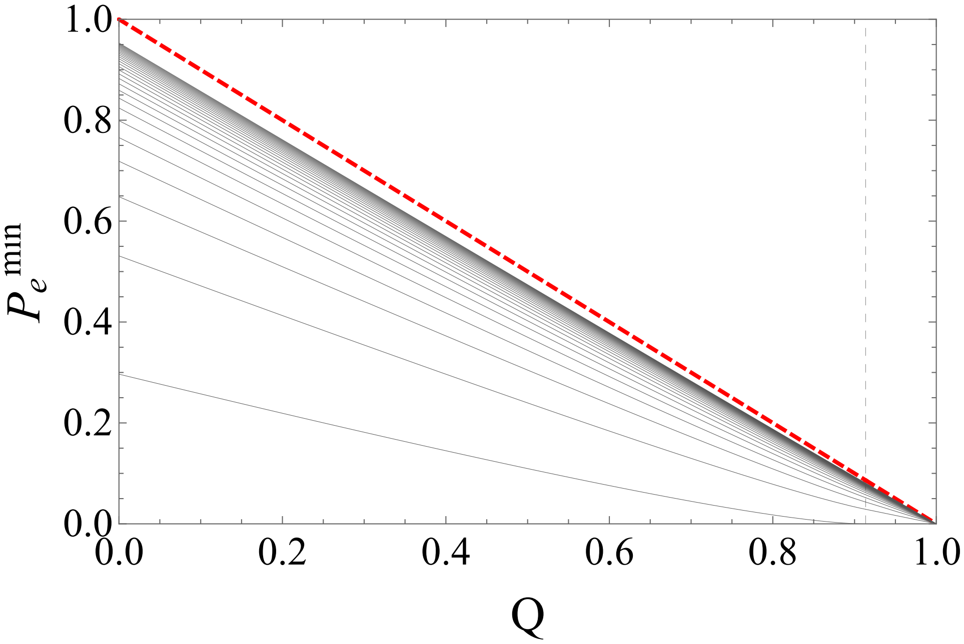

Figure 10 – Average error probability ($P_e^{\min}$) vs inconclusive rate (Q) for N input states (solid gray lines). From bottom to top, N ranges from 2 to 30. The dashed vertical line represents the critical inconclusive rate $Q = Q^{\text{MC}}$ and the dashed red line corresponds to the asymptotic limit [Eq. (2.36)]. The input states were fixed with polar angle $\theta = \pi/15$ in the Bloch sphere.

the output angle θ' for three input angles $\theta = 5°, 10°$, and $15°$. It decreases with θ', indicating that extracting greater distinguishability from the inputs comes at the cost of lower success rates. On the other hand, it increases with θ, since more distinguishable input states are easier to separate, resulting in higher success rates. In the right panel of Fig. 9, we plot $p_c^\beta = 1 - p_e^\beta$ as a function of θ' for $N = 2, 3$, and 4 input states. It increases with θ', as a result of the increased distinguishability of the successful output states. On the other hand, it decreases with N, as increasing the number of states reduces their distinguishability.

After some algebraic manipulation of Eq. (2.34), we obtain the minimum error probability $P_e^{\min}(Q)$ for the qubit case as

$$P_e^{\min}(Q) = \frac{1}{N}\left[(N-1)\bar{Q} - \sqrt{\bar{Q}^2 - (Q - Q^{\text{MC}})^2}\right], \tag{2.38}$$

where $\bar{Q} = 1 - Q$ and $0 \leq Q \leq Q^{\text{MC}}$; for $Q^{\text{MC}} \leq Q \leq 1$, $P_e^{\min}(Q) = \bar{Q}(1 - 2/N)$. This solution is in agreement with previous results in the literature [21,22,35]. In particular, by making $N = 2$, we recover the two-state solution discussed in Sec. 1.2.3 [see Eq. (1.34) with $Q_0 = Q^{\text{MC}}$].

In Fig. 10, we plot the minimum average error rate as a function of the inconclusive rate. The input set is defined by the polar angle $\theta = \pi/15$ and the number of states in the set ranges from $N = 2$ (bottom) to $N = 30$ (top). The dashed red line corresponds to the asymptotic limit given by Eq. (2.36); the dashed black line represents the critical inconclusive rate $Q = Q^{\text{MC}}$. The error rate decreases monotonically with the inconclusive rate and increases with the number of states to be discriminated. Moreover, as N increases, the corresponding curves approach the asymptotic bound more rapidly for large values of Q.

2.5 Concatenated FRIO discrimination of symmetric states

2.5.1 Standard and concatenated discrimination strategies

As shown in the previous section, a failure in the separation process results in the map $|\alpha_j\rangle \xrightarrow{\text{fail}} |\tilde{\beta}_j\rangle$, where the states $|\tilde{\beta}_j\rangle$ [Eqs. (2.21b) and (2.22b)] span an $(n-\mu)$-dimensional space, with $1 \leq n-\mu \leq n-1$. Depending on the value of $n-\mu$, the following scenarios may arise:

a) $n-\mu = 1$: The failure states are identical and therefore cannot provide more information about the inputs than a random guess, making any subsequent discrimination attempt useless. This is always the case for qubit states ($|\alpha_j(\theta')\rangle \xrightarrow{\text{fail}} |0\rangle$ for all j), where a failed separation implies inconclusive discrimination.

b) $n-\mu > 1$: This condition can only be achieved with qudits. Here, the failure states still carry information about the inputs,[8] although less than what can be extracted from the successfully separated states. Two types of strategies emerge from this scenario:

    (i) **Standard strategies:** Refraining from discriminating the failure states leads to inconclusive outcomes. The probabilistic discrimination strategies discussed so far follow this approach and will be referred to as *standard* strategies.

    (ii) **Concatenated strategies:** The failure states are linearly dependent and can be discriminated via ME, optimal MC, or optimal FRIO measurements. Strategies in which these states are discriminated will be referred to as *concatenated* strategies.

Since the early developments of probabilistic state discrimination in higher dimensions, several works have addressed the possibility of retrieving information from failure events [17, 37, 61–66]. Recently, the concatenation of optimal UD and ME measurements was experimentally demonstrated [41]. Concatenated discrimination strategies avoid discarding useful information—as in the standard case—and have been shown to yield significant improvements in probabilistic

---

[8] To understand this, let us consider the case of symmetric states. Using the triangle inequality, the magnitude of the overlap between an input state $|\alpha_i\rangle$ [Eq. (2.2)] and a failure output state $|\tilde{\beta}_j\rangle$ [Eq. (2.21b)] satisfies $|\langle\alpha_i|\tilde{\beta}_j\rangle| = |\sum_\ell \omega^{\ell(j-i)} a_\ell \tilde{b}_\ell| \leq \sum_\ell |a_\ell \tilde{b}_\ell| = |\langle\alpha_i|\tilde{\beta}_i\rangle|$, where the equality holds only for $i = j$. Thus, the overlap magnitudes are maximized when the indices match, which implies that identifying $|\tilde{\beta}_j\rangle$ yields a higher probability of correctly inferring the input as $|\alpha_j\rangle$. In the case $n-\mu = 1$, $|\langle\alpha_i|\tilde{\beta}_j\rangle|$ takes the same value for all i, j.

implementations of quantum teleportation [39], entanglement swapping [40], dense coding, and quantum key distribution [24].

2.5.2 Concatenating optimal FRIO and ME measurements

There are several ways to concatenate two or more state discrimination strategies, depending on which figure of merit one seeks to improve compared to the standard strategy. In this work, we study and apply the concatenation of optimal FRIO and ME measurements, which we refer to as concatenated FRIO.[9] In this strategy, the inconclusive outcome of standard FRIO is unfolded into N outcomes from the ME measurement on the failure states. Thus, it is represented by a $2N$-outcome POVM $\mathbf{\Pi}_{\text{CONC}} = \{\hat{\Pi}_j(\xi), \hat{\Pi}_j^f(\xi)\}_{j=0}^{N-1}$, where $\hat{\Pi}_j(\xi)$ and $\hat{\Pi}_j^f(\xi)$ are the elements associated with a conclusive identification of the input state after successful and failed separations, respectively.

For equiprobable symmetric input states, the set of detection operators $\hat{A}_j(\xi)$ corresponding to $\hat{\Pi}_j(\xi)$ remains unchanged from the standard case [see Eq. (2.31a)]. On the other hand, the detection operators $\hat{A}_j^f(\xi)$ associated with $\hat{\Pi}_j^f(\xi)$ must now incorporate the ME measurement given by Eq. (2.6), since the failure output states [Eq. (2.21b)] are also symmetric and equiprobable. Therefore,

$$\hat{A}_j(\xi) = \sqrt{\hat{\Pi}_j^{\text{ME}}}\hat{A}_s(\xi), \tag{2.39a}$$

$$\hat{A}_j^f(\xi) = \sqrt{\hat{\Pi}_j^{\text{ME}}}\hat{A}_f(\xi) \tag{2.39b}$$

with $\hat{A}_s(\xi)$ and $\hat{A}_f(\xi)$ given by Eqs. (2.24a) and (2.24b), respectively. It is easy to verify that all the elements are positive semidefinite and satisfy $\sum_j[\hat{\Pi}_j(\xi) + \hat{\Pi}_j^f(\xi)] = \hat{I}$.

As seen in Eqs. (2.21b) and (2.22b), the failure states $|\tilde{\beta}_j\rangle$—and thus the information they carry—do not depend on the separation parameter ξ (or equivalently, on the inconclusive rate Q), but only on the form of the input states. The maximum average probability of correctly identifying them will be given by

$$\begin{aligned} p_c^{\tilde{\beta}} &= \frac{1}{N}\sum_{j=0}^{N-1}\langle\tilde{\beta}_j|\hat{\Pi}_j^{\text{ME}}|\tilde{\beta}_j\rangle \\ &= \frac{1}{N}\left(\sum_{k\in\mathcal{I}}\sqrt{\frac{a_k^2 - a_{\text{min}}^2}{Q^{\text{MC}}}}\right)^2, \end{aligned} \tag{2.40}$$

---

[9] Strictly speaking, referring to this strategy as “concatenated FRIO” constitutes a slight abuse of language, since it does not produce inconclusive outcomes. However, we adopt this terminology throughout the thesis to distinguish it from “standard FRIO” and also because it effectively conveys the idea that the main strategy (optimal FRIO) is applied first; if it fails, a second strategy (ME) is then used to extract the remaining information.

and satisfies $p_c^{\tilde{\beta}} \in [1/N, (n-\mu)/N]$. The lower bound is achieved when $n - \mu = 1$, in which case we can do nothing but make a random guess; the upper bound is attained when the failure states are uniform, which occurs when $a_k^2 = (1-\mu a_{\text{min}}^2)/(n-\mu)$ for all $a_k > a_{\text{min}}$.

To compare the performance of the standard and concatenated FRIO measurements, we consider the overall probability of correct identification provided by each strategy as a function of the inconclusive rate, denoted by $P_{\text{std}}(Q)$ and $P_{\text{cct}}(Q)$, respectively. This figure of merit encompasses both successful and failure events in the separation process and is given for each case by

$$P_{\text{std}}(Q) = (1-Q)p_c^{\beta}(Q) + \frac{Q}{N}, \tag{2.41a}$$

$$P_{\text{cct}}(Q) = (1-Q)p_c^{\beta}(Q) + Qp_c^{\tilde{\beta}}, \tag{2.41b}$$

where $p_c^{\beta}(Q) = 1 - p_e^{\beta}(Q)$ [see Eqs. (2.33) and (2.34)], and $1/N$ corresponds to the probability of a correct outcome from a random guess, which is the best that can be achieved when no measurement is performed on the failure states. Since $p_c^{\tilde{\beta}} \geq 1/N$, it follows that $P_{\text{cct}}(Q) \geq P_{\text{std}}(Q)$, showing the advantage of the concatenated measurement when information is available after failure (i.e., when $n - \mu > 1$).

We now illustrate these results by considering the discrimination of $N = 3$ symmetric qutrit states. Let the coefficients $\{a_k\}_{k=0}^{2}$ of the input states be specified using spherical coordinates as $\{\cos\gamma, \sin\gamma\cos\phi, \sin\gamma\sin\phi\}$. First, we choose $\gamma = \pi/5$ and $\phi = \pi/10$, which results in $a_0 > a_1 > a_2$. In this case, the failure space is two-dimensional and contains information about the inputs. To see this, in the upper left panel of Fig. 11 we plot the magnitudes of the overlaps

$$|\langle\alpha_i|\tilde{\beta}_j\rangle| = \left|\sum_{\ell=0}^{2} \omega^{\ell(j-i)} a_\ell \tilde{b}_\ell\right| \equiv M_{ij}. \tag{2.42}$$

as a 3D bar chart. Since $M_{ii} > M_{ij}$ for $i \neq j$, the failure state $|\tilde{\beta}_i\rangle$ is most likely to correspond to the input state $|\alpha_i\rangle$. The concatenated measurement exploits this to extract the available information. In the upper right panel, we plot P_{std} and P_{cct} as functions of Q [Eqs. (2.41)], where it is clear that the concatenated FRIO outperforms its standard counterpart for all $Q > 0$.

As a second example, we consider qutrit states with $\gamma = \pi/10$ and $\phi = \pi/4$, which results in $a_0 > a_1 = a_2$. In this case, the failure space is one-dimensional and does not contain information about the inputs. In the lower left panel of Fig. 11, we plot M_{ij} [Eq. (2.42)]. Since M_{ij} is constant for all i, j, the failure states cannot be preferentially associated with any particular input state. Consequently, the standard and concatenated FRIO measurements yield the same overall probabilities of correct identification, as shown in the lower right panel.

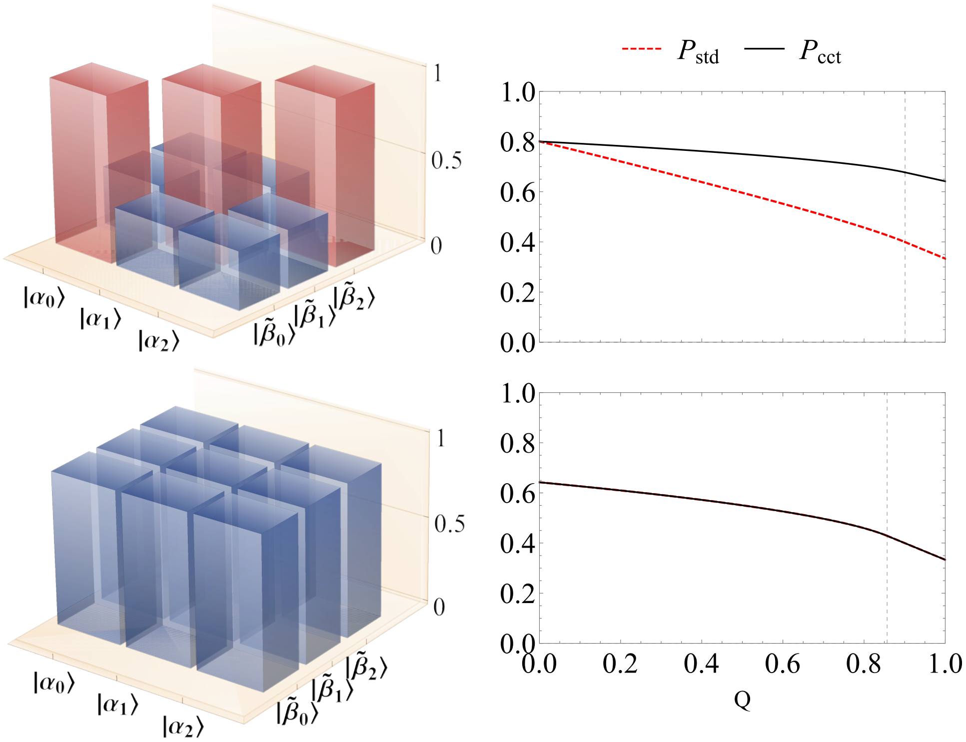

Figure 11 – First column: Overlap magnitudes M_{ij} [Eq. (2.42)]. Second column: Overall probabilities of correct identification vs Q for standard and concatenated FRIO measurements [Eqs. (2.41)]; the vertical dashed line corresponds to the critical inconclusive rate $Q = Q^{\text{MC}}$. First row: The failure states are most likely to correspond to the input states with the same index; when they are discriminated, the concatenated FRIO outperforms the standard one. Second row: There is no preferential correspondence between the failure and input states, and the concatenated and standard schemes yield the same results.

2.6 Summary

In this chapter, we have discussed the discrimination of equiprobable symmetric pure states by revisiting known results for ME and optimal MC measurements, and by deriving the solution for the optimal FRIO measurement. For the latter, we showed that optimal FRIO can be decomposed into a state separation stage that probabilistically modifies the distinguishability of the inputs, yielding successful (more distinguishable) and failure (less distinguishable) outputs, followed by a ME measurement on the former. With this approach, we provided a physical implementation of the strategy and obtained its optimized figure of merit, $P_e^{\min}(Q)$. Moreover, we showed that concatenating optimal FRIO and ME measurements can increase the overall probability of correct identification in high-dimensional spaces. In the subsequent chapters, we will build on these results to experimentally implement the optimal FRIO for qubits, analyze the quantum resources required to implement both the standard and concatenated measurements, and employ these strategies to derive wave-particle duality relations in multipath interferometers.

3 Optical implementation of FRIO measurement for qubit states

"Quantum phenomena do not occur in a Hilbert space. They occur in a laboratory"

Asher Peres

Among the results from the previous chapter, we found a closed-form solution for the optimal FRIO measurement applied to discriminate N equally likely symmetric states of a qubit. In this chapter, we present an experimental realization of this measurement strategy for $N = 2, 3, 5$, and 7 states of a qubit encoded in photonic path modes. Following the theoretical description provided in Sec. 2.4.2, our implementation is divided into two steps: First, using a programmable spatial light modulator, we carry out an optimal quantum state separation; then, the successfully transformed output states are discriminated via ME measurement. This approach is corroborated by the experimental results obtained, where the minimum error rates are achieved for fixed rates of inconclusive outcomes, encompassing the extreme strategies as particular cases. The results presented here were published in [34].

3.1 Experiment

The experimental setup to demonstrate the optimal FRIO measurement is illustrated in Fig. 12(a). Next, we describe each section of our optical implementation, namely, state preparation, separation and discrimination. It is important to stress that, like most optical tests of quantum state discrimination [25–31, 41], our implementation explores the isomorphism between the state of an optical field generated by a laser source and a quantum state, as explained below.[1]

3.1.1 Source and state preparation

Our light source consisted of a 687nm single-mode diode laser. The beam is initially sent through a spatial filter that cleans, expands and collimates its spatial profile, generating an approximate plane wave field. Then, it passes through a half-wave plate (HWP) followed by a polarizer: the former acts as a variable attenuator and the latter provides a clean vertical polarization for the field.

---

[1] As discussed in previous works of our group [30, 41], our implementation could be made truly quantum only by replacing the laser source by a single photon source and the cameras by detector arrays with single photon counting capability.

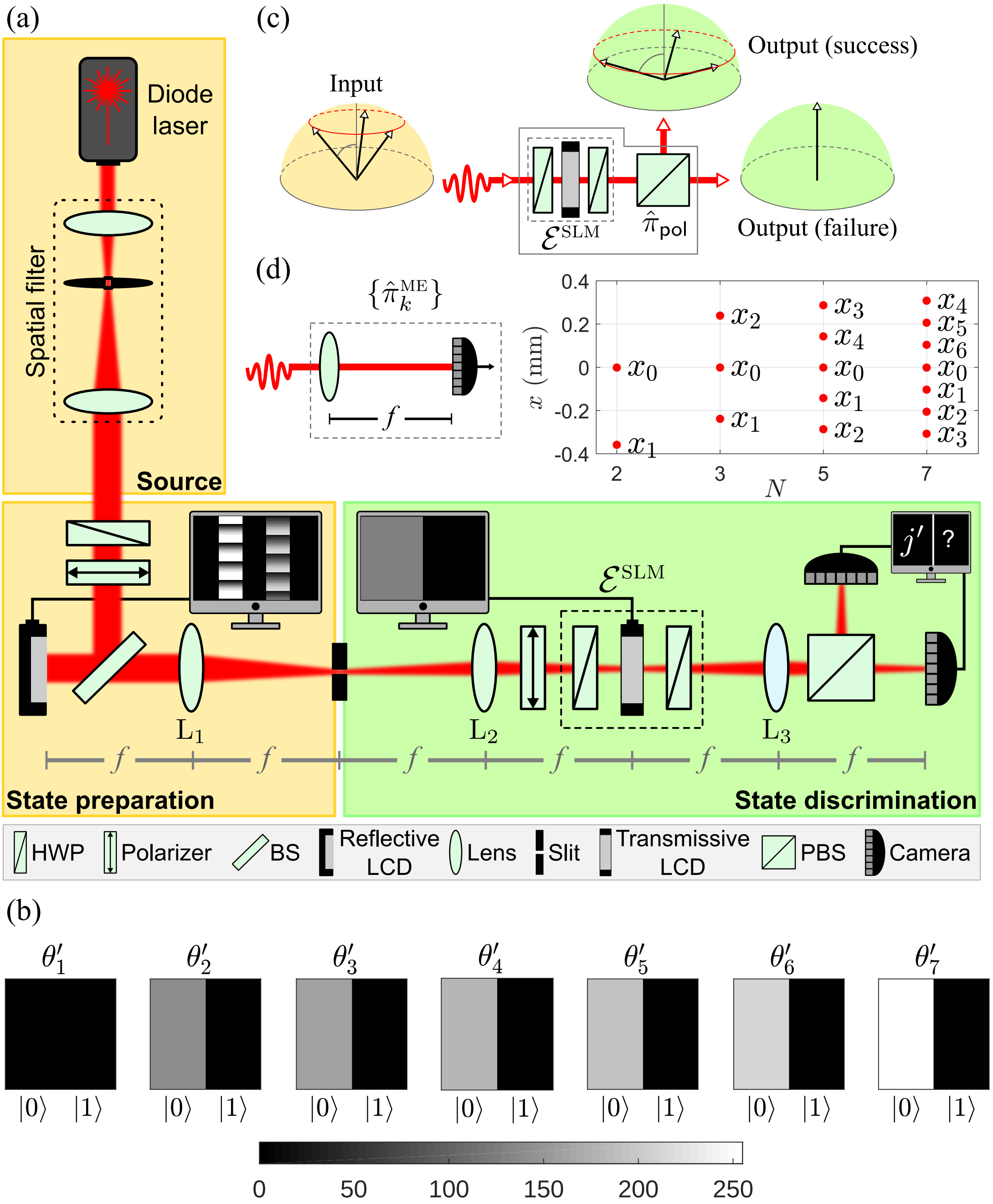

Figure 12 – (a) Experimental setup (see text for details). HWP: half-wave plate; BS: beam splitter; LCD: liquid crystal display; PBS: polarizing beam splitter; L$_1$–L$_3$: spherical lenses with focal length $f = 30\,\mathrm{cm}$. The dashed box highlights the spatial light modulator (SLM) that performs the operation $\mathcal{E}^{\mathrm{SLM}}$ described in the text. (b) Computer-generated masks addressed to the transmissive LCD to assist the state separation $|\alpha_j(\theta)\rangle \rightarrow |\beta_j(\theta'_t)\rangle$, where $\theta = 19.5°$ and $\{\theta'_t\}_{t=1}^{7}$ are given in Table 1. (c) Arrangement for state separation: the SLM couples the path modes with the polarization, which is then measured in the $\{|\mathrm{h}\rangle, |\mathrm{v}\rangle\}$ by the PBS; the separation succeeds (fails) with the projection onto $|\mathrm{v}\rangle$ ($|\mathrm{h}\rangle$). (d) ME measurement to discriminate N symmetric states of path encoded qubits [see Eq. (3.7)]: an array of N pointlike detectors, at the focal plane of a lens, is distributed along the transverse positions $\{x_k\}_{k=0}^{N-1}$ given by Eq. (3.9); the panel shows these positions in our experiment.

To prepare the desired path-encoded qubit states, we employed the method introduced in Refs. [67, 68], which we summarize next. The incoming beam produced at the source is driven to a normal incidence at a reflective liquid crystal display (LCD, Holoeye PLUTO) working as a programmable phase-only spatial light modulator (SLM). This device is addressed with a computer-generated mask given by an array of two blazed diffraction gratings [a typical mask is shown at the computer screen in the state preparation stage of Fig. 12(a)]. For a display with pixels 8 µm wide, the gratings have period, width and center-to-center separation of 12, 18, and 36 pixels, respectively. The SLM imprints the mask information into the phase profile of the beam; the modulated beam is then transmitted through the spherical lens L_1, and a slit diaphragm at its focal plane filters the first diffraction order. The filtered beam is given by a coherent superposition of two non-overlapping path modes generated by the gratings. These modes, represented by $|0\rangle$ and $|1\rangle$, are modulated by complex coefficients with magnitude and phase defined by the phase depth and lateral displacement of the gratings, respectively. The state of the field emerging from this process is equivalent to a stream of single photons prepared in a given pure state on a two-dimensional space spanned by the two path modes. In particular, we use this method to prepare the symmetric qubit states

$$|\alpha_j(\theta)\rangle = \cos\theta|0\rangle + e^{i\varphi}\omega^j \sin\theta|1\rangle. \tag{3.1}$$

Note that unlike Eq. (2.25), these symmetric states have an additional fixed relative phase, φ. In the state separation stage described below, the SLM will introduce a phase shift φ in the $|0\rangle$ mode. To eliminate its effect, in the preparation stage, we introduce the same phase in the $|1\rangle$ mode, ensuring that it becomes global and thus irrelevant.

3.1.2 State separation

As described in Sec. 2.4.1, state separation is the transformation that maps the inputs $|\alpha_j(\theta)\rangle$ into the more distinguishable outputs $|\beta_j(\theta')\rangle$, defined by Eq. (2.26), with the maximum success probability $P_s(\theta')$ given by Eq. (2.29). Here, it will be performed using the light polarization as an ancilla qubit, with the horizontal and vertical polarization states, $|\mathsf{h}\rangle$ and $|\mathsf{v}\rangle$, chosen as the canonical basis for its Hilbert space $\mathcal{H}_a$.

As both path modes in the preparation stage are vertically polarized, the input state is given by $|\alpha_j(\theta)\rangle|\mathsf{v}\rangle$. Now, consider the following unitary operation acting on the composite Hilbert space $\mathcal{H}\otimes\mathcal{H}_a$:

$$\hat{\mathcal{U}}(\theta') = e^{i\varphi}|0\rangle\langle 0| \otimes \begin{bmatrix} \zeta(\theta') & \tau(\theta') \\ -\tau(\theta') & \zeta(\theta') \end{bmatrix}_a + |1\rangle\langle 1| \otimes \hat{I}_a, \tag{3.2}$$

where $\zeta(\theta') = \tan\theta\cot\theta' = \sqrt{1-\tau^2(\theta')}$ and $\hat{I}_a$ is the identity on the ancilla space. By applying this operation on the input state (3.1) and using Eqs. (2.26) and (2.29), it is straightforward to show that

$$\hat{\mathcal{U}}(\theta')|\alpha_j(\theta)\rangle|\mathsf{v}\rangle = \sqrt{P_s(\theta')}|\beta_j(\theta')\rangle|\mathsf{v}\rangle + \sqrt{P_f(\theta')}|0\rangle|\mathsf{h}\rangle. \tag{3.3}$$

To implement the controlled unitary given by Eq. (3.2), we must have the path-encoded qubit acting as the control for a transformation on the polarization qubit: if the path mode is $|0\rangle$, a phase φ is added and the polarization is rotated as

$$|\mathsf{v}\rangle \to |\mathsf{p}(\theta')\rangle = \sqrt{1-\zeta^2(\theta')}|\mathsf{h}\rangle + \zeta(\theta')|\mathsf{v}\rangle; \tag{3.4}$$

otherwise, it is left unchanged. The transformation on the ancilla, denoted by $\mathcal{E}^{\text{SLM}}$, is performed by a programmable SLM composed of a transmissive LCD (Holoeye LC 2012) sandwiched between two HWPs with fixed orientations, shown in the dashed box of Fig. 12(a) (see Appendix 6 for an overview of the SLM characterization, or Ref. [69] for a complete description). This device modulates the polarization and phase of the incoming light as a function of the gray level ($\mathsf{gl} = 0, \ldots, 255$) displayed onto each pixel of the LCD[2] [70]. Given a vertically polarized input beam, for $\mathsf{gl} = 0$, it acts as an identity operation. On the other hand, for $\mathsf{gl} > 0$, its action imprints a phase shift and approaches the desired polarization rotation[3] (3.4). Now, to make this a controlled operation, each path mode is imaged onto one of the halves of the LCD screen by a $4f$ optical system formed by the lenses L_1 and L_2, as shown in Fig. 12(a) (the polarizer before the SLM is used only to ensure a pure vertical polarization for each mode). The mode $|0\rangle$ ($|1\rangle$) goes through the left (right) half which is addressed with a homogeneous computer-generated mask with $\mathsf{gl} > 0$ ($\mathsf{gl} = 0$) [a typical mask is shown on the corresponding computer screen of Fig. 12(a)]. In this way, the SLM will only act in the path mode $|0\rangle$. The relationship between the gray level at the LCD with the target separation angles and the phase shifts for the input symmetric states are discussed in the Appendix 6. The values of these parameters used in our experiment are specified in Table 1; the corresponding masks to implement the intended transformations are shown in Fig. 12(b).

After the unitary system-ancilla coupling, the protocol is completed with a projective measurement on the ancilla's canonical basis $\{|\mathsf{h}\rangle, |\mathsf{v}\rangle\}$, as shown in Eq. (3.3), performed using a polarizing beam splitter (PBS). The vertically polarized component of the state is reflected by the PBS, resulting in the desired separation with the maximal success probability, while the

---

[2] Each gray level, ranging from 0 to 255, corresponds to an increasing voltage applied to the LCD pixel.

[3] Unwanted effects present in the SLM, such as depolarization, prevents it from working exactly as the required unitary polarization rotation. A full characterization of these effects demands a process tomography of the device, which was beyond the scope of the present work but can be found in the master's dissertation of Erick R. de Carvalho [69].

Table 1 – Starting with a set of N symmetric states characterized by $\theta = 19.5°$ (this choice is explained in Appendix 6), the target separation angles in our experiment are specified in th second column. The third column shows the required gray level at the left half of the LCD screen to implement the intended separation; the fourth column shows the phase shifts introduced by the SLM with the addressed gray level.

t	Separation angle $\{\theta'_t\}$	Gray level $\{\mathsf{gl}_t\}$	Phase shift $\{\varphi_t\}$
1	$19.5°$	0	0
2	$22.6°$	142	0.23π
3	$25.5°$	163	0.32π
4	$29.5°$	180	0.40π
5	$34.2°$	195	0.48π
6	$40.0°$	214	0.56π
7	$45.0°$	255	0.61π

horizontal component is transmitted, resulting in completely indistinguishable failure outputs. This process is illustrated in Fig. 12(c).

3.1.3 Minimum-error measurement

The separated states $\{|\beta_j(\theta')\rangle\}$ from the previous step must now be discriminated with a ME measurement given by the N-outcome POVM of Eq. (2.6). From Naimark's theorem described in Sec. 1.1.3, this POVM on the two-dimensional qubit space can be implemented as a projective measurement on an extended N-dimensional Hilbert space, $\mathcal{H}_N$, which in the present case will be achieved via direct sum. To see this, let $\{|k\rangle\}_{k=0}^{N-1}$ be an orthonormal basis for $\mathcal{H}_N$. By applying the quantum Fourier transform

$$\hat{\mathcal{F}}_N = \frac{1}{\sqrt{N}} \sum_{m,n=0}^{N-1} \omega^{mn} |m\rangle\langle n|, \tag{3.5}$$

we generate a conjugate orthonormal basis that can be written as

$$\begin{aligned} |\mu_k\rangle &= \hat{\mathcal{F}}_N |k\rangle \\ &= \sqrt{\frac{2}{N}} |u_k\rangle + \frac{1}{\sqrt{N}} \sum_{m=2}^{N-1} \omega^{mk} |m\rangle, \end{aligned} \tag{3.6}$$

where $|u_k\rangle$ is given by Eq. (2.7). From Eqs. (2.6) and (2.26), it is straightforward to show that $\langle\beta_j(\theta')|\hat{\Pi}_k^{\mathrm{ME}}|\beta_j(\theta')\rangle = |\langle\mu_k|\beta_j(\theta')\rangle|^2$. Therefore, the projective measurement

$$\hat{\pi}_k^{\mathrm{ME}} = |\mu_k\rangle\langle\mu_k| = \hat{\mathcal{F}}_N |k\rangle\langle k| \hat{\mathcal{F}}_N^{-1} \tag{3.7}$$

in the larger space $\mathcal{H}_N$, implements, in the qubit space $\mathcal{H}$, the POVM of Eq. (2.6) for the required ME discrimination.

Table 2 – Parameters used in our experimental setup. λ: wavelength of the laser; f: focal length of the lens L$_3$, Δ: distance between the modes; Λ: width of the modes.

λ	f	Δ	Λ
687 nm	30 cm	288 µm	144 µm

Here, this projective measurement is performed by an array of N pointlike detectors at the focal plane of a spherical lens, as sketched in Fig. 12(d). The lens performs an optical Fourier transform, and the kth detector in the array, located at the transverse position x_k, postselects the state [30]

$$|\mu(x_k)\rangle = \frac{1}{\sqrt{N}} \sum_{l=0}^{N-1} \omega^{x_k N l \Delta/\lambda f} |l\rangle, \tag{3.8}$$

where Δ is the distance between the centers of the path modes, λ is the light wavelength, and f the lens focal length. Thus, the ME measurement is implemented by distributing the detectors along the transverse positions

$$x_k = -\frac{\lambda f m_k}{N\Delta} \quad \Rightarrow \quad |\mu(x_k)\rangle\langle\mu(x_k)| = \hat{\pi}_k^{\mathrm{ME}}, \tag{3.9}$$

where $k = 0, \ldots, N-1$ and $m_k = k$ if $k \leq N/2$ or $m_k = k - N$, otherwise. The panel in Fig. 12(d) shows these positions for $N = 2, 3, 5$, and 7 symmetric states, obtained with our experimental parameters shown in Table 2.

We use CMOS cameras (Thorlabs DCC1545M) at the focal plane of the lens L$_3$, at both outputs of the PBS, as shown in Fig. 12(a). From each camera, we select N pixels (for a pixel size of 5.2 µm) located at the positions shown in Fig. 12(d). With the detections at the reflected arm, we obtain the error rates in the discrimination of the successfully separated states; with the detection at both arms, we obtain the rate of inconclusive outcomes, as explained next.

3.2 Experimental results

3.2.1 Preliminaries

To carry out the experiment, we first define the number of states to be discriminated, N, and the fixed rate of inconclusive results, $Q(\theta')$, which is determined by the target separation angle θ'_t. For a given N and θ'_t, the input states, given by Eq. (3.1), are prepared with $\theta = 19.5°$ (see Appendix 6) and a relative phase $\varphi = \varphi(\theta'_t) \equiv \varphi_t$ shown in Table 1. The inputs are prepared one at a time, each one with its corresponding mask displayed on the reflective LCD. All are subjected to the same operation by the SLM, defined by a fixed mask addressed to the transmissive LCD, according to θ'_t [see Fig. 12(b)]. Finally, the cameras at both outputs of the PBS (success and

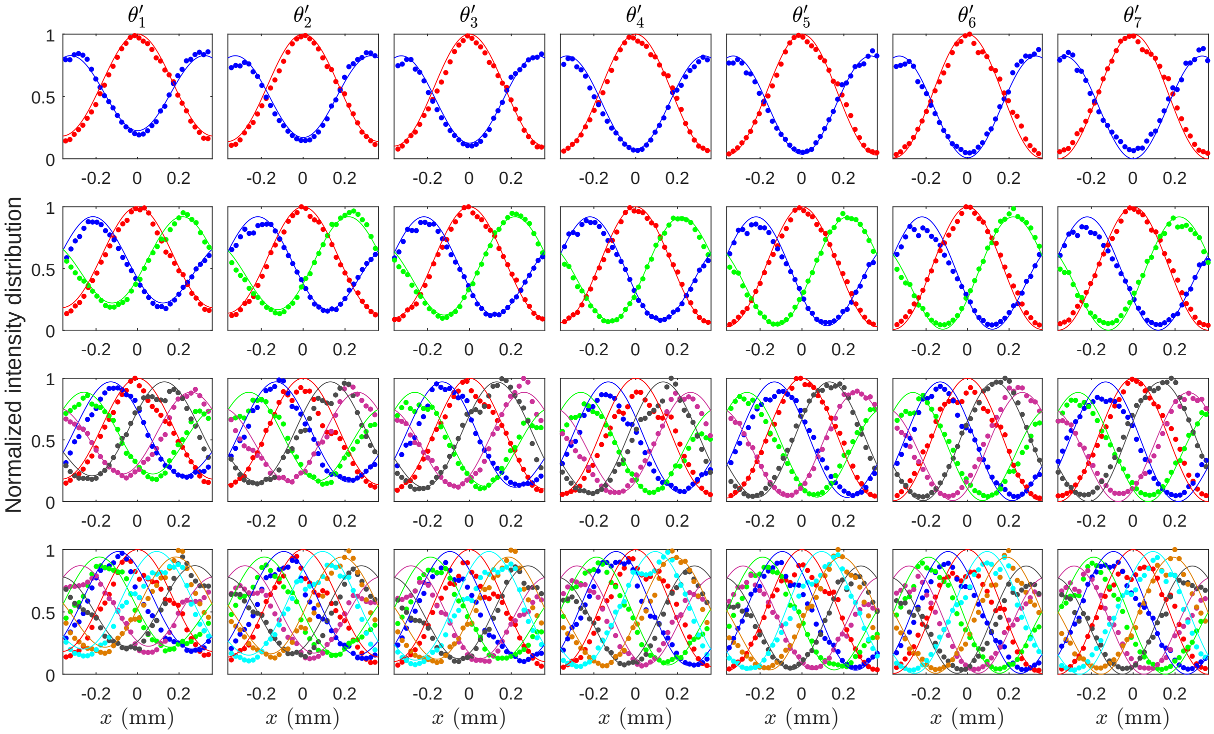

Figure 13 – Successful state separation. Normalized intensity distributions for $I_j^s(x)$: experimental results (dots) and theoretical predictions (solid lines). From top to bottom, each row corresponds to $N = 2, 3, 5,$ and 7 input states; each column corresponds to the target separation angle $\{\theta'_t\}_{t=1}^{7}$ given in Table 1. The colors are associated with the state indices as follows: $j = 0$ (red), $j = 1$ (blue), $j = 2$ (green), $j = 3$ (magenta), $j = 4$ (gray), $j = 5$ (orange), and $j = 6$ (cyan).

failure, $\ell = s, f$) record the intensity distributions, $I_j^\ell(x, y)$, for each input state j. For each distribution, we subtract the background noise and integrate it in the transverse direction y, obtaining $I_j^\ell(x)$. Figures 13 and 14 show the normalized intensity distributions for $I_j^s(x)$ and $I_j^f(x)$, respectively, obtained in our experiments.[4] We first examine their behavior before using them to characterize the state separation and estimate the probabilities in the discrimination process.

For a path-encoded qubit, the probability amplitude of a path mode $|m\rangle$ ($m = 0, 1$) at the focal plane of a lens is written, in position space, as [71]

$$\langle x|m\rangle \propto \exp(-i\kappa(1-2m)x\Delta)\,\mathrm{sinc}(\kappa\Lambda x), \tag{3.10}$$

where $\kappa = \pi/\lambda f$, and Λ is its width. (The values of these parameters in our experiment were provided in Table 2.) Hence, in the case of successful separation, a qubit in the symmetric state

---

[4] For θ'_1 in Fig. 14, there is no separation, and thus no failure state.

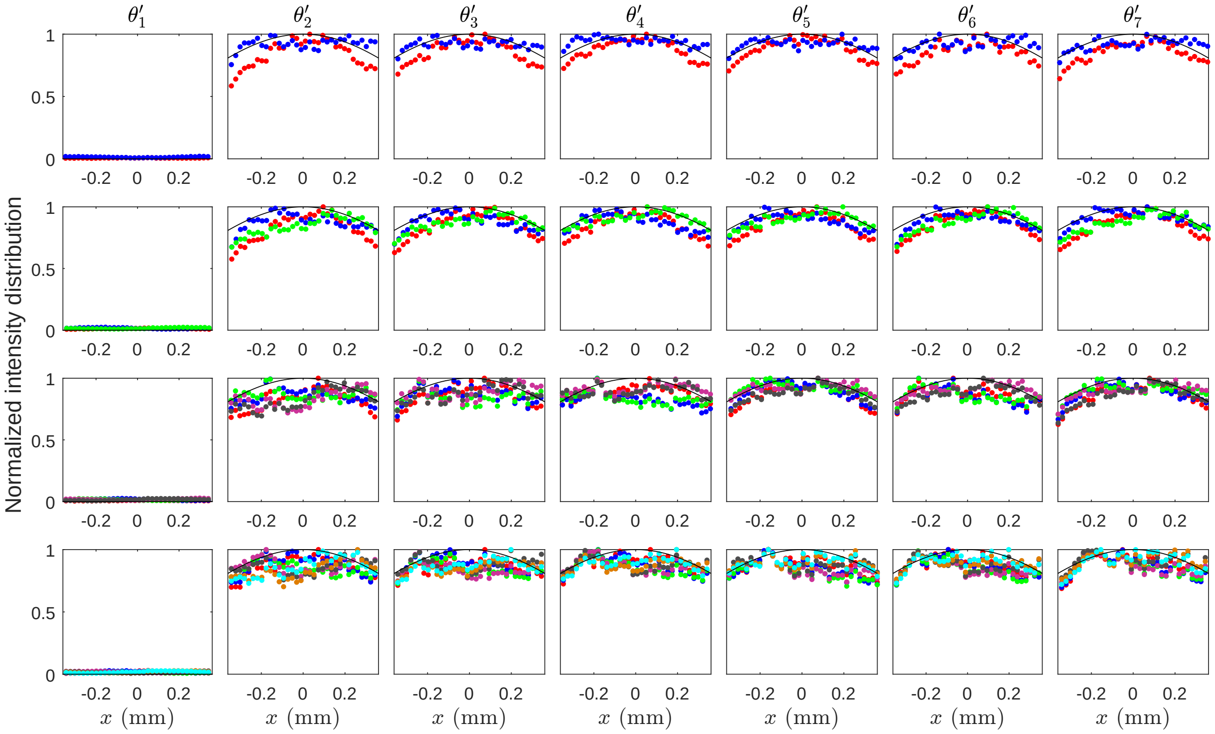

Figure 14 – Failed state separation. Normalized intensity distributions for $I^f_j(x)$: experimental results (dots) and theoretical predictions (solid black lines). From top to bottom, each row corresponds to $N = 2, 3, 5$, and 7 input states; each column corresponds to the target separation angle $\{\theta'_t\}_{t=1}^{7}$ given in Table 1. The colors are associated with the state indices as follows: $j = 0$ (red), $j = 1$ (blue), $j = 2$ (green), $j = 3$ (magenta), $j = 4$ (gray), $j = 5$ (orange), and $j = 6$ (cyan).

$|\beta_j(\theta')\rangle$ defined in Eq. (2.26) will generate a detection probability density given by

$$\begin{aligned} I^s_j(x) &= |\langle x|\beta_j(\theta')\rangle|^2 \\ &\propto \operatorname{sinc}^2(\kappa\Lambda x)\left[1 + V(\theta')\cos(2\kappa x\Delta + \arg\omega^j)\right], \end{aligned} \tag{3.11}$$

where

$$V(\theta') = \sin 2\theta'. \tag{3.12}$$

The expression in Eq. (3.11) represents an interference pattern modulated by the envelope $\operatorname{sinc}^2(\bullet)$; $V(\theta') \in [\sin 2\theta, 1]$ is the visibility of this pattern whose fringes are displaced by $\arg\omega^j = 2\pi j/N$. On the other hand, in the case of failure, where $|\alpha_j(\theta)\rangle \to |0\rangle\ \forall\ j$, the corresponding detection probability density at the focal plane will be

$$I^f_j(x) \propto \operatorname{sinc}^2(\kappa\Lambda x), \tag{3.13}$$

which is simply the diffraction envelope. In Figs. 13 and 14, the solid lines represent the normalized theoretical predictions from Eqs. (3.11) and (3.13), respectively, obtained with the target separation angles $\{\theta'_t\}_{t=1}^{7}$ given in Table 1; they show good agreement with the experimental results (dots).

3.2.2 Characterizing the separated states

From Eq. (3.12), the density matrix associated with the state $|\beta_j(\theta')\rangle$ can be written as

$$|\beta_j(\theta')\rangle\langle\beta_j(\theta')| = \frac{1}{2}\begin{bmatrix} 2\cos^2\theta' & \omega^{-j}V(\theta') \\ \omega^{j}V(\theta') & 2\sin^2\theta' \end{bmatrix}. \tag{3.14}$$

Therefore, by measuring the interference pattern $I_j^s(x)$ and determining its visibility and phase shift, we obtain the off-diagonal terms of the density matrix; the terms on the diagonal are obtained by measuring the amplitudes of the path modes.

The separation angle, θ', sets the parallel of radius $V(\theta')$ on the Bloch sphere, and the azimuthal angle $\arg\omega^j = 2\pi j/N$ locates $|\beta_j(\theta')\rangle$ on this parallel, as seen in Fig. 8(b). For a given θ' and an azimuthal angle ϕ_j, a path-encoded qubit state $\hat{\rho}_j(\theta')$ inside the parallel is mixed and its radial location is defined by the visibility of its interference pattern, $V_j \in [0, \sin 2\theta')$. This state can be written as

$$\hat{\rho}_j(\theta') = \frac{1}{2}\begin{bmatrix} 2\cos^2\theta' & e^{-i\phi_j}V_j \\ e^{i\phi_j}V_j & 2\sin^2\theta' \end{bmatrix}. \tag{3.15}$$

Thus, by replacing the desired θ' and the corresponding measured parameters ϕ_j and V_j in Eq. (3.15), we obtain the location of $\hat{\rho}_j(\theta')$ in the plane containing the parallel, which can be compared with the location of the ideal separated state $|\beta_j(\theta')\rangle$.

Each successfully separated state is characterized using the intensity distribution $I_j^s(x)$ as follows. For a given N and a target separation angle θ'_t, we apply a least-squares fitting to each measured $I_j^s(x)$ using the function

$$F_j(x) = I_j^{\max}\mathrm{sinc}^2(\kappa\Lambda x)\left[1 + V_j\cos(2\kappa x\Delta + \phi'_j)\right], \tag{3.16}$$

where $I_j^{\max}$ is a global proportionality constant for each distribution, V_j is the visibility, and ϕ'_j a phase shift. These are the parameters we obtain from the fitting. The visibility gives us the magnitude of the off-diagonal terms in Eq. (3.15). From the parameters $\{\phi'_j\}_{j=0}^{N-1}$, we compute a correction term

$$\phi_{\text{corr}} = \frac{\pi(N-1)}{N} - \frac{1}{N}\sum_{l=0}^{N-1}\phi'_l, \tag{3.17}$$

from which we obtain the phases of the off-diagonal terms in Eq. (3.15) as

$$\phi_j = \phi'_j + \phi_{\text{corr}}. \tag{3.18}$$

Figure 15 shows the results obtained from this analysis for $N = 2, 3, 5,$ and 7 symmetric states, and the separation angles $\{\theta'_t\}_{t=1}^{7}$ given in Table 1, arranged in the rows and columns, respectively. The black circles represent the parallels of the Bloch sphere set by θ'_t. The colored straight lines

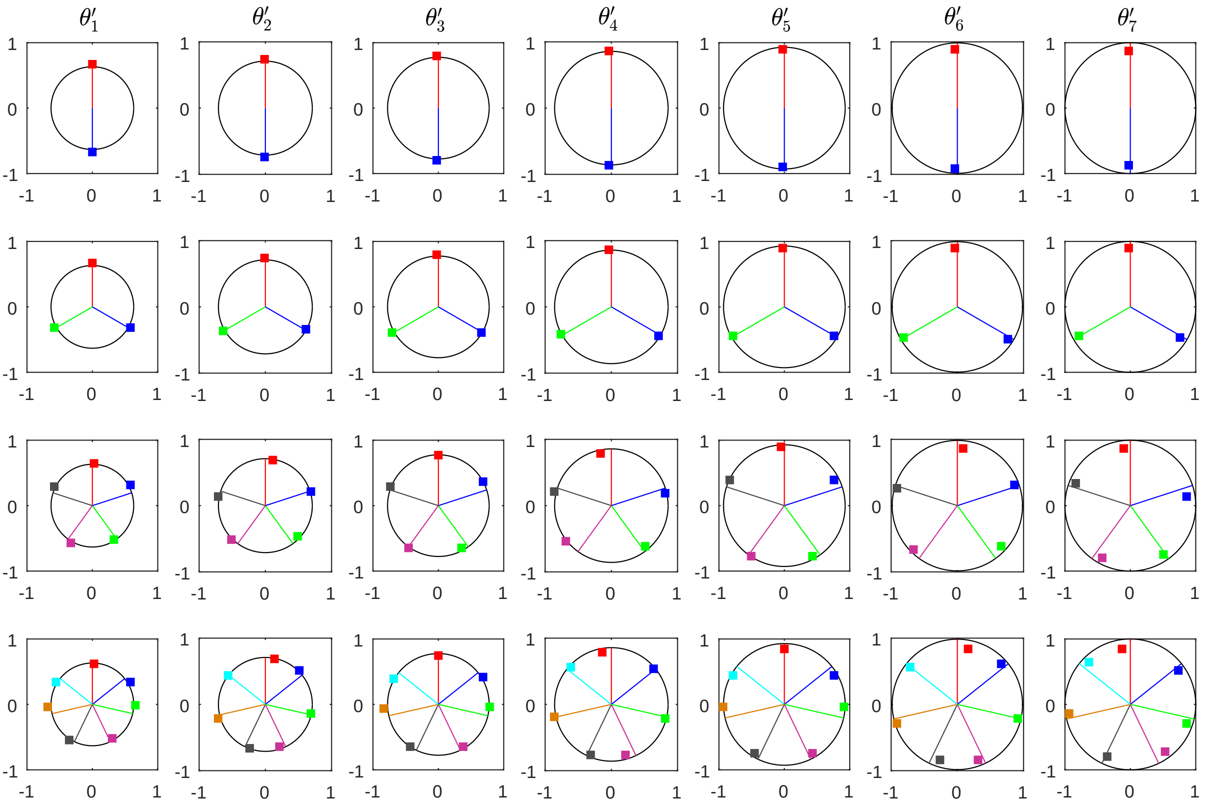

Figure 15 – Characterization of the state separation process for $N = 2, 3, 5$, and 7 symmetric states (rows) with the target separation angles $\{\theta'_t\}_{t=1}^{7}$ (columns) given in Table 1. The black circles represent the parallels of the Bloch sphere of radius $\sin 2\theta'_t$. The colored straight lines represent the target output symmetric states, where $|\beta_0(\theta'_t)\rangle$ is the red line (positive y-axis) and $\{|\beta_j(\theta'_t)\rangle\}_{j=1}^{N-1}$ are the remaining lines along the clockwise direction. The separated states, characterized experimentally, are shown as squares with the same colors of the target states.

locate the target output symmetric states, where $|\beta_0(\theta'_t)\rangle$ is the red line (positive y-axis) and $\{|\beta_j(\theta'_t)\rangle\}_{j=1}^{N-1}$ are the remaining lines along the clockwise direction. The states $\hat{\rho}_j(\theta'_t)$ are shown as square markers with the same colors of the target states.

Regarding the azimuthal angles $2\pi j/N$ that characterize the symmetric states, there is an excellent agreement between theory and experiment for $N = 2$ and 3. This agreement gets a little worse for $N = 5$ and 7, although it is still good. As N increases, the adjacent states of a parallel become closer, which means that their relative phases are also closer and thus more susceptible to errors due to the finite phase resolution of the LCDs in both the preparation and separation stages. The radial location of $\hat{\rho}_j(\theta'_t)$ is determined by the measured visibility V_j. For a given θ'_t, a visibility $V_j < \sin 2\theta'_t$ indicates loss of purity of the path-encoded states. In our experiment, this is observed more significantly for θ'_6 and, especially, θ'_7, as seen in Fig. 13. The main cause for this is the depolarization of the ancilla induced by the transmissive LCD (see Appendix 6), which is more detrimental for the gray levels associated with these separation angles. As an effect, the error rate in the discrimination increases since the ME measurement relies on the interference of the path modes.[5] On the other hand, in a few cases we also obtained a slight deviation $V_j > \sin 2\theta'_t$ (e.g., $N = 2$ and θ'_1 in Fig. 13), which we attribute to inaccuracies in the preparation of the input states.[6] In this case, the consequence is the decreasing of the expected error rate.

Despite experimental imperfections, the state separation increased the distinguishability of the input states in all instances $\theta = \theta'_1 \to \theta'_t$ for $t = 2, \ldots, 7$. The gradual increase in distinguishability, accounted for by the measured visibilities, was also observed from one step to another, i.e., $\theta'_t \to \theta'_{t+1}$, with the exception of $\theta'_6 \to \theta'_7$, for which there is a slight decrease in visibilities, due to the reasons discussed above.

3.2.3 The probabilities in FRIO discrimination

The experimental success probability in the state separation, $[p_s]_{\text{expt}}$, is obtained from the intensity distributions in both PBS outputs. First, we integrate them over x, $I_j^\ell = \sum_x I_j^\ell(x)$, and then, for each input j, we compute

$$p_{sj} = \frac{I_j^s}{(I_j^s + I_j^f)}. \tag{3.19}$$

Finally, we average this over all the inputs, obtaining

$$[p_s]_{\text{expt}} = \frac{1}{N} \sum_{j=0}^{N-1} p_{sj}. \tag{3.20}$$

Figure 16 shows the success probability as a function of the separation angles for each N. There is a good agreement between the experimental results (black squares) and the optimal theoretical expectations (black curves) given by Eq. (2.29).

The experimental probabilities of correctly identifying the separated states, $[p_c^\beta]_{\text{expt}}$, are computed from the intensity distributions $I_j^s(x)$ shown in Fig. 13 as follows. First, we use the phase correction term, ϕ_{corr}, given by Eq. (3.17), to determine offsets that correct the x-axis as

$$x_{\text{corr}} = x - \frac{\phi_{\text{corr}}}{2\kappa\Delta}. \tag{3.21}$$

This ensures greater accuracy in locating the single-pixel detectors that will implement the ME measurement.[7] For a given input state j, we collect the intensities at the N pixels along the x_{corr}-axis located at the positions given by Eq. (3.9) and apply a small compensation for the

---

[5] Note that the error probability in Eq. (2.37) can be written as $1 - (1 + V_j)/N$.

[6] As $\theta'_1 = \theta$, the SLM does not change the ancilla state for a zero gray level.

[7] The experimental intensity distributions in Figs. 13 and 14 are plotted using x_{corr}.

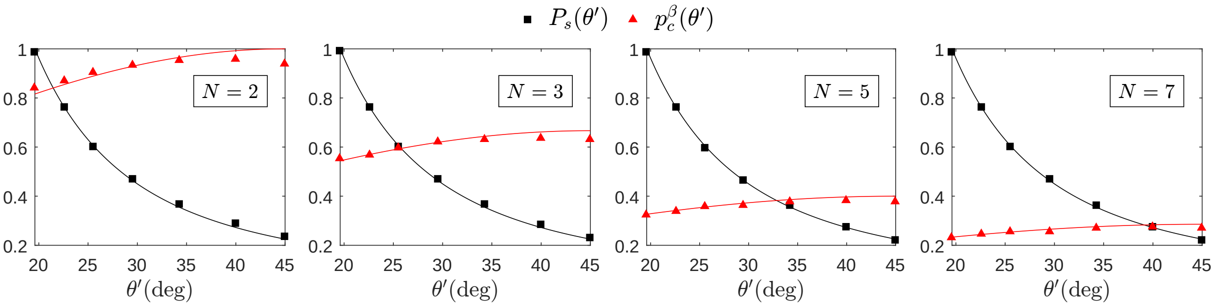

Figure 16 – Experimental results: average probabilities of successful state separation (black squares) and correct discrimination of the separated states (red triangles). The solid curves correspond to the optimal theoretical expectations $P_s(\theta')$ and $p_c^\beta(\theta') = 1 - p_e^\beta(\theta')$, given by Eqs. (2.29) and (2.37), respectively. The insets show the number of states, N. In both cases, the standard deviations are of the order of 10^{-3}. Thus, the error bars were smaller than the size of the data points and were not shown.

detection efficiency due to diffraction, yielding[8] $\{\mathcal{I}_j^s(x_k)\}_{k=0}^{N-1}$. From these intensities, we obtain

$$p_{jk} = \frac{\mathcal{I}_j^s(x_k)}{\sum_{l=0}^{N-1} \mathcal{I}_j^s(x_l)}, \tag{3.22}$$

namely, the conditional probabilities of correct ($j = k$) or erroneous ($j \neq k$) identifications of the separated states. Finally, the experimental average rate of correct discrimination will be given by

$$[p_c^\beta]_{\text{expt}} = \frac{1}{N}\sum_{j=0}^{N-1} p_{jj}. \tag{3.23}$$

These results are shown in Fig. 16 (red triangles) as a function of the separation angles for each N; the red curves correspond to the optimal theoretical predictions, $p_c^\beta(\theta') = 1 - p_e^\beta(\theta')$, given by Eq. (2.37). In general, there is good agreement between theory and experiment; the observed discrepancies are mainly due to the issues pointed out in the state separation stage, as discussed in the previous subsection. Despite these, it is clear that the rate of correct results for the separated states increases with θ', reflecting the increase in their distinguishability.

From these data, we can calculate the FRIO figure of merit using Eqs. (2.32). The experimental error rates and fixed rates of inconclusive results will be given, respectively, by

$$[P_e]_{\text{expt}} = [p_s]_{\text{expt}}(1 - [p_c^\beta]_{\text{expt}}) \tag{3.24a}$$

$$Q_{\text{expt}} = 1 - [p_s]_{\text{expt}}. \tag{3.24b}$$

In Fig. 17, we plot the former as a function of the latter (markers) for each N indicated in the insets (note that this is an experimental version of Fig. 10). The curves of the same color

---

[8] The compensated intensity is given by $\mathcal{I}_j^s(x_k) = I_j^s(x_k)/\chi_k$, where the compensation factor $\chi_k = \text{sinc}^2(\pi\Lambda x_k/\lambda f)$ depends only on the detector position [30].

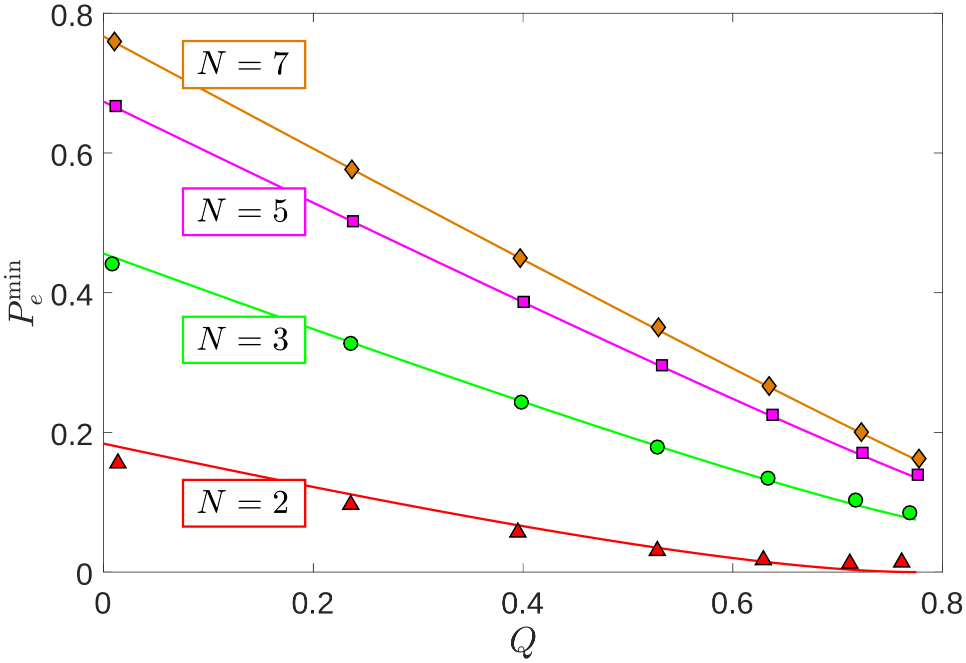

Figure 17 – Average error probability, $P_e^{\min}$, as a function of the fixed rate of inconclusive outcomes, Q. The markers represent the experimental results and the solid curves the optimal theoretical expectations given by Eq. (2.38). The insets show the number of states, N. Again, the error bars were not shown for the same reasons described in Fig. 16.

as the markers correspond to the optimal theoretical prediction, $P_e^{\min}(Q)$, given by Eq. (2.38), and show good agreement with the data. It can be seen that this agreement improves as the number of input states increases. As discussed in Sec. 2.4.2, this occurs because the errors and inconclusive results become predominant in the discrimination process as N increases. In this way, experimental imperfections independent of N become less noticeable. Still, we can see from Fig. 17 that our FRIO measurement scheme for discriminating between N equally likely symmetric states, closely reaches the minimum error rate for a fixed value of Q, and interpolates between the ME discrimination ($Q = 0$) and optimal UD (for $N = 2$) or MC (for $N > 2$) strategies ($Q = 0.7771$).

3.3 Summary and outlook

In this chapter, the optimal FRIO measurement, theoretically described in Sec. 2.4, has been experimentally demonstrated for discriminating between N equiprobable symmetric states of a qubit. Although our experiment was carried out with a classical laser source, the results would not differ if it were done with a true single photon source and a detector array with single photon counting capability, as extensively discussed in previous works [30, 41]. Our implementation employed two path modes of light to encode the symmetric states; the light polarization was used as an ancilla system to perform state separation, which controllably increased the distinguishability between the symmetric states. This transformation was implemented through a programmable spatial modulator, which gave us a fine control for the transition between ME measurement and optimal UD (or MC) measurements.

In addition to show the optimal FRIO measurement for N states of a qubit, rather than only two, our setup has an advantage over a previous FRIO implementation [33] that used polarization-encoded qubits: it can be straightforwardly extended to high-dimensional qudits. We have all the ingredients for that: the qudit states can be encoded in d path modes produced by an array of d blazed diffraction gratings at the SLM [67] [similarly to the two-dimensional case shown in the computer screen of Fig. 12(a)]. In addition, both extreme strategies, ME and UD, have been demonstrated for discriminating between path-encoded symmetric states of qudits [30,41]. The FRIO measurement in this case requires the parametric state separation in the first step, a protocol introduced in Ref. [23]. This protocol also uses a two-dimensional ancilla and can be performed in a similar way to what we did here, using an SLM (the optimal UD [41], in particular, employed this transformation to implement the maximum separation). After that, we just implement the ME measurement on the successfully separated states following the method shown in [30]. Therefore, our encoding enables a single setup where one can implement the most fundamental state discrimination strategies in dimensions much larger than two. The switching between these strategies is controlled just by tuning the transformation carried out by the SLM, which means to change the computer-generated mask addressed to a programmable LCD.

Part II

Fundamental Aspects

4 Coherence in quantum state discrimination

> *"Mathematics, rightly viewed, possesses not only truth, but supreme beauty."*
> *Bertrand Russell*

Quantum coherence is an intrinsic property of quantum states and an essential ingredient for many quantum phenomena. This property has acquired the status of a resource, in the sense that it can be generated, manipulated, and consumed to perform useful tasks. In this chapter, we present a comprehensive study on the role of quantum coherence as a resource for implementing the standard and concatenated FRIO discrimination strategies introduced in Chapter 2. Beyond its fundamental significance, we show how the characterization of this resource has practical applications, particularly in the context of secure quantum communication. The results reported here were published in [72].

4.1 Introduction

In the early 1990s, protocols like dense coding [73] and quantum teleportation [74] showed that quantum entanglement, far beyond an intriguing phenomenon with deep fundamental consequences, could be a valuable resource for practical applications. Since then, many other properties of physical systems, such as quantum discord [75, 76], quantum coherence [77–79], among others [80], have also been recognized as resources, meaning that without them, a given task would be infeasible—just as quantum teleportation is not possible without entanglement. In this context, the implementation of quantum state discrimination, like many other quantum information tasks, is underpinned by quantum resources, and recent efforts have been directed towards understanding and unraveling these resources. Early studies focused on the role of quantum correlations for standard UD of two [81, 82] or more [83, 84] states, ME [85], and FRIO [86] of two states, showing that quantum discord rather entanglement is the required resource for the protocol. Recent studies, on the other hand, have explored the role of quantum coherence in standard UD of two states [87–89], given that it is a more fundamental resource than quantum correlations [90]. While in Refs. [87, 88], the problem was addressed with the standard notion of coherence—based on projective measurements—Ref. [89] adopted a more suitable approach, using the generalized resource theory of coherence developed by Bischof *et al.* [79]. In this framework, coherence is the resource needed to implement a POVM on a given state in an extended Hilbert space, which serves as the operational basis for the discrimination strategies discussed in this thesis.

Here, following the approach of Ref. [89], we investigate coherence based on POVMs as a resource for standard and concatenated FRIO discrimination between N equally probable symmetric states of arbitrary dimension n, where $N \geq n$. For these strategies introduced in Chapter 2, we first show that the POVM coherence in the assisted separation stage decomposes into the coherence of the ancillary state and the quantum discord between the system and the ancilla, evidencing coherence as a more elementary resource than quantum correlations. Next, it is demonstrated that the POVM coherence for standard and concatenated FRIO decomposes into the POVM coherence measures for state separation and ME measurement, weighted by the probabilities of occurrence of each event. Due to the ME discrimination of inconclusive states, the coherence required for the concatenated scheme is shown to be greater than that of the standard one. We discuss other general aspects of our results by characterizing the POVM coherence in the discrimination of qutrit states, with respect to the distinguishability of the inputs and the inconclusive rate. Finally, by exploiting POVM-based coherence as a quantifier of private randomness, we discuss the standard and concatenated FRIO strategies from the perspective of generating random bits that are secret to an eavesdropper—a relevant topic in quantum random number generation [55, 91–94] and quantum cryptography [95].

4.2 Theoretical background

4.2.1 Coherence based on positive operator-valued measures

In general, the framework of a quantum resource theory consists of the following elements [80]: (i) states with and without the resource, namely, the resource states and free states, respectively; (ii) a set of free operations which cannot create a resource state from a free state; and (iii) a suitable measure that quantifies the resource in any given state, which must be non-increasing under free operations. Taking entanglement as the most well-known example of a quantum resource, these elements are: (i) entangled (resource) and separable (free) states; (ii) local operations and classical communication; and (iii) von Neumann entropy, for instance.

Quantum coherence is a basis-dependent concept, so we must first specify a reference basis to describe it. To this end, given an n-dimensional Hilbert space, $\mathcal{H}$, let $\{|k\rangle\}_{k=0}^{n-1}$ be its reference orthonormal basis. In the standard resource theory of coherence [78], the free states are diagonal in this basis, i.e.,

$$\hat{\rho}' = \sum_{k=0}^{n-1} p_k |k\rangle\langle k|, \tag{4.1}$$

and are called *incoherent states*. States that are not diagonal in this basis are, therefore, resource states. The free operations, called incoherent operations, are those that admit a Kraus decomposition with incoherent Kraus operators, i.e., $\mathcal{E}_{\text{inc}}(\hat{\rho}) = \sum_i \hat{A}_i \hat{\rho} \hat{A}_i^\dagger$, where $\hat{A}_i|k\rangle \propto |k'\rangle$. Among the different measures to quantify coherence, the relative entropy of coherence for a state $\hat{\rho}$ is given by

$$C_r(\hat{\rho}) = S(\hat{\rho}') - S(\hat{\rho}), \tag{4.2}$$

where $S(\hat{\varrho}) = -\text{Tr}(\hat{\varrho} \log_2 \hat{\varrho})$ is the von Neumann entropy.

The standard notion of coherence is connected with projective measurements in the following sense: given an arbitrary state $\hat{\rho}$, it can be written in the reference basis as $\hat{\rho} = \sum_{i,j=0}^{n-1} \rho_{ij} |i\rangle\langle j|$. The diagonal part of $\hat{\rho}$, obtained by suppressing its off-diagonal elements, can be written as $\hat{\rho}' = \sum_{k=0}^{n-1} \hat{\pi}_k \hat{\rho} \hat{\pi}_k$, where $\hat{\pi}_k = |k\rangle\langle k|$. This means that incoherent states can be seen as arising from a rank-one projective measurement on $\hat{\rho}$ in the basis $\{|k\rangle\}$, and coherence, quantified by $C_r(\hat{\rho})$, as the resource required to implement such a measurement.

Further studies extended this concept of coherence to general bases, lifting the requirement of orthogonality [96], and measurements described by orthogonal operators of higher rank [97]. But only recently has a proper extension of the resource theory of quantum coherence been achieved for POVMs [79, 93], the most general way of describing a quantum measurement. To summarize it, let $\mathbf{\Pi} = \{\hat{\Pi}_j\}_{j=0}^{N-1}$ be an N-outcome POVM on $\mathcal{H}$. As described in Sec. 1.1.3 (see "Tensor product extension"), its measurement on the state $\hat{\rho}$ may be implemented as a projective measurement $\boldsymbol{\pi} = \{\hat{\pi}_j\}_{j=0}^{N-1}$ on an extended tensor product Hilbert space. In the scenario considered there, the initial system-ancilla state is given by

$$\hat{\rho}_{\mathsf{da}} = \hat{\rho} \otimes |\ell\rangle_{\mathsf{a}}\langle \ell|. \tag{4.3}$$

Using Eq. (1.7), the post-measurement state, before recording the result, is

$$\hat{\rho}'_{\mathsf{da}} = \sum_{j=0}^{N-1} \hat{\pi}_j \hat{\rho}_{\mathsf{da}} \hat{\pi}_j = \hat{V}^\dagger \left(\sum_{j=0}^{N-1} p_j \hat{\rho}_j \otimes |\ell(j)\rangle_{\mathsf{a}}\langle \ell(j)| \right) \hat{V}, \tag{4.4}$$

where $\hat{V}$ is a global unitary operation and $p_j = \text{Tr}(\hat{\pi}_j \hat{\rho}_{\mathsf{da}}) = \text{Tr}(\hat{\Pi}_j \hat{\rho})$. The von Neumann entropies of these states are respectively given by

$$S(\hat{\rho}_{\mathsf{da}}) = S(\hat{\rho}), \tag{4.5a}$$

$$S(\hat{\rho}'_{\mathsf{da}}) = H(\{p_j\}) + \sum_{j=0}^{N-1} p_j S(\hat{\rho}_j), \tag{4.5b}$$

where, in (4.5b), we used the invariance of this entropy under unitaries, and

$$H(\{p_j\}) = -\sum_{j=0}^{N-1} p_j \log_2 p_j \tag{4.6}$$

denotes the Shannon entropy of the probability distribution $\{p_j\}$. Similarly to the standard notion of coherence, quantified by the expression in Eq. (4.2), the relative entropy of POVM-based coherence is given by

$$\begin{aligned}\mathcal{C}_{\text{rel}}(\hat{\rho}, \mathbf{\Pi}) &= S(\hat{\rho}'_{\mathsf{da}}) - S(\hat{\rho}_{\mathsf{da}}) \\ &= H(\{p_j\}) + \sum_{j=0}^{N-1} p_j S(\hat{\rho}_j) - S(\hat{\rho}),\end{aligned} \tag{4.7}$$

and quantifies the amount of quantum coherence consumed to implement the POVM $\mathbf{\Pi}$ on the state $\hat{\rho}$. In this formalism, the incoherent states are block-diagonal,[1] as is the state $\hat{\rho}'_{\mathsf{da}}$ in Eq. (4.4). Note that if $\mathbf{\Pi}$ is a projective measurement, Eq. (4.7) reduces to Eq. (4.2).

4.2.2 Quantifying correlations in a quantum state

Consider the case where identical copies of a bipartite system in the state $\hat{\rho}_{\mathsf{da}} \in \mathcal{B}(\mathcal{H}_{\mathsf{d}} \otimes \mathcal{H}_{\mathsf{a}})$ are shared between two parties. In the many copies scenario, the total amount of correlations is given by the quantum mutual information [98]:

$$I(\hat{\rho}_{\mathsf{da}}) = S(\hat{\rho}_{\mathsf{d}}) + S(\hat{\rho}_{\mathsf{a}}) - S(\hat{\rho}_{\mathsf{da}}), \tag{4.8}$$

where $\hat{\rho}_{\mathsf{d}} = \text{Tr}_{\mathsf{a}}\hat{\rho}_{\mathsf{da}}$ and $\hat{\rho}_{\mathsf{a}} = \text{Tr}_{\mathsf{d}}\hat{\rho}_{\mathsf{da}}$ are the reduced density matrices for each partition. Now, suppose that for each copy a projective measurement $\{\hat{\pi}_i^{\mathsf{a}}\}$ is implemented on subsystem a. The gain of information about d after measuring a is related to the classical correlations from the perspective of the latter subsystem, which are quantified by

$$J(\mathsf{d}|\{\hat{\pi}_i^{\mathsf{a}}\}) = S(\hat{\rho}_{\mathsf{d}}) - \sum_i q_i S(\hat{\rho}^i_{\mathsf{d|a}}), \tag{4.9}$$

where

$$q_i = \text{Tr}[(\hat{I}_{\mathsf{d}} \otimes \hat{\pi}_i^{\mathsf{a}})\hat{\rho}_{\mathsf{da}}(\hat{I}_{\mathsf{d}} \otimes \hat{\pi}_i^{\mathsf{a}})], \tag{4.10a}$$

$$\hat{\rho}^i_{\mathsf{d|a}} = \frac{1}{q_i}\text{Tr}_{\mathsf{a}}[(\hat{I}_{\mathsf{d}} \otimes \hat{\pi}_i^{\mathsf{a}})\hat{\rho}_{\mathsf{da}}(\hat{I}_{\mathsf{d}} \otimes \hat{\pi}_i^{\mathsf{a}})]. \tag{4.10b}$$

The quantum portion of correlations from the perspective of a is measured by the quantum discord, defined as

$$D(\mathsf{d|a}) = I(\hat{\rho}_{\mathsf{da}}) - \max_{\{\hat{\pi}_i^{\mathsf{a}}\}} J(\mathsf{d}|\{\hat{\pi}_i^{\mathsf{a}}\}), \tag{4.11}$$

where the maximization of J is over all rank-one projective measurements on that subsystem.

---

[1] Recall that the projectors given by Eq. (1.7) may have ranks ranging from one to n.

4.3 POVM-based coherence in optimal FRIO discrimination

With the theoretical framework presented above, we are now able to investigate the role of POVM-based coherence in the optimal FRIO discrimination of equiprobable symmetric states, described in Sec. 2.4. To avoid cumbersome equations, in this chapter, we will omit the dependence on the separation parameter ξ for all entities that are functions of it.

4.3.1 POVM coherence in quantum state separation

In the state separation process, let $\hat{\rho}$, $\hat{\rho}_s$, and $\hat{\rho}_f$ denote the density matrices describing the input, successful output, and failed output states, respectively. Using Eqs. (2.2), (2.3), (2.21a), (2.21b), these states will be given by

$$\hat{\rho} = \frac{1}{N}\sum_{j=0}^{N-1} |\alpha_j\rangle\langle\alpha_j| = \sum_{k\in\mathcal{I}} a_k^2 |k\rangle\langle k|, \tag{4.12a}$$

$$\hat{\rho}_s = \frac{1}{N}\sum_{j=0}^{N-1} |\beta_j\rangle\langle\beta_j| = \sum_{k\in\mathcal{I}} b_k^2 |k\rangle\langle k|, \tag{4.12b}$$

$$\hat{\rho}_f = \frac{1}{N}\sum_{j=0}^{N-1} |\tilde{\beta}_j\rangle\langle\tilde{\beta}_j| = \sum_{k\in\mathcal{I}} \tilde{b}_k^2 |k\rangle\langle k|, \tag{4.12c}$$

where $\mathcal{I} = \{k | a_k \neq 0\}$, with $|\mathcal{I}| = n \leq N$. Thus, denoting the global system-ancilla state after the unitary coupling (2.20) as $\hat{\rho}_{\mathsf{da}}$, we have

$$\begin{aligned}\hat{\rho}_{\mathsf{da}} &= \hat{\mathcal{U}}\left(\hat{\rho}\otimes|1\rangle_{\mathsf{a}}\langle 1|\right)\hat{\mathcal{U}}^\dagger \\ &= P_s\hat{\rho}_s\otimes|1\rangle_{\mathsf{a}}\langle 1| + Q\hat{\rho}_f\otimes|0\rangle_{\mathsf{a}}\langle 0| + \sqrt{P_sQ}\sum_{k\in\mathcal{I}} b_k\tilde{b}_k|k\rangle\langle k|\otimes\hat{\sigma}_x^{\mathsf{a}},\end{aligned} \tag{4.13}$$

where $\hat{\sigma}_x^{\mathsf{a}} = |1\rangle_{\mathsf{a}}\langle 0| + |0\rangle_{\mathsf{a}}\langle 1|$. It can be shown that the reduced state of the system is preserved, i.e.,

$$\hat{\rho}_{\mathsf{d}} = \mathrm{Tr}_{\mathsf{a}}\hat{\rho}_{\mathsf{da}} = P_s\hat{\rho}_s + Q\hat{\rho}_f = \hat{\rho}, \tag{4.14}$$

while the ancilla state $\hat{\rho}_{\mathsf{a}} = \mathrm{Tr}_{\mathsf{d}}\hat{\rho}_{\mathsf{da}}$ is transformed into

$$\hat{\rho}_{\mathsf{a}} = P_s|1\rangle_{\mathsf{a}}\langle 1| + Q|0\rangle_{\mathsf{a}}\langle 0| + \sqrt{P_sQ}\sum_{k\in\mathcal{I}} b_k\tilde{b}_k\hat{\sigma}_x^{\mathsf{a}}. \tag{4.15}$$

Note that coherence, in the sense of its standard resource theory [78], is produced only in the ancilla state. It can be easily quantified by the relative entropy of coherence given by Eq. (4.2), which in the basis $\{|0\rangle_{\mathsf{a}}, |1\rangle_{\mathsf{a}}\}$ yields

$$C_r(\hat{\rho}_{\mathsf{a}}) = H_2(P_s) - S(\hat{\rho}_{\mathsf{a}}), \tag{4.16}$$

where

$$H_2(x) = -x\log_2 x - (1-x)\log_2(1-x) \tag{4.17}$$

is the binary entropy and $S(\hat{\rho}_{\mathsf{a}}) = -\sum_{j=\pm} \lambda_j \log_2 \lambda_j$, with

$$\lambda_\pm = \frac{1}{2}\left\{1 \pm \sqrt{1 - 4P_sQ\left[1 - \left(\sum_{k\in\mathcal{I}} b_k\tilde{b}_k\right)^2\right]}\right\} \tag{4.18}$$

denoting the eigenvalues of $\hat{\rho}_{\mathsf{a}}$.

The coherence resource required to implement the POVM for state separation, $\mathbf{\Pi}_{\text{SEP}}$, on the input state $\hat{\rho}$ is not fully described by the coherence produced in the auxiliary system given by Eq. (4.16). To see this, we first compute the POVM coherence using Eq. (4.7), obtaining

$$\mathcal{C}_{\text{rel}}(\hat{\rho}, \mathbf{\Pi}_{\text{SEP}}) = H_2(P_s) + P_sS(\hat{\rho}_s) + QS(\hat{\rho}_f) - S(\hat{\rho}), \tag{4.19}$$

where, from Eqs. (4.12), the von Neumann entropies will be simply given by the Shannon entropies $H(\{x_k^2\})$, with $x = a, b, \tilde{b}$. Now, we address the correlations involved in the process. From Eq. (4.13) and the invariance of entropy under unitary transformations, we have $S(\hat{\rho}_{\mathsf{da}}) = S(\hat{\rho})$. In addition, Eq. (4.14) implies that $S(\hat{\rho}_{\mathsf{d}}) = S(\hat{\rho})$. As a result, the quantum mutual information between the system and ancilla [see Eq. (5.14)] will be

$$I(\hat{\rho}_{\mathsf{da}}) = S(\hat{\rho}_{\mathsf{a}}), \tag{4.20}$$

showing that the “cost” of generating correlations is the loss of purity in the ancilla. As demonstrated in Refs. [85, 86], the classical portion of such correlations from the perspective of the ancilla is maximized by the projective measurement in the basis[2] $\{|0\rangle_{\mathsf{a}}, |1\rangle_{\mathsf{a}}\}$; thus, from Eq. (4.9) we have

$$\max J(\mathsf{d}|\{\hat{\pi}_i^{\mathsf{a}}\}) = S(\hat{\rho}) - P_sS(\hat{\rho}_s) - QS(\hat{\rho}_f). \tag{4.21}$$

Finally, using the definition of quantum discord [Eq. (4.11)] and Eqs. (4.16)–(4.21), we can rewrite the POVM coherence (4.19) as

$$\mathcal{C}_{\text{rel}}(\hat{\rho}, \mathbf{\Pi}_{\text{SEP}}) = C_r(\hat{\rho}_{\mathsf{a}}) + D(\mathsf{d}|\mathsf{a}). \tag{4.22}$$

Therefore, the required coherence for implementing the optimal POVM for state separation is built both from the generated coherence in the ancilla and the quantum correlations between system and ancilla.

---

[2] This has been demonstrated in two ways. First, by minimizing the second term on the right-hand side of Eq. (4.9) with respect to the measurement basis $\{\hat{\pi}_{\mathsf{a}}\}$, which maximizes J (Section 4.1 of Ref. [85]). Second, by treating the discrimination process as a communication protocol between Alice and Bob, where their joint state is purified, i.e., $\hat{\rho}_{AB} \to |\psi\rangle_{ABC}$. It is then shown that the accessible information, $\max J = S(\hat{\rho}_A) - E_f(\hat{\rho}_{AC})$, is obtained when Bob measures in the basis $\{|0\rangle_{\mathsf{a}}, |1\rangle_{\mathsf{a}}\}$, where $E_f(\hat{\rho}_{AC})$ is the entanglement of formation between subsystems A and C (Section 4 of Ref. [86]).

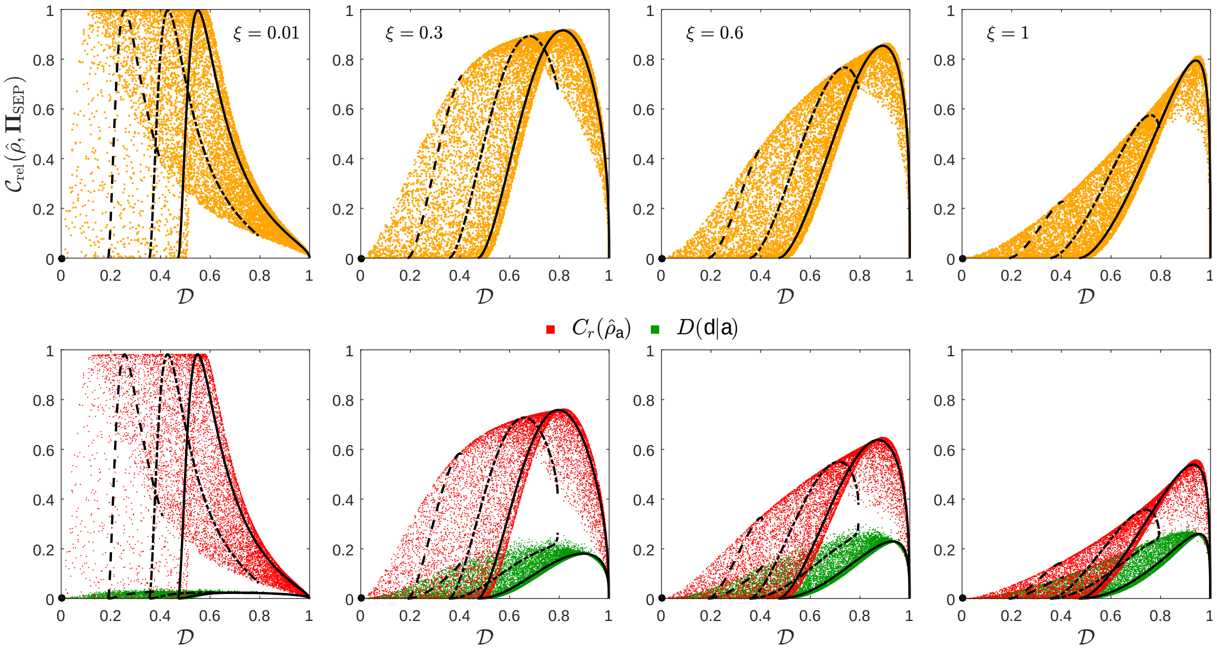

Figure 18 – POVM coherence (orange dots), ancilla's coherence (red dots), and quantum discord (green dots) vs distinguishability in the optimal state separation of $N = 3$ symmetric states of a qutrit. These quantities were computed for 10^4 random input states and a fixed value of the separation parameter ξ shown in the insets. We also plot them for inputs in the range $a_{\rm min} \in [0, a_0]$ [see Eq. (4.24)], where $a_0 = 0$ (circle), $a_0 = 0.192$ (dashed lines), $a_0 = 0.385$ (dash-dotted lines), and $a_0 = 1/\sqrt{3}$ (solid lines).

Example: Separating N symmetric states of a qutrit

To discuss general aspects of the above result, let us take as an example the separation between N symmetric states of a qutrit ($n = 3$). We study the coherence in the process as a function of the distinguishability of the input states $\{|\alpha_j\rangle\}$, which can be quantified by [99]

$$\mathcal{D} = \frac{n}{n-1}\left(P_c - \frac{1}{N}\right), \tag{4.23}$$

where P_c is the average probability of correctly identifying them through the ME measurement given by Eq. (2.8) ($P_c = 1 - P_e$). This measure is bounded by $0 \leq \mathcal{D} \leq n/N$, where the lower and upper bounds are attained by parallel and maximally distinguishable input states, respectively.[3]

Considering $N = 3$, we generate 10^4 random input states $\hat\rho$ [see Eq. (4.12a)], and from each state we compute the three terms of Eq. (4.22) for a fixed value of the separation parameter ξ. The results obtained as a function of $\mathcal{D}$ are shown in Fig. 18: in the top row, we plot the POVM coherence for state separation (orange dots), and in the bottom row its components $C_r(\hat\rho_{\rm a})$ (red

---

[3] In the next chapter, the concept of distinguishability will reappear in the discussion of wave-particle duality. In this context, it is important to emphasize that, although the measure in (4.23), based on the ME measurement, imposes an ordering on sets of symmetric states, it does not effectively represent the usual notion of distinguishability that will be discussed there (see Sec. 5.3.2).

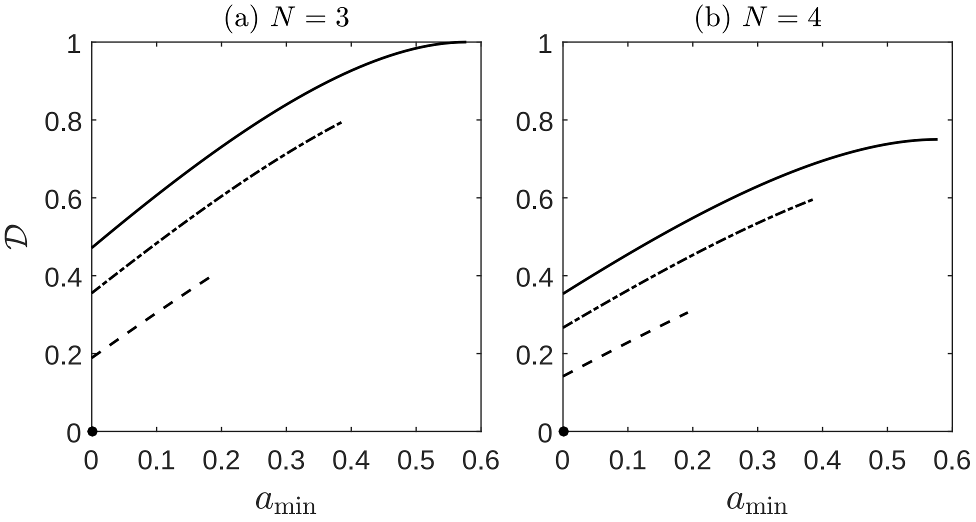

Figure 19 – Distinguishability vs $a_{\text{min}} \in [0, a_0]$ for (a) $N = 3$ and (b) $N = 4$ symmetric states of a qutrit defined by the coefficients given by Eq. (4.24), where $a_0 = 0$ (circle), $a_0 = 0.192$ (dashed line), $a_0 = 0.385$ (dash-dotted line), and $a_0 = 1/\sqrt{3}$ (solid line).

dots) and $D(\mathsf{d}|\mathsf{a})$ (green dots);[4] from left to right, we have $\xi = 0.01, 0.3, 0.6$, and 1. To assist in the analysis, we also computed these quantities considering input states generated with the coefficients (a_0, a_1, a_2) given by

$$a_0 = \{0, 0.192, 0.385, 1/\sqrt{3}\}, \tag{4.24a}$$

$$a_1 = a_{\text{min}} \in [0, a_0], \tag{4.24b}$$

$$a_2 = \sqrt{1 - a_0^2 - a_1^2}, \tag{4.24c}$$

that is, we choose a fixed value for a_0 which sets a variable $a_1 = a_{\text{min}}$ (a_2 is obtained from the normalization condition). The sets of states in each interval $a_{\text{min}} \in [0, a_0]$ are sorted in ascending order with respect to distinguishability, as shown in Fig. 19 for $N = 3$ and 4.

In Fig. 18 we plot $\mathcal{C}_{\text{rel}}(\hat{\rho}, \mathbf{\Pi}_{\text{SEP}})$, $C_r(\hat{\rho}_{\mathsf{a}})$, and $D(\mathsf{d}|\mathsf{a})$ for $N = 3$ states in the range $[0, a_0]$, where $a_0 = 0$ (circle), $a_0 = 0.192$ (dashed lines), $a_0 = 0.385$ (dash-dotted lines), and $a_0 = 1/\sqrt{3}$ (solid lines). For each range, the POVM coherence with respect to the distinguishability of the inputs, according to its components, either presents a monotonic increase[5] for low values of $\mathcal{D}$ or exhibits a nonmonotonic behavior otherwise. Later, we shall see that these behaviors influence the coherence for standard and concatenated FRIO measurements and are in sharp contrast with the coherence for ME. Then, we will exploit these results in Sec. 4.4.2 to compare the measurement strategies regarding the private randomness gain provided by each one.

---

[4] Note that the POVM coherence for state separation does not depend on N. Thus, for $N > 3$ it would have the same behavior shown in Fig. 18, but in a smaller range for distinguishability, i.e., $\mathcal{D} \in [0, n/N]$.

[5] Our selected sets of states given by Eqs. (4.24) cannot capture this behavior for $\xi = 0.01$.

Figure 18 shows that the main contribution to $\mathcal{C}_{\text{rel}}(\hat{\rho}, \mathbf{\Pi}_{\text{SEP}})$ comes from the ancilla's coherence. However, it can be shown that the total correlations between system and ancilla increase with the separation degree. Consequently, Eq. (4.20) implies that the ancilla's state becomes less pure with the transformation. As a result, the ancilla's coherence [Eq. (4.16)] decreases with ξ, and its contribution becomes more balanced with the quantum correlations between the two parts. The POVM coherence is zero only at the boundaries of $\mathcal{D}$, where $P_s = 0$ and $P_s = 1$, so that no further separation is possible in those cases. For $0 < \mathcal{D} < n/N$, it can be arbitrarily close to zero if $P_s \approx 0$ (e.g., for states with arbitrarily small a_{min}) or $P_s \approx 1$ (e.g., for arbitrarily small ξ). In this range, we also observe that the separation of input states with the same distinguishability will require different amounts of POVM coherence, which depend on an intricate relationship between the characteristics of the inputs[6] and the desired degree of separation. It can be shown that there are input states with the same $\mathcal{D}$ and quite distinct characteristics, which present opposite behaviors for coherence depending on ξ.

4.3.2 POVM coherence in standard FRIO measurement

The $(N+1)$-outcome POVM for the optimal standard FRIO measurement is built by the detection operators of Eq. (2.31), and the associated probabilities $\{p_0, \ldots, p_{N-1}, p^?\}$ will be given by

$$p_j = \text{Tr}[\hat{A}_j \hat{\rho} \hat{A}_j^\dagger] = \frac{P_s}{N}, \tag{4.25a}$$

$$p^? = \text{Tr}[\hat{A}^? \hat{\rho} \hat{A}^{?\dagger}] = Q. \tag{4.25b}$$

The post-measurement states for the conclusive and inconclusive outcomes are, respectively, $\hat{\rho}_j' = \hat{A}_j \hat{\rho} \hat{A}_j^\dagger / p_j = |u_j\rangle\langle u_j|$ [Eq. (2.7)] and $\hat{\rho}^? = \hat{A}^? \hat{\rho} \hat{A}^{?\dagger}/p^? = \hat{\rho}_f$ [Eq. (4.12c)], so that $S(\hat{\rho}_j') = 0$ and $S(\hat{\rho}_f) \geq 0$. Therefore, from Eq. (4.7), the required coherence to implement this POVM on the input state $\hat{\rho}$ will be

$$\mathcal{C}_{\text{rel}}(\hat{\rho}, \mathbf{\Pi}_{\text{FRIO}}) = H_2(P_s) + P_s \log_2 N + Q S(\hat{\rho}_f) - S(\hat{\rho}). \tag{4.26}$$

We can rewrite the expression above in a more instructive form by noting that, in the ME measurement, where $\xi = 0 \Rightarrow P_s = 1$, the coherence required to implement the corresponding POVM on $\hat{\rho}$ will be

$$\begin{aligned}\mathcal{C}_{\text{rel}}(\hat{\rho}, \mathbf{\Pi}_{\text{ME}}) &= \mathcal{C}_{\text{rel}}(\hat{\rho}, \mathbf{\Pi}_{\text{FRIO}})|_{\xi=0} \\ &= \log_2 N - S(\hat{\rho}).\end{aligned} \tag{4.27}$$

Then, using Eq. (4.19), we obtain

$$\mathcal{C}_{\text{rel}}(\hat{\rho}, \mathbf{\Pi}_{\text{FRIO}}) = \mathcal{C}_{\text{rel}}(\hat{\rho}, \mathbf{\Pi}_{\text{SEP}}) + P_s \mathcal{C}_{\text{rel}}(\hat{\rho}_s, \mathbf{\Pi}_{\text{ME}}), \tag{4.28}$$

---

[6] Their coefficients $\{a_j\}$, the value of a_{min} and its multiplicity μ, and the associated output states $\hat{\rho}_s$ and $\hat{\rho}_f$.

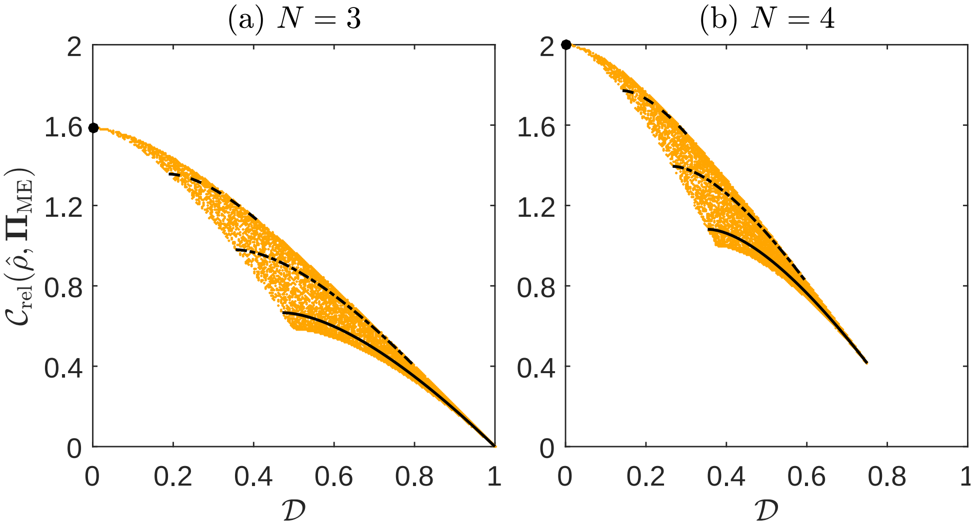

Figure 20 – POVM coherence vs distinguishability in the ME discrimination of (a) $N = 3$ and (b) $N = 4$ symmetric states of a qutrit. The orange dots represent 10^4 random input states while the plots represent the inputs in the range $a_{\text{min}} \in [0, a_0]$ [see Eq. (4.24)], where $a_0 = 0$ (circle), $a_0 = 0.192$ (dashed line), $a_0 = 0.385$ (dash-dotted line), and $a_0 = 1/\sqrt{3}$ (solid line).

where $\mathcal{C}_{\text{rel}}(\hat{\rho}_s, \mathbf{\Pi}_{\text{ME}}) = \log_2 N - S(\hat{\rho}_s)$. Reflecting the two-step nature of its implementation, the consumed coherence in the optimal FRIO discrimination is, thereby, split in the coherences for implementing state separation and the ME measurement on $\hat{\rho}_s$ weighted by the success rate.

Example: Discriminating N symmetric states of a qutrit with standard FRIO

Returning to the example introduced in Sec. 4.3.1, we now study the coherence in the optimal FRIO discrimination between N symmetric states of a qutrit. In what follows, we again use 10^4 random input states as well as fixed inputs defined by the coefficients in Eq. (4.24).

First, considering the ME measurement for $N = 3$ and 4, Fig. 20 shows the corresponding POVM coherence [Eq. (4.27)] as a function of distinguishability for the random input states (orange dots); the plots for the fixed inputs (black circle and lines) reveal a monotonic decreasing of $\mathcal{C}_{\text{rel}}(\hat{\rho}, \mathbf{\Pi}_{\text{ME}})$ with respect to $\mathcal{D}$. These results show a complementary relationship between this coherence and distinguishability as defined in Eq. (4.23).[7] The minimum of $\mathcal{C}_{\text{rel}}(\hat{\rho}, \mathbf{\Pi}_{\text{ME}})$, $\log_2 N/n$, is reached for maximally distinguishable inputs, showing that no coherence is consumed in the discrimination of orthogonal states. The maximum, $\log_2 N$, is reached for parallel input states, in which case no information is acquired and one obtains the maximum randomness of outcomes (see Sec. 4.4.2).

---

[7] In fact, the complementary nature between $\mathcal{D}$ given by Eq. (4.23) and coherence quantified by the l_1 norm has been found in Ref. [99]. Here, as the POVM coherence is quantified by an entropic measure, we should also define an entropic measure of distinguishability to establish a proper complementarity relation between these quantities. We will address this subject in the next chapter.

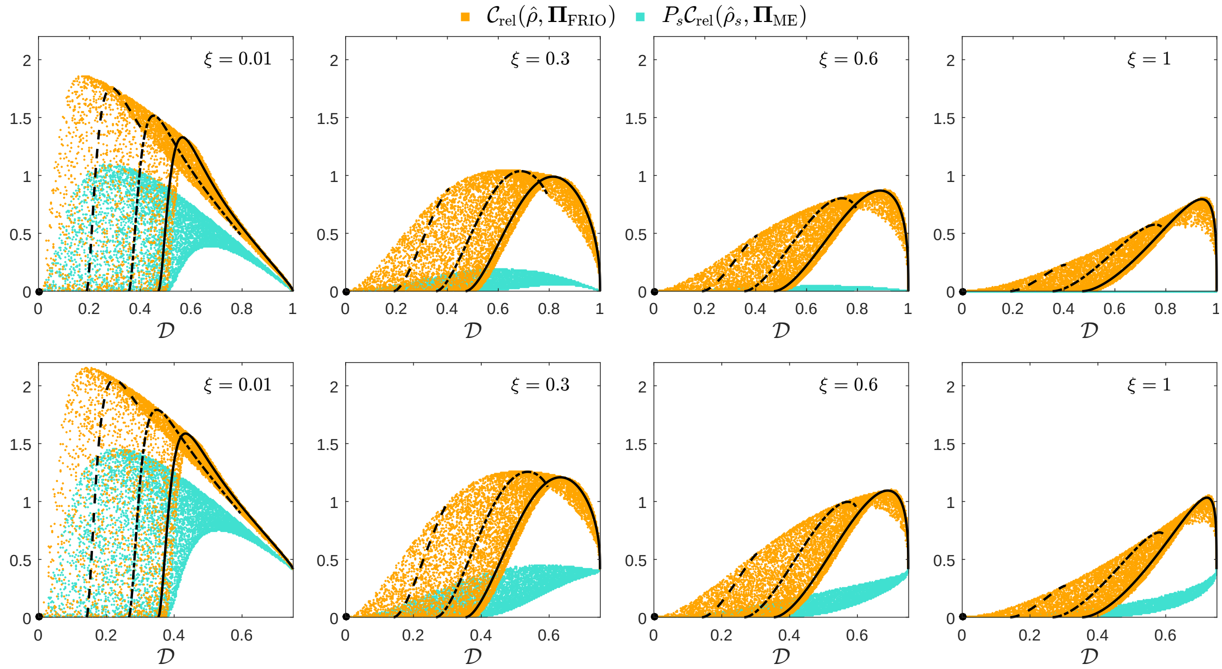

Figure 21 – POVM coherence (orange dots) and its component $P_s\mathcal{C}_{\rm rel}(\hat{\rho}_s, \mathbf{\Pi}_{\rm ME})$ (blue dots) vs distinguishability in the standard FRIO discrimination of $N = 3$ (top row) and 4 (bottom row) symmetric states of a qutrit. These quantities were computed for 10^4 random input states and a fixed value of the separation parameter ξ shown in the insets. We also plot the former for inputs in the range $a_{\rm min} \in [0, a_0]$ [see Eq. (4.24)], where $a_0 = 0$ (circle), $a_0 = 0.192$ (dashed lines), $a_0 = 0.385$ (dash-dotted lines), and $a_0 = 1/\sqrt{3}$ (solid lines).

We now address the coherence required for the standard FRIO measurement ($\xi > 0$). Using Eq. (4.28), in Fig. 21 we plot $\mathcal{C}_{\rm rel}(\hat{\rho}, \mathbf{\Pi}_{\rm FRIO})$ (orange dots) and the second term on the right-hand side (blue dots) as a function of $\mathcal{D}$ and ξ for the random input states; we also plot the former for the fixed inputs (black circle and lines). The top (bottom) row corresponds to $N = 3$ ($N = 4$) states to be discriminated. Note that the contribution from the first term on the right-hand side of Eq. (4.28), namely the POVM coherence for state separation, was discussed earlier (e.g., see Fig. 18). In the linearly independent case (top row), the coherence behavior is mainly dictated by the state separation stage (which is true whatever $n = N$), since the contribution from the second term in (4.28) is relevant only for $\xi \ll 1$. This occurs because the successfully separated states are more distinguishable, so that the required coherence for its ME discrimination, $\mathcal{C}_{\rm rel}(\hat{\rho}_s, \mathbf{\Pi}_{\rm ME})$, decreases with ξ. As a consequence, the coherence required to implement optimal UD ($\xi = 1$) is fully consumed at the separation stage, i.e.,

$$\mathcal{C}_{\rm rel}(\hat{\rho}, \mathbf{\Pi}_{\rm UD}) = \mathcal{C}_{\rm rel}(\hat{\rho}, \mathbf{\Pi}_{\rm SEP})|_{\xi=1}. \tag{4.29}$$

On the other hand, in the linearly dependent case (bottom row), the contribution from the second term in (4.28) is relevant for any ξ. In fact, since the coherence from state separation does not

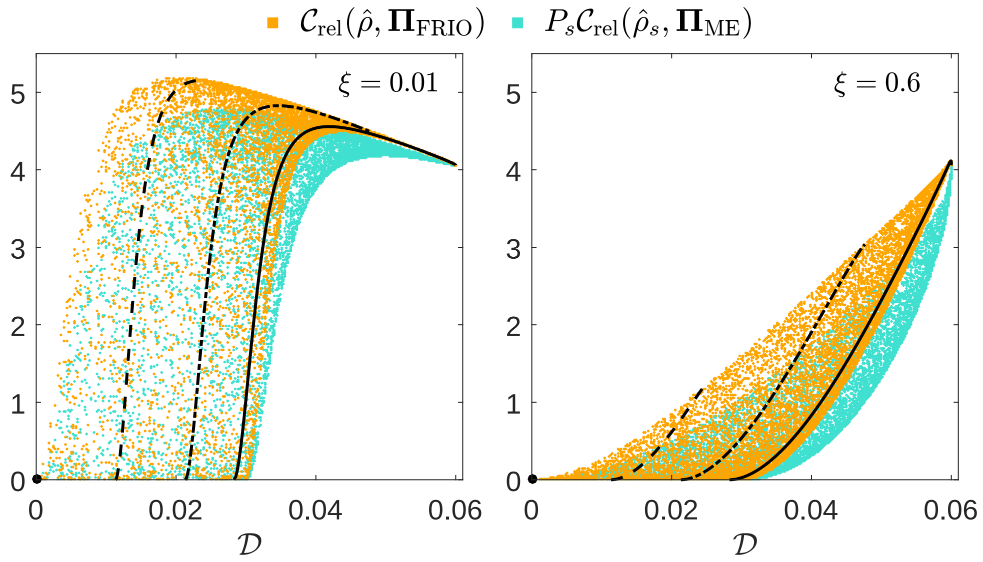

Figure 22 – POVM coherence (orange dots) and its component $P_s\mathcal{C}_{\rm rel}(\hat{\rho}_s, \mathbf{\Pi}_{\rm ME})$ (blue dots) vs distinguishability in the standard FRIO discrimination of $N = 50$ symmetric states of a qutrit. These quantities were computed for 10^4 random input states and a fixed value of the separation parameter ξ shown in the insets. We also plot the former for inputs in the range $a_{\rm min} \in [0, a_0]$ [see Eq. (4.24)], where $a_0 = 0$ (circle), $a_0 = 0.192$ (dashed lines), $a_0 = 0.385$ (dash-dotted lines), and $a_0 = 1/\sqrt{3}$ (solid lines).

depend on N, the contribution of $P_s\mathcal{C}_{\rm rel}(\hat{\rho}_s, \mathbf{\Pi}_{\rm ME})$ becomes dominant as the ratio N/n increases. In particular, it can be shown that for large N/n, this contribution dictates the coherence behavior, as we show in Fig. 22 for $N = 50$ symmetric states of a qutrit. This can be understood from the negligible effect that the separation has on increasing the distinguishability of the input states, which are very poorly distinguishable when $N \gg n$. Hence, the major coherence cost will come from the ME discrimination of the separated states weighted by P_s.

4.3.3 POVM coherence in concatenated FRIO measurement

The concatenation of optimal FRIO and ME measurements results in a $2N$-outcome POVM built by the detection operators of Eq. (2.39); the associated probabilities $\{p_j, p_j^f\}_{j=0}^{N-1}$ will be given by

$$p_j = \mathrm{Tr}[\hat{A}_j \hat{\rho} \hat{A}_j^\dagger] = \frac{P_s}{N}, \tag{4.30a}$$

$$p_j^f = \mathrm{Tr}[\hat{A}_j^f \hat{\rho} \hat{A}_j^{f\dagger}] = \frac{Q}{N}. \tag{4.30b}$$

In this case, the post-measurement states from both conclusive and inconclusive outcomes are pure, so from Eq. (4.7) the required coherence to implement this POVM on $\hat{\rho}$ will be

$$\mathcal{C}_{\rm rel}(\hat{\rho}, \mathbf{\Pi}_{\rm CONC}) = H_2(P_s) + \log_2 N - S(\hat{\rho}). \tag{4.31}$$

After simple algebraic manipulation, we can rewrite this expression as

$$\mathcal{C}_{\text{rel}}(\hat{\rho}, \mathbf{\Pi}_{\text{CONC}}) = \mathcal{C}_{\text{rel}}(\hat{\rho}, \mathbf{\Pi}_{\text{FRIO}}) + Q\mathcal{C}_{\text{rel}}(\hat{\rho}_f, \mathbf{\Pi}_{\text{ME}}), \tag{4.32}$$

where $\mathcal{C}_{\text{rel}}(\hat{\rho}, \mathbf{\Pi}_{\text{FRIO}})$ is the coherence for the standard FRIO measurement given by Eq. (4.28) and $\mathcal{C}_{\text{rel}}(\hat{\rho}_f, \mathbf{\Pi}_{\text{ME}}) = \log_2 N - S(\hat{\rho}_f)$ is the coherence required for discriminating the failure outputs of state separation via ME measurement [see Eq. (4.27)]. This latter coherence is bounded by

$$\log_2 N/(n-\mu) \leq \mathcal{C}_{\text{rel}}(\hat{\rho}_f, \mathbf{\Pi}_{\text{ME}}) \leq \log_2 N, \tag{4.33}$$

where the lower bound is attained for a maximally mixed $\hat{\rho}_f$ in an $(n-\mu)$-dimensional space, while the upper bound is achieved for a pure $\hat{\rho}_f$. Equation (4.32) shows that the POVM coherence in the concatenated FRIO measurement satisfies $\mathcal{C}_{\text{rel}}(\hat{\rho}, \mathbf{\Pi}_{\text{CONC}}) \geq \mathcal{C}_{\text{rel}}(\hat{\rho}, \mathbf{\Pi}_{\text{FRIO}})$, with equality holding only for $Q = 0$, which occurs when the input states are maximally distinguishable or $\xi = 0$ (when both strategies reduces to the ME measurement).

Example: Discriminating N symmetric states of a qutrit with concatenated FRIO

Here, we conclude the example discussed in the previous subsections, now studying the coherence in the concatenated FRIO discrimination between N symmetric states of a qutrit. Once again, we resort to 10^4 random input states and the fixed inputs defined by Eq. (4.24). Using Eq. (4.32), in Fig. 23 we plot $\mathcal{C}_{\text{rel}}(\hat{\rho}, \mathbf{\Pi}_{\text{CONC}})$ for both random (orange dots) and fixed inputs (black circle and lines), as well as the second term on the right-hand side (blue dots) as a function of $\mathcal{D}$ and ξ; the top (bottom) row corresponds to $N = 3$ ($N = 4$) states to be discriminated. The contribution from the first term on the right-hand side of (4.32), namely the POVM coherence for standard FRIO, was studied earlier and is shown in Fig. 21.

The results in Fig. 23 show that, in regard to the POVM coherence, the concatenated strategy presents similar aspects of both ME and standard FRIO measurements. Like ME, if the input states are parallel, i.e. $\mathcal{D} = 0$, we have $\mathcal{C}_{\text{rel}}(\hat{\rho}, \mathbf{\Pi}_{\text{CONC}}) = \mathcal{C}_{\text{rel}}(\hat{\rho}, \mathbf{\Pi}_{\text{ME}}) = \log_2 N$ for any ξ, as a consequence that a ME measurement is implemented on the failure outputs. On the other hand, like the standard FRIO, the POVM coherence presents a monotonic increasing or nonmonotonic behavior with respect to $\mathcal{D}$, as shown in the plots for the fixed inputs. This is a feature inherited from the state separation stage.

The term $Q\mathcal{C}_{\text{rel}}(\hat{\rho}_f, \mathbf{\Pi}_{\text{ME}})$ in Eq. (4.32) represents the extra amount of coherence that needs to be consumed for implementing the concatenated strategy instead of the standard one. It decreases with the distinguishability and increases with the separation degree. This latter behavior is dictated only by the failure rate Q, since $\mathcal{C}_{\text{rel}}(\hat{\rho}_f, \mathbf{\Pi}_{\text{ME}})$ does not depend on ξ. We also note from Fig. 23 that $\mathcal{C}_{\text{rel}}(\hat{\rho}, \mathbf{\Pi}_{\text{CONC}}) \approx Q\mathcal{C}_{\text{rel}}(\hat{\rho}_f, \mathbf{\Pi}_{\text{ME}})$ for states which $\mathcal{C}_{\text{rel}}(\hat{\rho}, \mathbf{\Pi}_{\text{FRIO}}) \approx 0$, namely the states with very small a_{min}, for which $P_s \approx 0$ and $S(\hat{\rho}_f) \approx S(\hat{\rho})$ for any ξ.

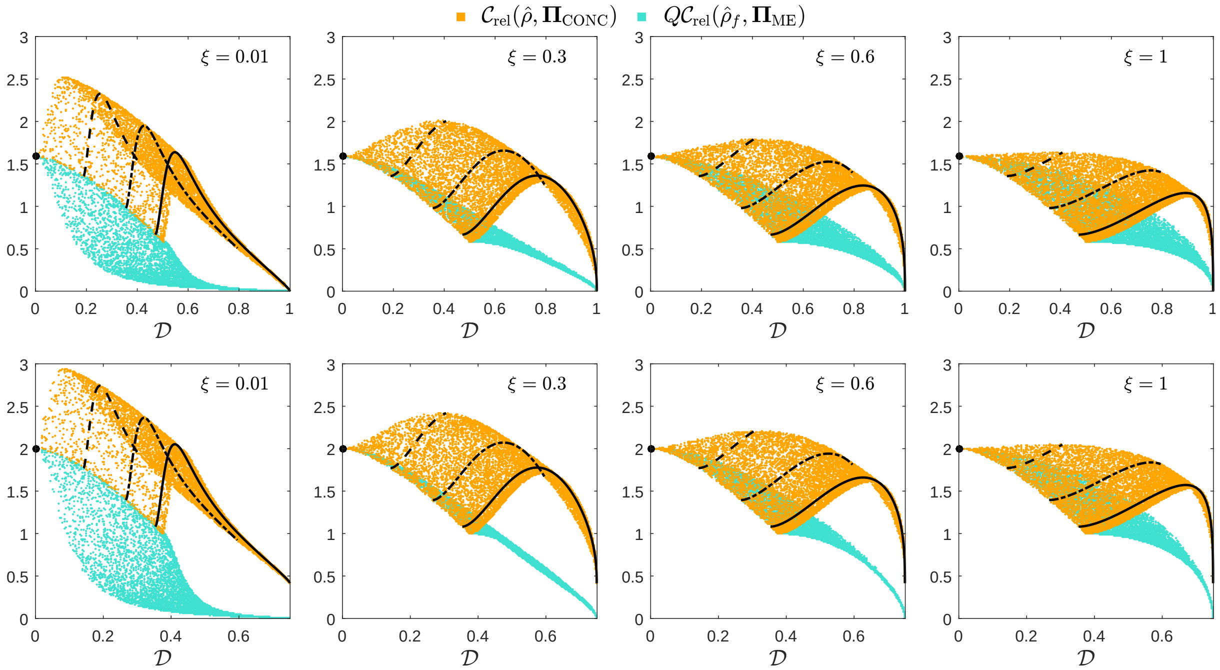

Figure 23 – POVM coherence (orange dots) and its component $Q\mathcal{C}_{\text{rel}}(\hat{\rho}_f, \mathbf{\Pi}_{\text{ME}})$ (blue dots) vs distinguishability in the concatenated FRIO discrimination of $N = 3$ (top row) and 4 (bottom row) symmetric states of a qutrit. These quantities were computed for 10^4 random input states and a fixed value of the separation parameter ξ shown in the insets. We also plot the former for inputs in the range $a_{\text{min}} \in [0, a_0]$ [see Eq. (4.24)], where $a_0 = 0$ (circle), $a_0 = 0.192$ (dashed lines), $a_0 = 0.385$ (dash-dotted lines), and $a_0 = 1/\sqrt{3}$ (solid lines).

4.4 Discussion

4.4.1 Bounds of POVM-based coherence

In Ref. [79], Bischof *et al.* show that for an N'-outcome POVM $\mathbf{\Pi}' = \{\hat{\Pi}'_i\}_{i=0}^{N'-1}$, the relative entropy of POVM-based coherence is bounded by $0 \le \mathcal{C}_{\text{rel}}(\hat{\rho}, \mathbf{\Pi}') \le \log_2 N'$. The upper bound is attained by the pure states that generate the highest entropy of measurement outcomes. The lower bound is attained for states that satisfy $\hat{\Pi}'_i \hat{\rho} \hat{\Pi}'_j = 0$ for all $i \neq j$, and $\hat{\rho}$ is POVM incoherent.

For the ME POVM there are N pure states whose coherence reaches the upper bound $\log_2 N$. They are given by $|j\rangle = \frac{1}{\sqrt{N}} \sum_k \omega^{-jk} |u_k\rangle$ for $j = 0, \ldots, N-1$, where $\{|u_k\rangle\}$ is the orthonormal basis given by the uniform states of Eq. (2.7) with $n = N$. A ME measurement [see Eq. (2.6)] on $|j\rangle$ yields, randomly, any outcome k with probability $1/N$, generating the maximal randomness. On the other hand, $\hat{\rho} = \frac{1}{n} \sum_{k \in \mathcal{I}} |k\rangle\langle k|$ is the only state with minimum coherence, $\log_2 N/n$. If $N = n$, this is the maximally mixed state $\hat{\rho} = \hat{I}/n$, which is then POVM incoherent. These bounds can be visualized in the example of Fig. 20 and extend the findings of [79] that considered the ME discrimination of symmetric states for $N = 3$ and $n = 2$.

For the standard and concatenated FRIO POVMs the upper bounds of coherence are $\log_2(N+1)$ and $\log_2 2N$, respectively. However, in both cases, there are no states that reach these bounds, no matter the value of ξ. The lower bound of coherence is attained both by $\{|j\rangle\}_{j=0}^{N-1}$ and $\hat{\rho} = \hat{I}/n$ in the standard case, and only by the latter in the concatenated case. The results shown in the examples of Figs. 21, 22, and 23 illustrate this discussion.

4.4.2 Private randomness

Quantum coherence is an operationally relevant quantity for quantum cryptography as it quantifies the private randomness of a measurement with respect to eavesdropping activities [91–93], an important result to secure quantum generation of random numbers [94, 95]. Briefly, let $\hat{\rho}_a$ be the state to be measured and consider an eavesdropper e that has access to a purification $\hat{\rho}_{ae} = |\psi\rangle\langle\psi|_{ae}$, so that $\hat{\rho}_a = \mathrm{Tr}_e\hat{\rho}_{ae}$. Applying the POVM $\mathbf{\Pi} = \{\hat{\Pi}_i = \hat{A}_i^\dagger\hat{A}_i\}$ on $\hat{\rho}_a$ and storing the outcomes i in a register x produces the output joint state

$$\hat{\rho}'_{xae} = \sum_i p_i|i\rangle\langle i|_x \otimes |\psi_i\rangle\langle\psi_i|_{ae}, \tag{4.34}$$

where $|\psi_i\rangle_{ae} = \frac{1}{\sqrt{p_i}}(\hat{A}_i \otimes \hat{I})|\psi\rangle_{ae}$ and $p_i = \mathrm{Tr}(\hat{\Pi}_i\hat{\rho}_a)$. Bischof *et al.* [93] define the randomness of the measurement $\mathbf{\Pi}$ as

$$R_{x|e}(\hat{\rho}_a) \equiv \min_{\hat{\rho}_{ae}} S(x|e)_{\hat{\rho}'_{xe}}, \tag{4.35}$$

where $S(x|e)_{\hat{\rho}'_{xe}} = S(\hat{\rho}'_{xe}) - S(\hat{\rho}'_e)$ denotes the conditional von Neumann entropy, $\hat{\rho}'_{xe} = \mathrm{Tr}_a\hat{\rho}'_{xae}$, $\hat{\rho}'_e = \mathrm{Tr}_{xa}\hat{\rho}'_{xae}$, and the minimization is taken over all purifications. Then they show that

$$R_{x|e}(\hat{\rho}_a) = \mathcal{C}_{\text{rel}}(\hat{\rho}_a, \mathbf{\Pi}), \tag{4.36}$$

i.e., the POVM coherence quantifies the rate of measurement outcomes that are unpredictable to the eavesdropper. This is a generalization of previous results by Yuan *et al.* [91, 92] concerning the standard relative entropy of coherence.

In the state discrimination scenario, if the inputs are orthogonal, then $\hat{\rho}_a = \hat{I}/N$, and the eavesdropper will hold a maximally entangled purification

$$|\psi\rangle_{ae} = \frac{1}{\sqrt{N}} \sum_{j=0}^{N-1} |u_j\rangle_a \otimes |j\rangle_e. \tag{4.37}$$

In this case, e can always uncover the bits generated by the measurement, making secrecy unreachable. Therefore, the measurement outcome privacy lies on the nonorthogonality of the input states, which is verified by the fact that coherence vanishes in all cases where the inputs are perfectly distinguishable (e.g., see Figs. 20, 21, and 23).

Our results show that there are optimal intermediate values for the input set distinguishability in terms of maximizing coherence (see Figs. 21 and 23). This feature is not observed for the ME measurement, for which coherence decreases monotonically with distinguishability (Fig. 20): this means that the maximum coherence is achieved for identical states, for which discrimination is useless. In this way, the standard and concatenated FRIO schemes benefit scenarios where both the ability to discriminate quantum states and the outcomes secrecy with respect to eavesdropping are relevant figures of merit. In both cases, the optimal distinguishability that maximizes coherence increases with the separation parameter ξ, a feature that is more pronounced for the standard measurement. Note that for any ξ the concatenated strategy outperforms the standard one (including ME) in terms of private bit generation. Take, for example, the case of $N = 4$ states of a qutrit and separation parameter $\xi = 1$ (bottom rows of Figs. 21 and 23): whereas the concatenated scheme can achieve up to two secret bits *per* measurement the standard strategy only achieves around one bit.

4.5 Summary and outlook

We presented a detailed study on POVM-based coherence as a resource for standard and concatenated FRIO discrimination of equally likely symmetric states in arbitrary dimensions. We showed that the POVM coherence in the assisted separation stage decomposes into the coherence of the ancillary state and the quantum discord between the system and the ancilla, evidencing coherence as a more elementary resource than quantum correlations. This relation may pave the way for a deeper understanding of the measure in Eq. (4.7) from a fundamental perspective. Quantum coherence has traditionally been viewed as a quantification of the strength of superposition [77, 78], and, further, as a measure of intrinsic randomness [91–93]. It is therefore highly relevant that, at least in the particular case addressed here, its formal extension to generalized measurements [79] embraces the definition of quantum discord at its core. A more general result in this direction was not the purpose of this thesis, and we leave further investigation on the subject to future research.

The operational meaning of the POVM-based coherence in terms of private random bit generation was discussed, and we showed how standard and concatenated FRIO measurements can outperform the ME strategy with respect to this figure of merit. In particular, it was shown that the concatenation of the failure outputs of state separation leads to better secret bit generation rates compared to standard FRIO. These findings may be useful in high-dimensional quantum random number generation and quantum cryptography [55, 91–95].

5 Wave-particle duality and quantum state discrimination

"And deep beneath the rolling waves, in labyrinths of coral caves."
Echoes, Pink Floyd

Wave-particle duality relations are quantitative statements on the trade-off between the "strength" of interference effects produced by individual quantum systems in an interferometer and the knowledge about which path they took inside it. In this chapter, we investigate these relations by considering a system that, upon entering an N-path interferometer, interacts with a quantum detector in such a way that each possible path is tagged by a pure, symmetric state of the detector. Taking quantum coherence in the path basis as a measure of interference strength and the mutual information obtained via detector-state discrimination as a measure of which-path knowledge, we employ the measurement strategies presented in Chapter 2 to derive entropic wave-particle duality relations for N-path interferometers with $N \geq 2$ equally likely paths.

5.1 Historical background

The realization that, at the quantum level, certain pairs of properties cannot be observed or measured simultaneously lies at the heart of human understanding of the quantum world [100]. This concept was introduced by Niels Bohr in 1927 as the *complementarity principle* [101], motivated by the fundamental challenge of understanding the wave-particle duality exhibited by a quantum particle in a two-path interferometer—a phenomenon that Richard Feynman later described as "the only mystery" of quantum mechanics [102]. The initial discussions on the dual wave-particle behavior gained historical prominence, due to the intellectual dispute between Niels Bohr and Albert Einstein [100]. After Bohr's views prevailed over Einstein's, marking the triumph of quantum over the classical descriptions, the topic received relatively little attention until the late 1970s, when it gained a new boost with the pioneering work of Wootters and Zurek [103], who showed that wave- and particle-like behaviors can coexist. Since then, several studies have focused on developing quantitative measures of these complementary aspects [99, 104–119].

The first explicit quantitative statement of a trade-off between measures of wave and particle behavior—namely, a wave-particle duality relation—can be attributed to Greenberger and YaSin [107]. They considered an individual quantum system (*quanton*[1]) in a two-path

---

[1] Throughout this chapter, we use the term *quanton* to refer to an individual quantum system in an interferometer.

interferometer, where its wave behavior is quantified by the *a priori* fringe visibility ($\mathcal{V}_0$) and its particle behavior by the path predictability ($\mathcal{P}$), resulting in the trade-off

$$\mathcal{V}_0^2 + \mathcal{P}^2 \leq 1. \tag{5.1}$$

The which-way information is acquired predictively by using prior knowledge about the probabilities for the quanton to follow each path and betting on the most likely one. In addition, prior knowledge of the quantons' superposition in the path basis allows one to estimate, *a priori*, the fringe visibility of the interference pattern they will produce.

The essence of the discussion on wave-particle duality, as conceived by Einstein's recoiling-slit proposal to confront Bohr's complementarity principle [100], relied on active intervention in the experiment to obtain which-way knowledge. Thus, the scenario addressed by Greenberger and YaSin in [107], based solely on predictive analysis using *a priori* information, was unable to capture it adequately. Addressing the discussion from a fully quantum mechanical perspective, Englert considered two-path interferometers supplemented by an auxiliary quantum system functioning as a which-way detector [110]. This system stores which-way information in its states through a unitary coupling with the quanton inside the interferometer. The amount of which-way information that becomes available in this process is quantified by the distinguishability ($\mathcal{D}$) of the detector states and can be extracted retrodictively by an optimal measurement that discriminates between them. (Note that a non-optimal measurement can only extract part of the available information.) As a consequence of the quanton-detector coupling, the fringe visibility ($\mathcal{V}$) of the quantons' interference pattern will decrease in comparison to the *a priori* visibility; unlike $\mathcal{V}_0$, $\mathcal{V}$ is an *a posteriori* visibility. In this retrodictive scenario, the trade-off between the quantifiers of wave and particle behaviors is given by

$$\mathcal{V}^2 + \mathcal{D}^2 \leq 1. \tag{5.2}$$

It is interesting to note that there is a connection between predictive and retrodictive scenarios. When both *a priori* information and which-path detectors are available, the relation in Eq. (5.2) can be expressed as

$$\frac{1 - \mathcal{P}^2}{\mathcal{V}_0^2}\mathcal{V}^2 + \mathcal{D}^2 \leq 1, \tag{5.3}$$

where the equal sign holds always if two conditions are met before the quanton-detector interaction takes place: the which-way detector is in a pure state, and the quanton state is a uniform superposition of the path-basis states (so that $\mathcal{P} = 0$ and $\mathcal{V}_0 = 1$).

This term, adopted by Englert in Ref. [110], was coined by the physicist and philosopher Mario Bunge in 1973 to avoid associating classical notions such as "particle" or "wave" with quantum objects.

Once the wave-particle duality relation was fully understood in the two-path case, a natural next step was to explore its extension to interferometers with more than two paths. Early attempts [113–116], both in predictive and retrodictive scenarios, faced difficulties in generalizing the notion of visibility in a consistent and physically meaningful way. More recent developments, however, have succeeded in capturing the wave-like behavior of a quanton in a multipath interferometer by associating it with the quantum coherence of its state in the path basis [99, 117–119]. Another obstacle in extending the duality relation is the lack of an analytical expression for distinguishability in the general case. This limits the analysis of particle-like behavior to the amount of path information accessible through a given measurement, which may underestimate the true distinguishability. In the remainder of this chapter, we adopt the coherence-based approach to characterize the wave-like behavior, while the particle-like behavior is quantified by the which-path knowledge extracted via discrimination strategies. Using this framework, we derive entropic wave-particle duality relations for a quanton traversing an interferometer with N equally probable paths, each tagged by a symmetric state of a which-path detector.

5.2 Entropic wave-particle duality relation in a multipath interferometer

5.2.1 General interferometric scenario

Consider a quanton that, upon entering an N-path interferometer, is put in the superposition state

$$|\psi\rangle_q = \sum_{\ell=0}^{N-1} \sqrt{\eta_\ell}|\ell\rangle_q, \tag{5.4}$$

where $\{|\ell\rangle_q\}_{\ell=0}^{N-1}$ denotes the orthonormal basis corresponding to the N possible paths and η_ℓ is the probability of taking the ℓth path. Inside the interferometer, the quanton interacts with another quantum system, assumed to be in a fixed pure state $|\alpha_0\rangle_d$, through a controlled unitary operation

$$\hat{\mathcal{U}}_{qd}|\ell\rangle_q|\alpha_0\rangle_d = |\ell\rangle_q|\alpha_\ell\rangle_d, \tag{5.5}$$

which transforms the initial bipartite state $|\psi\rangle_q|\alpha_0\rangle_d$ into

$$|\Psi\rangle = \sum_{\ell=0}^{N-1} \sqrt{\eta_\ell}|\ell\rangle_q|\alpha_\ell\rangle_d. \tag{5.6}$$

The correlation generated by this interaction allows one to obtain information about which path the quanton has taken by measuring the auxiliary system. Therefore, this system acts as a which-way detector.

5.2.2 Characterizing wave-like properties

Following recent approaches [99, 119], we use the relative entropy of coherence [Eq. (4.2)] in the path basis as a measure to characterize the quanton's wave-like properties in the interferometric scenario described above. First, we compute the *a priori* coherence, i.e., the coherence of the quanton before its interaction with the detector takes place. Using Eq. (5.4), we obtain

$$C_r^0(|\psi\rangle_q\langle\psi|) = H(\{\eta_\ell\}), \tag{5.7}$$

where $H(\{\eta_\ell\})$ is the Shannon entropy of the path probability distribution. After the interaction, the quanton's state is found by tracing out the detector in Eq. (5.6):

$$\begin{aligned}\hat{\rho}_q &= \mathrm{Tr}_d|\Psi\rangle\langle\Psi| \\ &= \sum_{\ell,\ell'=0}^{N-1}\sqrt{\eta_\ell\eta_{\ell'}}\langle\alpha_{\ell'}|\alpha_\ell\rangle|\ell\rangle_q\langle\ell'|.\end{aligned} \tag{5.8}$$

The coherence of this state is given by

$$C_r(\hat{\rho}_q) = H(\{\eta_\ell\}) - S(\hat{\rho}_q) = H(\{\eta_\ell\}) - S(\hat{\rho}_d), \tag{5.9}$$

where

$$\begin{aligned}\hat{\rho}_d &= \mathrm{Tr}_q|\Psi\rangle\langle\Psi| \\ &= \sum_{\ell=0}^{N-1}\eta_\ell|\alpha_\ell\rangle_d\langle\alpha_\ell|.\end{aligned} \tag{5.10}$$

is the detector's state after the interaction; in the last step of (5.9) we used the fact that $S(\hat{\rho}_q) = S(\hat{\rho}_d)$, since the global state is pure. Comparing Eqs. (5.7) and (5.9), we observe that $C_r(\hat{\rho}_q) \leq C_r^0(|\psi\rangle_q\langle\psi|)$, with the equality holding if and only if $|\alpha_\ell\rangle = |\alpha_0\rangle$ for all ℓ. This shows that the process of acquiring which-path knowledge via coupling to a which-way detector inevitably reduces the coherence of the quanton. In particular, when the detector states are mutually orthogonal, we have $S(\hat{\rho}_q) = S(\hat{\rho}_d) = H(\{\eta_\ell\})$. In this case, the coherence vanishes, meaning that no interference effects emerge due to the availability of full which-path information in the detector.

The effective quantity that we will use to characterize the quanton's wave-like properties is the normalized version of Eq. (5.9), given by

$$\mathcal{C} = \frac{C_r(\hat{\rho}_q)}{\log_2 N}, \tag{5.11}$$

which satisfies $0 \leq \mathcal{C} \leq 1$. For simplicity, in this chapter we will refer to this normalized quantity as coherence.

5.2.3 Characterizing particle-like properties

As described above, the coupling with the quanton stores which-path information in the detector. To gain knowledge about the quanton's path, one must perform a measurement that discriminates the detector states, noting that not all measurements can extract all the available information. In this context, following Refs. [99, 119], we characterize the particle-like properties of the quanton by the mutual information between the detector states and the outcomes of a measurement designed to discriminate them.

Let D and M be the random variables associated with the detector states and the measurement outcomes, respectively. We can express the mutual information between them as

$$I(M:D) = H(D) - H(D|M), \tag{5.12}$$

where $H(D|M)$ denotes the conditional entropy of D given M. The variable D takes values in the set $\{\ell\}_{\ell=0}^{N-1}$, corresponding to the state $|\alpha_\ell\rangle$, with probability η_ℓ; hence, $H(D) = H(\{\eta_\ell\})$. On the other hand, M takes values in the set $\{j\}_{j=0}^{N'-1}$, corresponding to the outcome probabilities $p_j = \text{Tr}(\hat{\Pi}_j \hat{\rho}_d)$ of a given measurement $\mathbf{\Pi} = \{\hat{\Pi}_j\}_{j=0}^{N'-1}$ performed on the detector. Note that N' depends on the chosen discrimination strategy. For instance, in the strategies discussed in Chapter 2, we have $N' = N$ for ME measurement, $N' = N + 1$ for optimal FRIO, and $N' = 2N$ for concatenated FRIO. $H(D|M)$ can be written as the statistical sum of the Shannon entropies of the conditional probability distributions $p(\alpha_\ell|j)$,

$$H(D|M) = \sum_{j=0}^{N'-1} p_j H(\{p(\alpha_\ell|j)\}). \tag{5.13}$$

Thus, the mutual information between M and D is given by

$$I(M:D) = H(\{\eta_\ell\}) - \sum_{j=0}^{N'-1} p_j H(\{p(\alpha_\ell|j)\}). \tag{5.14}$$

Similarly to coherence, we use the normalized version of this quantity to characterize the quanton's particle-like properties:

$$\mathcal{K}(\mathbf{\Pi}) = \frac{I(M:D)}{\log_2 N}, \tag{5.15}$$

which satisfies $0 \leq \mathcal{K}(\mathbf{\Pi}) \leq 1$. The notation $\mathcal{K}(\mathbf{\Pi})$ highlights that this quantity—which we refer to as *which-path knowledge* [111, 112]—depends on the specific discrimination strategy applied, expressed by the second term on the right-hand side of Eq. (5.14). When the measurement is able to extract all the available information stored in the detector states, $\mathcal{K}(\mathbf{\Pi})$ reaches its maximum value:

$$\mathcal{D} = \max_{\mathbf{\Pi}} \mathcal{K}(\mathbf{\Pi}). \tag{5.16}$$

The maximum mutual information over all POVMs is known as the *accessible information*; in the context of wave-particle duality relations, it corresponds to the path *distinguishability* [99, 110]. Unfortunately, as with any other discrimination strategy, there is no general solution to the problem of finding the accessible information.

5.2.4 Entropic wave-particle duality relation

Holevo's theorem [120] establishes that $I(M:D) \leq S(\hat{\rho}_d) - \sum_\ell \eta_\ell S(|\alpha_\ell\rangle_d\langle\alpha_\ell|) = S(\hat{\rho}_d)$. From Eq. (5.9), this can be rewritten as $I(M:D) \leq H(\{\eta_\ell\}) - C_r(\hat{\rho}_q)$. Dividing both sides by $\log_2 N$, we obtain $\mathcal{K}(\mathbf{\Pi}) \leq 1 - \mathcal{C}$. Therefore, using Eqs. (5.9) and (5.14), we find

$$\mathcal{C} + \mathcal{K}(\mathbf{\Pi}) = \frac{2H(\{\eta_\ell\}) - S(\hat{\rho}_d) - \sum_{j=0}^{N'-1} p_j H(\{p(\alpha_\ell|j)\})}{\log_2 N} \leq 1. \tag{5.17}$$

This is the entropic wave-particle duality relation between coherence and accessible which-path knowledge that we will explore in the remainder of the chapter.

5.3 Uniform N-path interferometers with symmetric detector states

5.3.1 Interferometric scenario

In this section, we analyze an N-path interferometer assuming a uniform path probability distribution for the quanton (i.e., $\eta_\ell = 1/N$ for all ℓ). In this so-called *uniform* interferometer, we also assume that the controlled unitary coupling between the quanton and the which-way detector is given by

$$\hat{\mathcal{U}}_{qd} = \sum_{\ell=0}^{N-1} |\ell\rangle_q\langle\ell| \otimes \hat{V}_d^\ell, \tag{5.18}$$

where $\hat{V}_d$ is defined in Eq. (2.5), which leads to symmetric detector states $\{|\alpha_\ell\rangle_d\}_{\ell=0}^{N-1}$ [see Eq. (2.2)]. As a result, the problem of acquiring which-path knowledge amounts to discriminating equiprobable symmetric states, for which the measurement strategies from Chapter 2 can be applied. Although this scenario may seem restrictive, we will see that it provides valuable physical insights into the problem.

In a uniform interferometer, the path predictability of the quanton is zero, while the normalized *a priori* coherence is maximal, i.e., $\mathcal{C}^0 = C_r^0(|\psi\rangle_q\langle\psi|)/\log_2 N = 1$ [see Eq. (5.7)]. After coupling to the which-way detector, Eqs. (5.9) and (5.11) show that the quanton's coherence is reduced to

$$\mathcal{C} = 1 - \frac{S(\hat{\rho}_d)}{\log_2 N}. \tag{5.19}$$

Interestingly, the *a priori* scenario can be completely reversed. If the detector states are mutually orthogonal, we have $S(\hat{\rho}_d) = \log_2 N$, so that the *a posteriori* coherence vanishes. In this case, a projective measurement in the detector basis yields exact which-path information. Uniform interferometers, therefore, offer the most striking contrast between predictive and retrodictive wave-particle duality relations.

As a final comment, by comparing Eq. (5.19) with Eq. (4.27), we find that

$$\mathcal{C} = \frac{\mathcal{C}_{\text{rel}}(\hat{\rho}_d, \mathbf{\Pi}_{\text{ME}})}{\log_2 N}. \tag{5.20}$$

This means that the quanton's coherence in a uniform interferometer corresponds to the amount of coherence consumed in performing the ME measurement on the detector state $\hat{\rho}_d$. It remains unclear to us whether this result has a deeper physical significance or is merely coincidental.

5.3.2 Wave-particle duality with standard FRIO measurement

Here, we consider the case in which the detector states are discriminated using the standard FRIO measurement. As discussed in Sec. 2.4, this strategy is characterized by the parameter $\xi \in [0, 1]$, which means that the conditional probability appearing in Eq. (5.13) depends on ξ. From Bayes' rule, it can be expressed as

$$p(\alpha_\ell | j) = \frac{p(j|\alpha_\ell)}{N p_j}. \tag{5.21}$$

Using the POVM defined by the detection operators of this strategy [Eq. (2.31)], the probabilities of conclusive $\{p(j|\alpha_\ell)\}_{j=0}^{N-1}$ and inconclusive $p(?|\alpha_\ell)$ identifications of the detector states will be given by

$$p(j|\alpha_\ell) = \langle \alpha_\ell | \hat{\Pi}_j(\xi) | \alpha_\ell \rangle = P_s(\xi) \langle \beta_\ell(\xi) | \hat{\Pi}_j^{\text{ME}} | \beta_\ell(\xi) \rangle, \tag{5.22}$$

$$p(?|\alpha_\ell) = \langle \alpha_\ell | \hat{\Pi}_?(\xi) | \alpha_\ell \rangle = Q(\xi), \tag{5.23}$$

where $P_s(\xi) = 1 - Q(\xi)$, $|\beta_\ell(\xi)\rangle$, and $\hat{\Pi}_j^{\text{ME}}$ are defined in Eqs. (2.23), (2.21a), and (2.6), respectively. The total probabilities of obtaining conclusive and inconclusive outcomes are given by $p_j = \frac{1}{N}\sum_{\ell=0}^{N-1} p(j|\alpha_\ell) = P_s(\xi)/N$ and $p_? = \frac{1}{N}\sum_{\ell=0}^{N-1} p(?|\alpha_\ell) = Q(\xi)$. Therefore, the conditional probability distribution for the standard FRIO measurement reads

$$p(\alpha_\ell | j) = \langle \beta_\ell(\xi) | \hat{\Pi}_j^{\text{ME}} | \beta_\ell(\xi) \rangle \equiv \lambda_{j\ell}(\xi), \tag{5.24}$$

$$p(\alpha_\ell | ?) = \frac{1}{N}, \tag{5.25}$$

where the latter corresponds to a random guess of the detector state, and thus of the quanton's path. By replacing this distribution into Eq. (5.14), and noting that $H(\{\lambda_{j\ell}(\xi)\})$ is identical for all $j = 0, \ldots, N-1$, the which-path knowledge can be written as

$$\mathcal{K}(\mathbf{\Pi}_{\text{FRIO}}) = P_s(\xi)\left(1 - \frac{H(\{\lambda_{0\ell}(\xi)\})}{\log_2 N}\right). \tag{5.26}$$

As expected, this quantity vanishes when $P_s = 0$, as all outcomes are inconclusive and discarded. Finally, for the standard FRIO measurement, the duality relation (5.17) becomes

$$\mathcal{C} + \mathcal{K}(\mathbf{\Pi}_{\text{FRIO}}) = 1 - \frac{S(\hat{\rho}_d)}{\log_2 N} + P_s(\xi)\left(1 - \frac{H(\{\lambda_{0\ell}(\xi)\})}{\log_2 N}\right) \leq 1. \tag{5.27}$$

The above relation is trivially saturated when the detector states are orthogonal, in which case $\mathcal{K}(\mathbf{\Pi}_{\text{FRIO}}) = 1$ for all ξ, or when they are all identical, leading to $\mathcal{C} = 1$ (which is not a case of interest). Relevant particular cases are easily derived from Eq. (5.26), as we show next.

Extreme cases: ME and optimal MC measurements

When performing the ME measurement ($\xi = 0$, and hence $P_s = 1$) to discriminate the detector states, the which-path knowledge is given by

$$\mathcal{K}(\mathbf{\Pi}_{\text{ME}}) = 1 - \frac{H(\{\lambda_{0\ell}(0)\})}{\log_2 N}. \tag{5.28}$$

The ME POVM for discriminating equiprobable symmetric states is given by $\hat{\Pi}_j = \frac{n}{N}|u_j\rangle\langle u_j| = \hat{\Phi}^{-1/2}|\alpha_j\rangle\langle\alpha_j|\hat{\Phi}^{-1/2}$, where $\hat{\Phi} = \sum_{j=0}^{N-1}|\alpha_j\rangle\langle\alpha_j|$. This measurement, known as the square-root measurement [121], has two important features regarding the maximization of the mutual information. First, it provides a close approximation to the accessible information when the states to be discriminated are equally likely and nearly orthogonal [122]. Second, it satisfies the necessary (but not sufficient) condition for attaining the accessible information [42]. Accordingly, the ME discrimination of the detector states yields an extremum—though not necessarily a maximum—of the which-path knowledge, and closely approximates $\mathcal{K}_{\max}$ when ${}_d\langle\alpha_\ell|\alpha_{\ell'}\rangle_d \approx 0$ for all $\ell \neq \ell'$. The equality $\mathcal{K}(\mathbf{\Pi}_{\text{ME}}) = \mathcal{K}_{\max}$ always holds for two-path interferometers,[2] as the optimal measurements for both criteria coincide [123]. For interferometers with $N > 2$ paths, the equality holds only at the saturation points of the duality relation.

In the other extreme ($\xi = 1$), the detector states are discriminated via optimal MC measurement. If the states are linearly independent (so that the optimal MC becomes the optimal UD), we have that $\lambda_{j\ell} = \delta_{j\ell}$ [see Eq. (5.24)], and the which-path knowledge becomes

$$\mathcal{K}(\mathbf{\Pi}_{\text{UD}}) = P_s. \tag{5.29}$$

This is in accordance with [119] for equiprobable states.

---

[2] In Englert's derivation of the duality relation for two-path interferometers, distinguishability is obtained through the ME measurement [**?**].

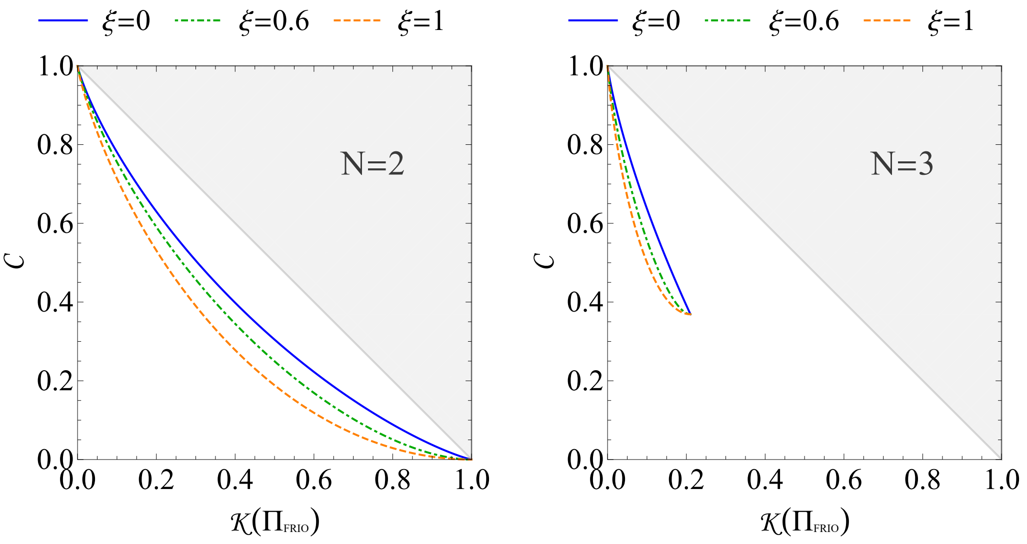

Figure 24 – Coherence vs which-path knowledge for uniform interferometers with $N = 2$ (left) and $N = 3$ (right) paths, which are marked with a qubit detector. The detector states are discriminated via ME ($\xi = 0$), optimal FRIO ($\xi = 0.6$), and optimal MC/UD ($\xi = 1$). The shaded area is the region forbidden by the duality relation.

Numerical results and discussion

To illustrate the above results, we start by considering two- and three-path interferometers supplemented by a two-dimensional detector. In Fig. 24, we plot $\mathcal{C}$ [Eq. (5.19)] as a function of $\mathcal{K}(\mathbf{\Pi}_{\text{FRIO}})$ [Eq. (5.26)] for $N = 2$ (left panel) and $N = 3$ (right panel), using three values of the separation parameter: $\xi = 0$ (solid line), $\xi = 0.6$ (dot-dashed line), and $\xi = 1$ (dashed line). Clearly, the bound in the duality relation (5.27) is tightest for the ME measurement ($\xi = 0$) and becomes progressively looser as ξ increases. In the case of linearly dependent detector states (right panel), the which-path knowledge never reaches unity, and the duality relation is saturated only when $\mathcal{C} = 1$. This contrasts with the linearly independent case, where the detector states can be orthogonal, allowing $\mathcal{K}(\mathbf{\Pi}_{\text{FRIO}}) = 1$.

The most relevant case in current studies of wave–particle duality involves quantons and detectors in dimensions greater than two. In the remainder of this section, we present the results of numerical simulations for this scenario, carried out as follows. First, we fix the number of paths in the interferometer (N) and the dimension of the detector's Hilbert space (n). Then, we generate X_d random sets of detector states; from each set, we compute the quanton's coherence using Eq. (5.19) and the which-path knowledge using Eq. (5.26), for a fixed value of the parameter ξ. The obtained results are displayed in a scatter plot of $\mathcal{C}$ versus $\mathcal{K}(\mathbf{\Pi})$. In all subsequent plots, the shaded area corresponds to the region forbidden by the duality relation in Eq. (5.17).

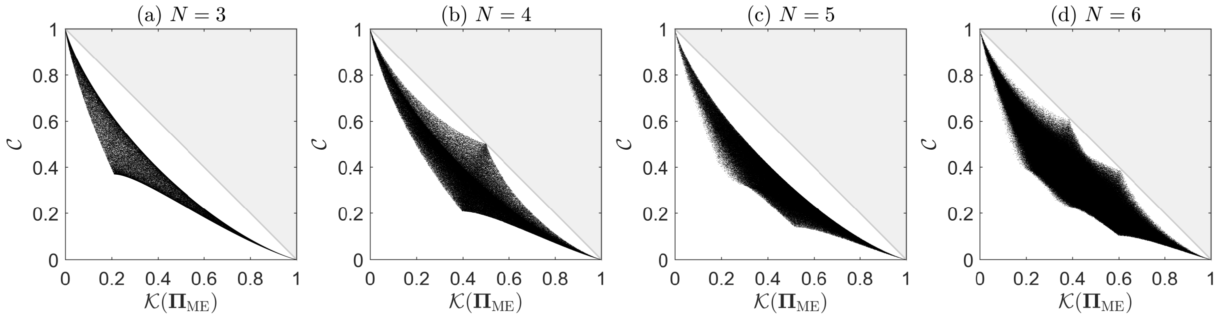

Figure 25 – Coherence vs which-path knowledge for uniform N-path interferometers with N-dimensional detector states discriminated via ME measurement. The simulations were performed with (a) 10^5, (b) 3×10^5, (c) 2.5×10^5, and (d) 3×10^6 randomly generated sets of detector states.

First, we consider the detector states discriminated via ME measurement ($\xi = 0$). In Fig. 25, we show the results for $N = 3, 4, 5, 6$, with $n = N$. In all cases, the scatter plots exhibit the resulting $(\mathcal{K}, \mathcal{C})$ points spanning a well-defined region—whose shape varies with N—within the bounds imposed by the duality relation. The boundaries of these regions exhibit cusps and inflection points. For $N = 4$ and $N = 6$, we observe cusps that touch the saturation line of the duality relation. This means that, beyond the trivial saturation points, namely $(1, 0)$ or $(0, 1)$, there also exist intermediate points where the relation is saturated for these values of N. In fact, this behavior was observed only for interferometers with a non-prime number of paths; the number of upward-pointing cusps and nontrivial saturation points corresponds to the number of proper divisors of N, excluding 1. As we shall discuss in detail in Sec. 5.4, these saturation points occur for uniform detector states embedded in n-dimensional subspaces, where n is a divisor of N in the range $1 < n < N$. It is important to emphasize that, in the results presented here, these saturation points are only approximately reached, since the randomly generated detector states are always linearly independent and have no vanishing components.

Still considering ME discrimination, in Fig. 26 we present results for a six-path interferometer with detector states lying in subspaces of dimension ranging from $n = 5$ to $n = 2$. A comparison with the plot in Fig. 25(d) shows that, for linearly dependent detector states, the region occupied by the $(\mathcal{C}, \mathcal{K})$ points becomes smaller as n decreases, due to the increasingly limited which-path knowledge.

We now assess the duality relation (5.27) in the case where which-path knowledge is obtained via standard FRIO discrimination of the detector states, using a fixed value of the separation parameter $\xi > 0$. In the first and third rows of Fig. 27, we plot $\mathcal{C}$ as a function of $\mathcal{K}(\mathbf{\Pi}_{\mathrm{FRIO}})$ for interferometers with $N = 3, 4, 5$ and 6 paths, where the quanton is coupled to an N-dimensional detector, and either $\xi = 0.6$ (first row) or $\xi = 1$ (third row) is used. To facilitate comparison with the ME case, we also plot the boundaries of the corresponding regions from

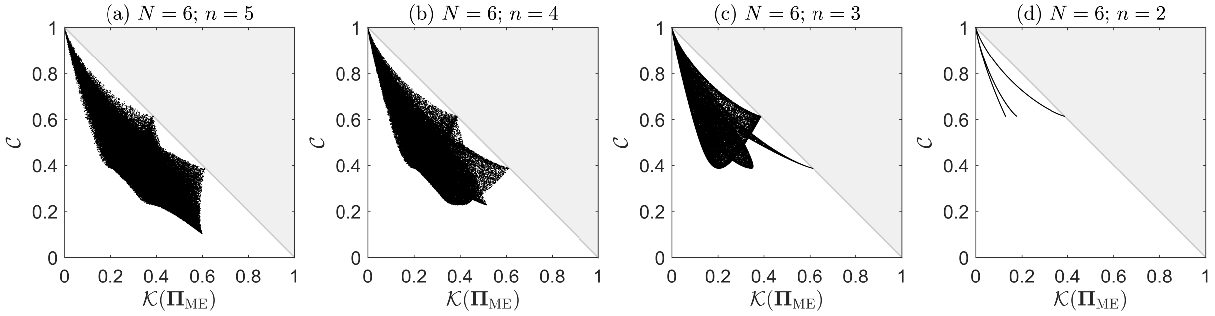

Figure 26 – Coherence vs which-path knowledge for uniform six-path interferometers with n-dimensional detector states discriminated via ME measurement. The simulations were performed with (a) 3×10^5, (b) 10^5, (c) 5×10^4, and (d) 10^4 randomly generated sets of detector states.

the $\mathcal{C}\times\mathcal{K}(\mathbf{\Pi}_{\text{ME}})$ diagrams shown in Fig. 25, as solid black lines.[3] For all values of N and ξ, the $(\mathcal{C},\mathcal{K})$ points obtained via standard FRIO now span a much broader region. Since the quanton's coherence is independent of the discrimination strategy applied to the detector states, this effect is entirely due to a decrease in the which-path knowledge,[4] which shifts these points from right to left within the region allowed by the duality relation. From Eq. (5.26), we see that this effect is driven by the success probability of state separation, $P_s(\xi)$, which modulates $\mathcal{K}(\mathbf{\Pi}_{\text{FRIO}})$. For instance, when the detector states have a very small coefficient a_{min}, both $P_s(\xi)$ [see Eq. (2.23)] and $\mathcal{K}(\mathbf{\Pi}_{\text{FRIO}})$ approach zero. This is illustrated in Fig. 28, where we generate 5×10^3 random detector states, each having at least one coefficient a_k ensured to be small. The plot also shows that, as ξ increases, the distribution of $(\mathcal{C},\mathcal{K})$ points moves further away from the saturation line. As in the two-path case, these features demonstrate that the bound in the duality relation is tighter for the ME measurement. Furthermore, for fixed N, the tightness of the bound decreases with increasing ξ.

5.3.3 Wave-particle duality with concatenated FRIO measurement

Here, we consider the case in which the detector states are discriminated using the concatenated FRIO measurement. As discussed in Sec. 2.5, this strategy is described by a $2N$-outcome POVM built from the detection operators defined in Eq. (2.39). Each half is associated with the probability distributions $\{p(j|\alpha_\ell)\}_{j=0}^{N-1}$ and $\{\tilde{p}(j|\alpha_\ell)\}_{j=0}^{N-1}$, which describe the conclusive identification of the input state conditioned on a successful or a failed separation, respectively.

---

[3] These boundaries were obtained using the *boundary* function in MATLAB, which computes a tight enclosing boundary around a set of points in 2D space. When the density of points near the boundary is low, the resulting curve tends to be less smooth, as observed for $N=5$ and, especially, for $N=6$.

[4] That is, $\mathcal{K}(\mathbf{\Pi}_{\text{FRIO}})\leq\mathcal{K}(\mathbf{\Pi}_{\text{ME}})$.

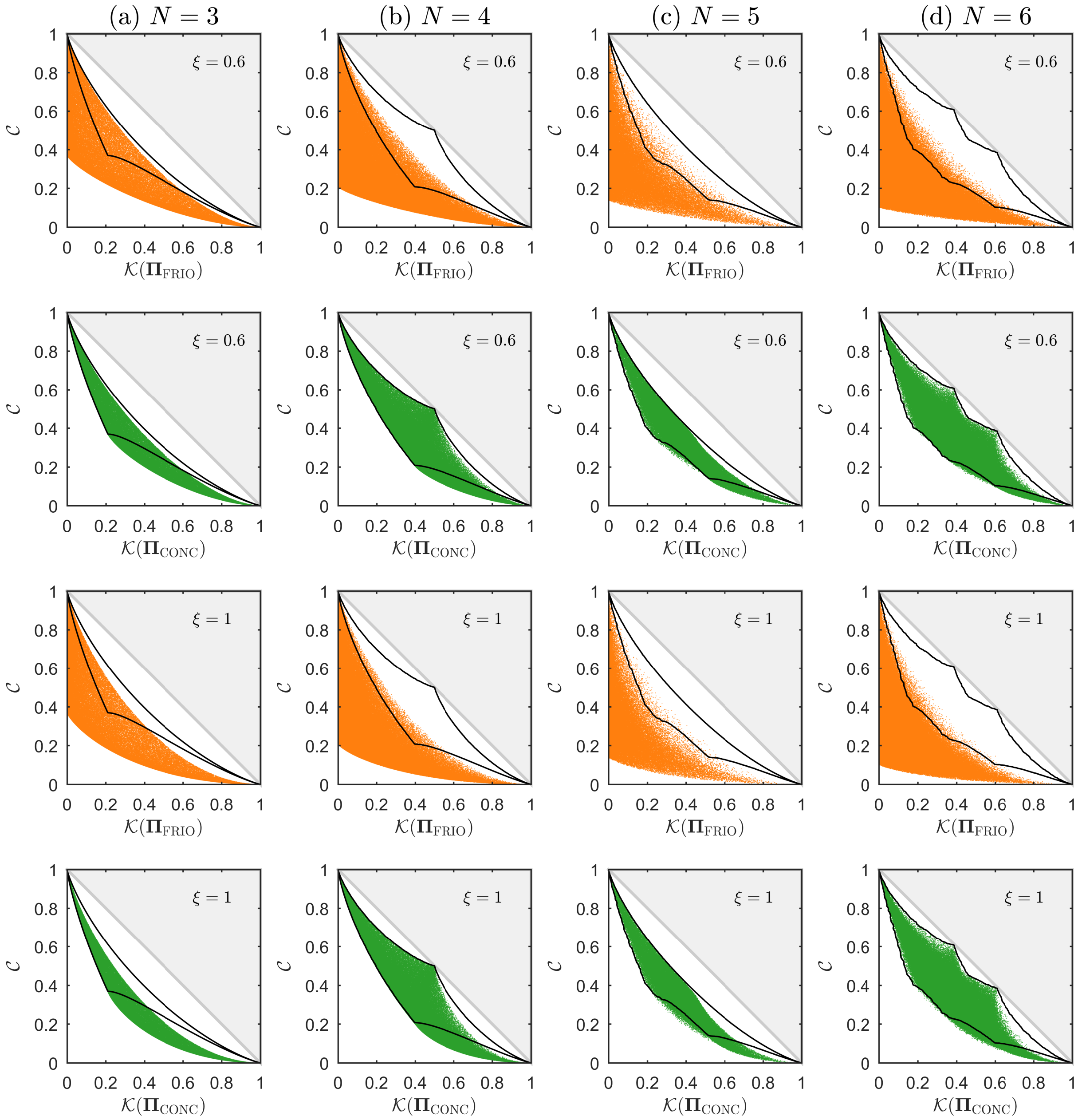

Figure 27 – Coherence vs which-path knowledge for uniform N-path interferometers with N-dimensional detector states discriminated via standard FRIO (first and third rows; orange dots) and concatenated FRIO (second and fourth rows; green dots), using the separation parameter ξ shown in the insets. The simulations were performed with (a) 10^5, (b) 3×10^5, (c) 10^5, and (d) 10^6 randomly generated sets of detector states. In each plot, the black solid line depicts the boundary of the corresponding region in the $\mathcal{C} \times \mathcal{K}(\mathbf{\Pi}_{\text{ME}})$ diagram shown in Fig. 25.

These distributions are given by

$$p(j|\alpha_\ell) = \langle\alpha_\ell|\hat{\Pi}_j(\xi)|\alpha_\ell\rangle = P_s(\xi)\langle\beta_\ell(\xi)|\hat{\Pi}_j^{\text{ME}}|\beta_\ell(\xi)\rangle, \tag{5.30}$$

$$\tilde{p}(j|\alpha_\ell) = \langle\alpha_\ell|\hat{\Pi}_j^f(\xi)|\alpha_\ell\rangle = P_f(\xi)\langle\tilde{\beta}_\ell(\xi)|\hat{\Pi}_j^{\text{ME}}|\tilde{\beta}_\ell(\xi)\rangle, \tag{5.31}$$

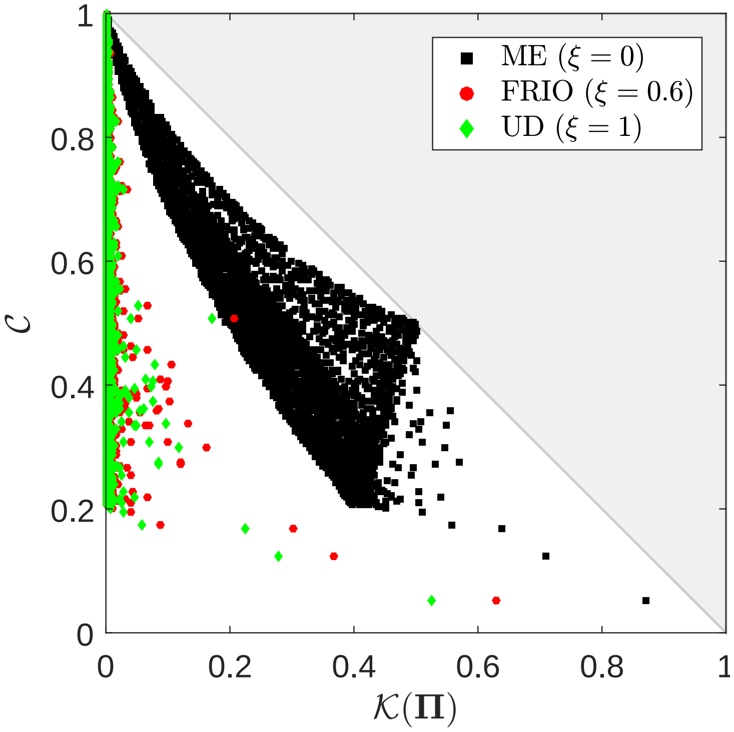

Figure 28 – Coherence vs which-path knowledge for uniform four-path interferometers with four-dimensional detector states discriminated via ME, FRIO, and UD measurements. The simulations were performed with 5×10^3 randomly generated sets of detector states, each having at least one coefficient ensured to be small.

where $P_s(\xi) = 1 - P_f(\xi)$, $|\beta_\ell(\xi)\rangle$, $|\tilde{\beta}_\ell(\xi)\rangle$, and $\hat{\Pi}_j^{\text{ME}}$ are defined in Eqs. (2.23), (2.21a), (2.21b), and (2.6), respectively.[5] The total probabilities of obtaining conclusive and inconclusive outcomes are given by $p_j = \frac{1}{N}\sum_{\ell=0}^{N-1} p(j|\alpha_\ell) = P_s(\xi)/N$ and $p_j^f = \frac{1}{N}\sum_{\ell=0}^{N-1} \tilde{p}(j|\alpha_\ell) = P_f(\xi)/N$. Therefore, the conditional probability distribution for the concatenated FRIO measurement reads

$$p(\alpha_\ell|j) = \langle\beta_\ell(\xi)|\hat{\Pi}_j^{\text{ME}}|\beta_\ell(\xi)\rangle \equiv \lambda_{j\ell}(\xi), \tag{5.32}$$

$$\tilde{p}(\alpha_\ell|j) = \langle\tilde{\beta}_\ell|\hat{\Pi}_j^{\text{ME}}|\tilde{\beta}_\ell\rangle \equiv \gamma_{j\ell}, \tag{5.33}$$

where $\gamma_{j\ell}$ is independent of the separation parameter ξ. By replacing this distribution into Eq. (5.14), and noting that $H(\{\gamma_{j\ell}\})$ is identical for all $j = 0, \ldots, N-1$, the which-path knowledge can be written as

$$\begin{aligned}\mathcal{K}(\mathbf{\Pi}_{\text{CONC}}) &= P_s(\xi)\left(1 - \frac{H(\{\lambda_{0\ell}(\xi)\})}{\log_2 N}\right) + P_f(\xi)\left(1 - \frac{H(\{\gamma_{0\ell}\})}{\log_2 N}\right)\\ &= \mathcal{K}(\mathbf{\Pi}_{\text{FRIO}}) + P_f(\xi)\left(1 - \frac{H(\{\gamma_{0\ell}\})}{\log_2 N}\right),\end{aligned} \tag{5.34}$$

---

[5] Note that $P_f(\xi) = Q(\xi)$ [see Eq. (2.32c)]. For the concatenated FRIO measurement, we use the notation $P_f(\xi)$ to emphasize that a failure in the separation process does not correspond to an inconclusive outcome in the discrimination stage, in contrast to the standard FRIO.

where we used Eq. (5.26). This expression shows that $\mathcal{K}(\mathbf{\Pi}_{\text{CONC}}) \geq \mathcal{K}(\mathbf{\Pi}_{\text{FRIO}})$. In fact, for a given set of detector states, we can establish the hierarchy

$$\mathcal{K}(\mathbf{\Pi}_{\text{FRIO}}) \leq \mathcal{K}(\mathbf{\Pi}_{\text{CONC}}) \leq \mathcal{K}(\mathbf{\Pi}_{\text{ME}}). \tag{5.35}$$

This hierarchy is expected, since the ME measurement yields the highest overall probability of correct identifications among these three discrimination strategies, followed by the concatenated and standard FRIO.

Finally, for the concatenated FRIO measurement, the duality relation (5.17) becomes

$$\begin{aligned} \mathcal{C} + \mathcal{K}(\mathbf{\Pi}_{\text{CONC}}) &= 1 - \frac{S(\hat{\rho})}{\log_2 N} + P_s(\xi)\left(1 - \frac{H(\{\lambda_{0\ell}(\xi)\})}{\log_2 N}\right) + P_f(\xi)\left(1 - \frac{H(\{\gamma_{0\ell}\})}{\log_2 N}\right) \\ &\leq 1. \end{aligned} \tag{5.36}$$

Numerical results and discussion

Like in the standard FRIO case, in the second and fourth rows of Fig. 27, we plot $\mathcal{C}$ as a function of $\mathcal{K}(\mathbf{\Pi}_{\text{CONC}})$ for interferometers with $N = 3, 4, 5$ and 6 paths, where the quanton is coupled to an N-dimensional detector, and either $\xi = 0.6$ (second row) or $\xi = 1$ (fourth row) is used. Again, the solid black lines represent the boundaries of the regions in the $\mathcal{C} \times \mathcal{K}(\mathbf{\Pi}_{\text{ME}})$ diagrams shown in Fig. 25. The regions spanned by the $(\mathcal{K}, \mathcal{C})$ points are now closer to those observed in the ME case; in particular, the cusps and nontrivial saturation points are recovered for interferometers with a non-prime number of paths. Note in the $\mathcal{C} \times \mathcal{K}(\mathbf{\Pi}_{\text{CONC}})$ diagrams that this proximity tends to be greater as the quanton's coherence increases or as ξ decreases. In both scenarios, the concatenated FRIO approaches the ME measurement. Increased coherence is associated with reduced distinguishability of the detector states $\{|\alpha_\ell\rangle\}$. In this case, the separation stage succeeds with low probability $P_s(\xi)$, and the resulting failure states are discriminated via ME with high probability $P_f(\xi) = 1 - P_s(\xi)$. On the other hand, as ξ decreases, the input states are separated with increasing success probability and undergo progressively smaller transformations before being discriminated via ME measurement.

As a consequence of these results, the bound in the duality relation is tighter for the concatenated FRIO compared to the standard FRIO. Moreover, the tightness decreases with increasing ξ, as can be seen in the diagrams of Fig. 27. In all cases, one observes a reduction in the region spanned by the $(\mathcal{K}, \mathcal{C})$ points and an approach to the saturation line.[6] This effect is driven by the second term on the right-hand side of Eq. (5.34), which, in comparison with $\mathcal{K}(\mathbf{\Pi}_{\text{FRIO}})$, is responsible for shifting these points in the opposite direction—from left to right.

---

[6] For a fixed $\xi > 0$, the approach to the saturation line do not occur only for $N = 3$. In this case, the detector states at the upper boundary of the region take the form $|\alpha_\ell\rangle = a_0|0\rangle + a_{\text{min}}\omega^\ell|1\rangle + a_{\text{min}}\omega^{2\ell}|2\rangle$, leading to identical failure states at the separation stage ($|\alpha_\ell\rangle \xrightarrow{\text{fail}} |0\rangle$ for all ℓ) and making concatenation ineffective.

In summary, corroborating the hierarchy established for which-path knowledge with respect to the discrimination strategies applied to the detector states [Eq. (5.35)], it is evident that the ME measurement yields the tightest bound in the duality relation, followed by the concatenated and standard FRIO measurements. Moreover, for both standard and concatenated FRIO, the tightness of the bound for fixed N decreases with increasing ξ, as shown in the diagrams of Fig. 27.

5.4 Saturating the duality relation in interferometers with non-prime number of paths

As stated above, the duality relation $\mathcal{C} + \mathcal{K}(\mathbf{\Pi}_{\text{ME}}) \leq 1$ for uniform N-path interferometers with symmetric detector states is saturated at nontrivial $(\mathcal{K}, \mathcal{C})$ points when the detector states are uniform and span an n-dimensional space, where n is a divisor of N in the range $1 < n < N$.[7] Thus, denoting by $\tau(N)$ the number of positive divisors of N, the number of nontrivial saturation points is given by $\sigma(N) = \tau(N) - 2$, which is consistent with the examples shown in Fig. 25. In this section, we provide a more detailed analysis of these aspects.

5.4.1 Qualitative analysis based on numerical simulations

Consider the duality relation in the case where the detector states are uniform, as defined in Eq. (2.7). In this scenario, both the standard and concatenated FRIO strategies reduce to the ME measurement, since no further separation is possible (see Sec. 2.4). For a fixed integer $n \leq N$, there are $\binom{N}{n}$ distinct n-dimensional subspaces generated by subsets of the orthonormal basis $\{|k\rangle\}_{k=0}^{N-1}$, and each of these subspaces supports a corresponding set of uniform symmetric states. To assess the duality relation for a given N-path interferometer in this case, we generate all $\binom{N}{n}$ sets of uniform n-dimensional detector states, for n ranging from 1 to N. From each set, we compute the quanton's coherence using Eq. (5.19) and the which-path knowledge using Eq. (5.28). The results obtained for $N = 12, 18,$ and 20 are shown in the $\mathcal{C} \times \mathcal{K}(\mathbf{\Pi}_{\text{ME}})$ diagrams of Fig. 29. For a given n, all sets of uniform detector state generate the same quanton's coherence[8]

$$\mathcal{C} = 1 - \frac{\log_2 n}{\log_2 N}. \tag{5.37}$$

This expression shows that, as n increases, coherence decreases. Therefore, in these diagrams, each set of $(\mathcal{K}, \mathcal{C})$ points with the same coherence corresponds, from top to bottom, to a value

---

[7] The trivial saturation points $(1, 0)$ and $(0, 1)$ are attained for uniform detector states in spaces of dimension $n = 1$ and $n = N$, respectively.

[8] In this case, the detector state in Eq. (5.10) is given by $\hat{\rho}_d = \frac{1}{n}\sum_{k\in\mathcal{I}} |k\rangle_d\langle k|$, where $|\mathcal{I}| = n$. Thus, for a given n, $S(\hat{\rho}_d)$—and consequently the coherence [Eq. (5.19)]—is the same for all $\hat{\rho}_d$, regardless of which n-dimensional subspace is considered.

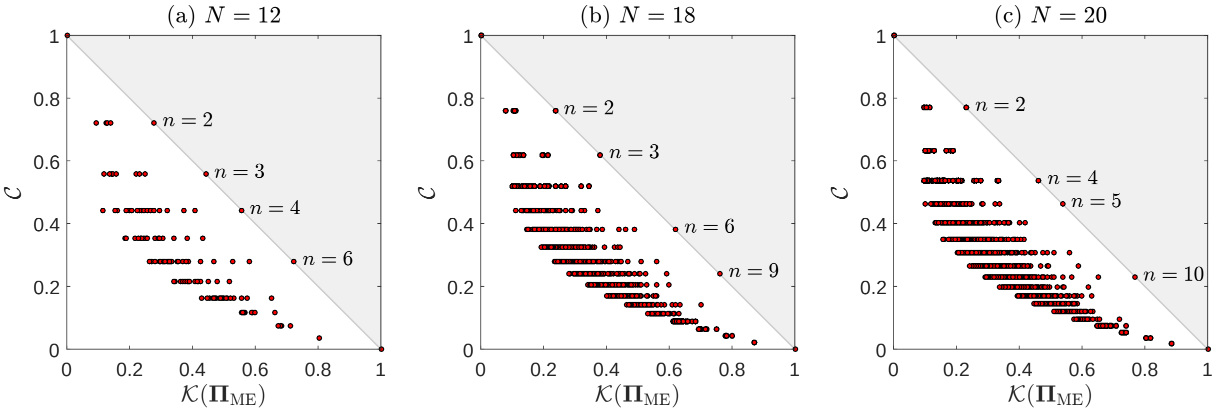

Figure 29 – Coherence vs which-path knowledge for uniform N-path interferometers with uniform n-dimensional detector states discriminated via ME measurement. From top to bottom, each set of points with same coherence corresponds to a value of n, ranging from 1 to N. The simulations were performed with all possible sets of uniform n-dimensional detector states and the insets show the values of n (beyond the trivial $n = 1$ and $n = N$) for which the duality relation is saturated.

of n ranging from 1 to N. In all cases, we have $\sigma(N) = 4$, as expected for the chosen values of N, with nontrivial saturation points occurring only at subspaces of the detector space whose dimensions are nontrivial divisors of N.

The diagrams of Fig. 29 also show that, among the $\binom{N}{n}$ sets of uniform n-dimensional detector states, many are physically equivalent or inequivalent, in the sense that they provide the same or different amounts of which-path knowledge, respectively, resulting in superimposed or displaced $(\mathcal{C}, \mathcal{K})$ points. For instance, for $n = N - 1$, all N sets of uniform states are physically equivalent, resulting in a single point in the diagram. On the other hand, both classes of detector states are present for all n in the range $1 < n < N - 1$.

In this analysis, we also extract the sets of detector states that lead to the saturation of the duality relation. The numerical results point that the states within a given set can be written as

$$|u_\ell^{m,\tau}\rangle = \frac{1}{\sqrt{N/m}} \sum_{k=0}^{N/m-1} \omega^{km\ell} |\tau \oplus km\rangle, \tag{5.38}$$

where m is an integer such that $N = nm$, $\tau \in \{0, 1, \ldots, m-1\}$, and $\oplus$ denotes addition modulo N; note that an irrelevant global phase factor, $\omega^{\tau\ell}$, has been discarded in this expression. For each $n = N/m$, there exist m physically equivalent sets that lead to saturation. Each set is labeled by τ and is defined in the n-dimensional subspace spanned by the basis vectors $\{|\tau \oplus km\rangle\}_{k=0}^{n-1}$, whose indices are equally spaced by m. As an example, consider $N = 6$. For $n = 2$, the sets $\{|u_\ell^{3,0}\rangle\}$, $\{|u_\ell^{3,1}\rangle\}$, and $\{|u_\ell^{3,2}\rangle\}$ lie in the subspaces spanned by $\{|0\rangle, |3\rangle\}$, $\{|1\rangle, |4\rangle\}$, and $\{|2\rangle, |5\rangle\}$, respectively. For $n = 3$, the sets $\{|u_\ell^{2,0}\rangle\}$ and $\{|u_\ell^{2,1}\rangle\}$ lie in the subspaces spanned by $\{|0\rangle, |2\rangle, |4\rangle\}$ and $\{|1\rangle, |3\rangle, |5\rangle\}$, respectively. Next, we provide a formal derivation of the results presented in this subsection.

5.4.2 Characterizing the saturating sets of detector states

In our interferometric scenario, the detector state defined in Eq. (5.10) becomes diagonal, i.e., $\hat{\rho}_d = \sum_{k\in\mathcal{I}} a_k^2 |k\rangle_d\langle k|$, leading to the quanton's coherence [Eq. (5.19)] $\mathcal{C} = 1 - H(\{a_k^2\})/\log_2 N$. From Eqs. (2.2), (2.6), and (5.24), the conditional probability distribution $\{\lambda_{0\ell}(0)\}$ for the ME measurement is given by

$$\lambda_{0\ell}(0) = \langle\alpha_\ell|\hat{\Pi}_0^{\mathrm{ME}}|\alpha_\ell\rangle = \frac{1}{N}\left|\sum_{k\in I} a_k\omega^{k\ell}\right|^2 \equiv |\lambda_\ell|^2. \tag{5.39}$$

Thus, the corresponding which-path knowledge [Eq. (5.28)] is written as $\mathcal{K}(\mathbf{\Pi}_{\mathrm{ME}}) = 1 - H(\{|\lambda_\ell|^2\})/\log_2 N$. The saturation of the duality relation, namely $\mathcal{C} + \mathcal{K}(\mathbf{\Pi}_{\mathrm{ME}}) = 1$, imposes the following condition on the Shannon entropies of the probability distributions $\{a_k^2\}$ and $\{|\lambda_\ell|^2\}$:

$$H(\{a_k^2\}) + H(\{|\lambda_\ell|^2\}) = \log_2 N. \tag{5.40}$$

We now demonstrate that this condition is satisfied if and only if the detector states are given by Eq. (5.38).

When the detector states are uniform, the probability distribution $\{a_k^2\}$ is uniform on its support $\mathcal{I}$ (i.e., $a_k^2 = 1/n$ for all $k \in \mathcal{I}$) and reaches the maximum entropy, $H(\{\frac{1}{n}\}) = \log_2 n$. From Eq. (5.40), this yields the following condition on the entropy $H(\{|\lambda_\ell|^2\})$:

$$H(\{|\lambda_\ell|^2\}) = -\sum_{\ell=0}^{N-1} |\lambda_\ell|^2 \log_2 |\lambda_\ell|^2 = \log_2 \frac{N}{n}. \tag{5.41}$$

This is the maximum entropy attained by $\{|\lambda_\ell|^2\}$ when it is uniform on a support of size $m = N/n$. Explicitly,

$$|\lambda_\ell|^2 = \begin{cases} \dfrac{n}{N}, & \text{for } \ell \in \mathcal{L} \subset \{0,\ldots,N-1\},\ |\mathcal{L}| = m, \\ 0, & \text{otherwise.} \end{cases} \tag{5.42}$$

It follows immediately from this result that saturation can only occur when n is a divisor of N, as stated earlier.

While the uniformity of the detector states is a necessary condition for saturating the duality relation, it is not sufficient. As shown in Fig. 29, not all sets of uniform states lead to saturation, and the numerical results point to a very specific form for the saturating states [Eq. (5.38)]. To understand this, consider the vectors $\{a_k\}$ and $\{\lambda_\ell\}$ in $\mathbb{C}^N$, which generate the corresponding probability distributions $\{a_k^2\}$ and $\{|\lambda_\ell|^2\}$. Let $\mathcal{I}$ and $\mathcal{L}$ denote the supports of these vectors, respectively. From Eq. (5.39), we have $\lambda_\ell = \frac{1}{\sqrt{N}}\sum_{k\in\mathcal{I}} a_k\omega^{k\ell}$, that is, the vector $\{\lambda_\ell\}$ is the discrete Fourier transform (DFT) of $\{a_k\}$. In this case, the discrete uncertainty principle[9] states that [124]

$$|\mathcal{I}|\cdot|\mathcal{L}| \geq N \quad\Rightarrow\quad |\mathcal{L}| \geq \frac{N}{n}, \tag{5.43}$$

where we used $|\mathcal{I}| = n$. As shown in Ref. [124], if N admits the factorization $N = nm$, then the lower bound $|\mathcal{L}| = m$ is attained by vectors $\{a_k\}$ of the form

$$a_k = \begin{cases} \dfrac{1}{\sqrt{n}}, & \text{if } k \in \{\tau\oplus\kappa m \mid \kappa = 0,\dots,n-1\}, \\ 0, & \text{otherwise,} \end{cases} \tag{5.44}$$

where $\tau \in \{0,\dots,m-1\}$ and $\oplus$ denotes addition modulo N. These are precisely the coefficient vectors corresponding to the fiducial states $|u_0^{m,\tau}\rangle$, from which the m sets of symmetric states defined in Eq. (5.38) are constructed. For vectors of this form, the corresponding probability distributions $\{|\lambda_\ell|^2\}$ satisfy Eq. (5.42), which ensures the saturation of the duality relation.[10] Therefore, we have demonstrated that the sets of uniform states $\{|u_\ell^{m,\tau}\rangle\}$, defined in Eq. (5.38), are indeed saturating sets. These are also the only ones with this property. For any other set of uniform or non-uniform detector states, the discrete uncertainty principle in Eq. (5.43) implies that $|\mathcal{L}| > N/n$. In such cases, the probability distribution $\{|\lambda_\ell|^2\}$ spreads over a larger support, and the corresponding increase in its entropy beyond $\log_2(N/n)$ prevents the saturation condition in Eq. (5.40) from being fulfilled.

Example: Four-path interferometers with two-dimensional detector states

To gain physical intuition about the above results, we analyze a uniform four-path interferometer with uniform two-dimensional detector states. Here, we have $\mathcal{C} = 1/2$, and the corresponding global quanton–detector state, obtained from Eqs. (2.7) and (5.6), is given by

$$|\Psi\rangle = \frac{1}{2}\sum_{\ell=0}^{3}|\ell\rangle_q|u_\ell\rangle_d = \frac{1}{2\sqrt{2}}\sum_{\ell=0}^{3}\sum_{k\in\mathcal{I}}\omega^{k\ell}|\ell\rangle_q|k\rangle_d. \tag{5.45}$$

---

[9] The discrete uncertainty principle for vectors related by a DFT states that if a vector of length N has n nonzero entries, then its DFT must have at least N/n nonzero entries. That is, a vector concentrated on a few components in one domain must be spread over many components in the Fourier-conjugate domain, which limits the simultaneous sparsity of a vector and its DFT. As an extreme example, if $a_k = \delta_{kk'}$, then $|\lambda_\ell| = 1/\sqrt{N}$ for all ℓ.

[10] The DFT of the vector $\{a_k\}$ defined in Eq. (5.44) is given by $\lambda_\ell = \frac{1}{\sqrt{Nn}}\sum_{\kappa=0}^{n-1}\omega^{(\tau\oplus\kappa m)\ell} = \frac{\omega^{\tau\ell}}{\sqrt{Nn}}\sum_{\kappa=0}^{n-1}\omega^{\kappa m\ell}$. The sum is a geometric series with ratio $r = \omega^{m\ell}$. Since $r^n = e^{2\pi i\ell} = 1$ for all $\ell \in \{0,\dots,N-1\}$, and $r = 1$ if and only if ℓ is a multiple of n, the sum equals n if $\ell \in \{0, n, 2n, \dots, (m-1)n\}$, and is zero otherwise. Substituting this into λ_ℓ and taking its modulus squared yields the probability distribution shown in Eq. (5.42).

First, we consider the support $\mathcal{I} = \{0, 2\}$, which corresponds to the saturating set defined in Eq. (5.38), in the subspace spanned by $\{|0\rangle_d, |2\rangle_d\}$. The detector states are given by

$$|u_0\rangle_d = |u_2\rangle_d = \frac{|0\rangle_d + |2\rangle_d}{\sqrt{2}} \equiv |+\rangle_d, \tag{5.46a}$$

$$|u_1\rangle_d = |u_3\rangle_d = \frac{|0\rangle_d - |2\rangle_d}{\sqrt{2}} \equiv |-\rangle_d, \tag{5.46b}$$

and thus the global state can be written as

$$|\Psi\rangle = \frac{1}{2}[(|0\rangle_q + |2\rangle_q)|+\rangle_d + (|1\rangle_q + |3\rangle_q)|-\rangle_d]. \tag{5.47}$$

Using Eq. (5.39), we obtain the probability distribution $\left(\frac{1}{2}, 0, \frac{1}{2}, 0\right)$ for $\{|\lambda_\ell|^2\}_{\ell=0}^3$, in agreement with Eq. (5.42). In this way, we have $\mathcal{K}(\mathbf{\Pi}_{\text{ME}}) = 1/2$, so that $\mathcal{C} + \mathcal{K}(\mathbf{\Pi}_{\text{ME}}) = 1$, as expected. The same results hold for $\mathcal{I} = \{1, 3\}$.

Now we consider the support $\mathcal{I} = \{0, 1\}$, which corresponds to a non-saturating set in the subspace spanned by $\{|0\rangle_d, |1\rangle_d\}$. In this case, the detector states are given by

$$|u_0\rangle_d = \frac{|0\rangle_d + |1\rangle_d}{\sqrt{2}} \equiv |+\rangle_d, \tag{5.48a}$$

$$|u_1\rangle_d = \frac{|0\rangle_d + i|1\rangle_d}{\sqrt{2}} \equiv |\imath_+\rangle_d, \tag{5.48b}$$

$$|u_2\rangle_d = \frac{|0\rangle_d - |1\rangle_d}{\sqrt{2}} \equiv |-\rangle_d, \tag{5.48c}$$

$$|u_3\rangle_d = \frac{|0\rangle_d - i|1\rangle_d}{\sqrt{2}} \equiv |\imath_-\rangle_d, \tag{5.48d}$$

which yields the global state

$$|\Psi\rangle = \frac{1}{2}(|0\rangle_q|+\rangle_d + |1\rangle_q|\imath_+\rangle_d + |2\rangle_q|-\rangle_d + |3\rangle_q|\imath_-\rangle_d). \tag{5.49}$$

From Eq. (5.39), we obtain the probability distribution $\left(\frac{1}{2}, \frac{1}{4}, 0, \frac{1}{4}\right)$ for $\{|\lambda_\ell|^2\}_{\ell=0}^3$, resulting in $\mathcal{K}(\mathbf{\Pi}_{\text{ME}}) = 1/4$. Thus, $\mathcal{C} + \mathcal{K}(\mathbf{\Pi}_{\text{ME}}) = 3/4 < 1$, and the relation is not saturated, as expected for this set of detector states. The same results hold for $\mathcal{I} = \{0, 3\}, \{1, 2\}$, and $\{2, 3\}$.

To better understand the results, we examine the quanton-detector states in each case. Equation (5.47) shows that the equally spaced structure of the support, such as $\mathcal{I} = \{0, 2\}$, allows the four paths to be grouped into pairs that are correlated with orthogonal detector states. Consequently, the ME measurement is performed on two states, such that each detector click eliminates two of the four possible paths, yielding the maximum which-path information allowed by the quanton's coherence. In contrast, when the support is unequally spaced, as in $\mathcal{I} = \{0, 1\}$, Eq. (5.49) shows that each path becomes correlated with a distinct detector state drawn from two mutually unbiased bases [Eqs. (5.48)]. As a result, the ME is performed on four states, with each detector click excluding only one of the four possible paths and thereby yielding less which-path information. This contrast highlights how the structure of the uniform detector states—specifically, the distribution of their relative phases, as determined by the choice of the support—affects the available which-path information. We expect that similar conclusions can be drawn by extending the present analysis to arbitrary non-prime values of N, with $n = N/m$.

5.5 Summary and outlook

In this chapter, we derived entropic wave-particle duality relations for a quanton tagged by symmetric which-way detector states in a uniform N-path interferometer. The wave- and particle-like properties were characterized by the normalized quanton's relative entropy of coherence ($\mathcal{C}$) and the mutual information obtained via detector-state discrimination $[\mathcal{K}(\mathbf{\Pi})]$, respectively. This interferometric configuration allowed us to apply the analytically solvable discrimination strategies presented in Chapter 2 and thus to obtain an exact quantification of which-path knowledge, rather than only upper bounds.

Using these exact quantifiers, we performed numerical simulations by generating large samples of random detector states and computing the corresponding values of $\mathcal{C}$ and $\mathcal{K}(\mathbf{\Pi})$ for ME, standard FRIO, and concatenated FRIO measurements. The resulting $\mathcal{C} \times \mathcal{K}(\mathbf{\Pi})$ diagrams provided several insights into the trade-off between these quantities, among which we highlight the following: (i) a clear observation that the ME measurement yields the tightest bound in the duality relation, followed by the concatenated and standard FRIO measurements; (ii) the close performance of the concatenated FRIO measurement relative to the ME measurement, and its advantage over the standard FRIO in terms of which-path information gain; (iii) the identification of nontrivial saturation points of the relation in interferometers with a non-prime number of paths. In the latter case, we explained this phenomenon by demonstrating that nontrivial saturation occurs only for uniform n-dimensional detector states with equally spaced support, where n is a nontrivial divisor of N.

The discussion of wave–particle duality dates back almost a century, yet it remains relevant, particularly in the context of duality relations in multipath interferometers. Our findings provide novel contributions to this topic and open avenues for experimental verification, as the discrimination strategies explored here have already been demonstrated in the laboratory.

6 Conclusion

In this thesis, we have explored the optimal discrimination of nonorthogonal quantum states from a theoretical, experimental, and foundational perspective. In particular, we addressed the optimal FRIO measurement (and its concatenated form) applied to distinguish between equally likely symmetric states, resulting in several advances in the field. On the theoretical side, we derived analytical solutions for the strategy. On the experimental side, we demonstrated the discrimination of up to seven nonorthogonal qubit states in a photonic setup. Finally, on the foundational side, we investigated the role of POVM-based coherence as a resource underlying both the standard and concatenated FRIO, and applied these strategies to derive new entropic wave-particle duality relations in multipath interferometers.

The results presented here not only deepen our understanding of quantum state discrimination but also open avenues for future research. From an experimental perspective, the standard FRIO measurement can be readily extended to qudits using our photonic setup, which would also allow for the implementation of the concatenated FRIO strategy. By exploiting the FRIO's ability to finely tune the balance between inconclusive and error rates, one can envision applying this setup to quantum communication protocols where trade-offs between efficiency and error tolerance play a crucial role. Another potential application involves using the randomness of the optimal FRIO measurement—as characterized by its associated POVM coherence—to develop high-dimensional quantum random number generators. This could be achieved by generalizing the approach of Ref. [55], which employs optimal UD of two states. Lastly, in the context of wave-particle duality relations, the results obtained in our specific scenario raise intriguing questions about the structure of detector states responsible for the saturation of the relation. A deeper understanding of these states may provide valuable insights into the form of the optimal measurement that achieves distinguishability.

Bibliography

[1] C. W. Helstrom, Detection theory and quantum mechanics, Inform. Control 10 (1967) 254. doi:10.1016/S0019-9958(67)90302-6.

[2] C. W. Helstrom, Detection theory and quantum mechanics (II), Inform. Control 13 (1968) 156. doi:10.1016/S0019-9958(68)90746-8.

[3] C. W. Helstrom, Quantum detection and estimation theory, J. Stat. Phys. 1 (1969) 231. doi:10.1007/BF01007479.

[4] N. Gisin, G. Ribordy, W. Tittel, H. Zbinden, Quantum cryptography, Rev. Mod. Phys. 74 (2002) 145. doi:10.1103/RevModPhys.74.145.

[5] S. M. Barnett, *Quantum Information*, Oxford University Press, Oxford, 2009.

[6] A. Chefles, Quantum state discrimination, Contemp. Phys. 41 (2000) 401. doi:10.1080/00107510010002599.

[7] J. Bae, L.-C. Kwek, Quantum state discrimination and its applications, J. Phys. A 48 (2015) 083001. doi:10.1088/1751-8113/48/8/083001.

[8] S. M. Barnett, S. Croke, Quantum state discrimination, Adv. Opt. Photon. 1 (2009) 238. doi:10.1364/AOP.1.000238.

[9] J. A. Bergou, Discrimination of quantum states, J. Mod. Opt. 57 (2010) 160. doi:10.1080/09500340903477756.

[10] C. W. Helstrom, *Quantum Detection and Estimation Theory*, Academic Press, New York, 1976.

[11] A. Holevo, Statistical decision theory for quantum systems, J. Multivariate Anal. 3 (1973) 337. doi:10.1016/0047-259X(73)90028-6.

[12] H. Yuen, R. Kennedy, M. Lax, Optimum testing of multiple hypotheses in quantum detection theory, IEEE Trans. Inf. Theory 21 (1975) 125. doi:10.1109/TIT.1975.1055351.

[13] I. Ivanovic, How to differentiate between non-orthogonal states, Phys. Lett. A 123 (1987) 257. doi:10.1016/0375-9601(87)90222-2.

[14] D. Dieks, Overlap and distinguishability of quantum states, Phys. Lett. A 126 (1988) 303. `doi:10.1016/0375-9601(88)90840-7`.

[15] A. Peres, How to differentiate between non-orthogonal states, Phys. Lett. A 128 (1988) 19. `doi:10.1016/0375-9601(88)91034-1`.

[16] G. Jaeger, A. Shimony, Optimal distinction between two non-orthogonal quantum states, Phys. Lett. A 197 (1995) 83. `doi:10.1016/0375-9601(94)00919-G`.

[17] A. Chefles, Unambiguous discrimination between linearly independent quantum states, Phys. Lett. A 239 (1998) 339. `doi:10.1016/S0375-9601(98)00064-4`.

[18] S. Croke, E. Andersson, S. M. Barnett, C. R. Gilson, J. Jeffers, Maximum confidence quantum measurements, Phys. Rev. Lett. 96 (2006) 070401. `doi:10.1103/PhysRevLett.96.070401`.

[19] A. Chefles, S. M. Barnett, Strategies for discriminating between non-orthogonal quantum states, J. Mod. Opt. 45 (1998) 1295. `doi:10.1080/09500349808230919`.

[20] C.-W. Zhang, C.-F. Li, G.-C. Guo, General strategies for discrimination of quantum states, Phys. Lett. A 261 (1999) 25. `doi:https://doi.org/10.1016/S0375-9601(99)00566-6`.

[21] E. Bagan, R. Muñoz Tapia, G. A. Olivares-Rentería, J. A. Bergou, Optimal discrimination of quantum states with a fixed rate of inconclusive outcomes, Phys. Rev. A 86 (2012) 040303. `doi:10.1103/PhysRevA.86.040303`.

[22] U. Herzog, Optimal state discrimination with a fixed rate of inconclusive results: Analytical solutions and relation to state discrimination with a fixed error rate, Phys. Rev. A 86 (2012) 032314. `doi:10.1103/PhysRevA.86.032314`.

[23] M. A. Solís-Prosser, A. Delgado, O. Jiménez, L. Neves, Parametric separation of symmetric pure quantum states, Phys. Rev. A 93 (2016) 012337. `doi:10.1103/PhysRevA.93.012337`.

[24] R. A. Kögler, L. Neves, Optimal probabilistic dense coding schemes, Quantum Inf. Process. 16 (2017) 92. `doi:10.1007/s11128-017-1545-7`.

[25] S. M. Barnett, E. Riis, Experimental demonstration of polarization discrimination at the Helstrom bound, J. Mod. Opt. 44 (1997) 1061. `doi:10.1080/09500349708230718`.

[26] R. Clarke, V. Kendon, A. Chefles, S. Barnett, E. Riis, M. Sasaki, Experimental realization of optimal detection strategies for overcomplete states, Phys. Rev. A 64 (2000) 012303. doi:10.1103/PhysRevA.64.012303.

[27] B. Huttner, A. Muller, J. D. Gautier, H. Zbinden, N. Gisin, Unambiguous quantum measurement of nonorthogonal states, Phys. Rev. A 54 (1996) 3783. doi:10.1103/PhysRevA.54.3783.

[28] R. B. M. Clarke, A. Chefles, S. M. Barnett, E. Riis, Experimental demonstration of optimal unambiguous state discrimination, Phys. Rev. A 63 (2001) 040305. doi:10.1103/PhysRevA.63.040305.

[29] P. J. Mosley, S. Croke, I. A. Walmsley, S. M. Barnett, Experimental realization of maximum confidence quantum state discrimination for the extraction of quantum information, Phys. Rev. Lett. 97 (2006) 193601. doi:10.1103/PhysRevLett.97.193601.

[30] M. A. Solís-Prosser, M. F. Fernandes, O. Jiménez, A. Delgado, L. Neves, Experimental minimum-error quantum-state discrimination in high dimensions, Phys. Rev. Lett. 118 (2017) 100501. doi:10.1103/PhysRevLett.118.100501.

[31] M. Mohseni, A. M. Steinberg, J. A. Bergou, Optical realization of optimal unambiguous discrimination for pure and mixed quantum states, Phys. Rev. Lett. 93 (2004) 200403. doi:10.1103/PhysRevLett.93.200403.

[32] M. Agnew, E. Bolduc, K. J. Resch, S. Franke-Arnold, J. Leach, Discriminating single-photon states unambiguously in high dimensions, Phys. Rev. Lett. 113 (2014) 020501. doi:10.1103/PhysRevLett.113.020501.

[33] S. Gómez, E. S. Gómez, O. Jiménez, A. Delgado, S. P. Walborn, G. Lima, Experimental quantum state discrimination using the optimal fixed rate of inconclusive outcomes strategy, Sci. Rep. 12 (2022) 17312. doi:10.1038/s41598-022-22314-w.

[34] L. F. Melo, M. A. Solís-Prosser, O. Jiménez, A. Delgado, L. Neves, Experimental optimal discrimination of N states of a qubit with fixed rates of inconclusive outcomes, Phys. Rev. Res. 5 (2023) 043149. doi:10.1103/PhysRevResearch.5.043149.

[35] A. Chefles, S. M. Barnett, Quantum state separation, unambiguous discrimination and exact cloning, J. Phys. A 31 (1998) 10097. doi:10.1088/0305-4470/31/50/007.

[36] O. Jiménez, X. Sánchez-Lozano, E. Burgos-Inostroza, A. Delgado, C. Saavedra, Experimental scheme for unambiguous discrimination of linearly independent symmetric states, Phys. Rev. A 76 (2007) 062107. doi:10.1103/PhysRevA.76.062107.

[37] O. Jiménez, M. A. Solís-Prosser, A. Delgado, L. Neves, Maximum-confidence discrimination among symmetric qudit states, Phys. Rev. A 84 (2011) 062315. doi:10.1103/PhysRevA.84.062315.

[38] K. Nakahira, T. S. Usuda, K. Kato, Discrimination between geometrically uniform quantum states with inconclusive results, Phys. Rev. A 86 (2012) 032316. doi:10.1103/PhysRevA.86.032316.

[39] L. Neves, M. A. Solís-Prosser, A. Delgado, O. Jiménez, Quantum teleportation via maximum-confidence quantum measurements, Phys. Rev. A 85 (2012) 062322. doi:10.1103/PhysRevA.85.062322.

[40] M. A. Solís-Prosser, A. Delgado, O. Jiménez, L. Neves, Deterministic and probabilistic entanglement swapping of nonmaximally entangled states assisted by optimal quantum state discrimination, Phys. Rev. A 89 (2014) 012337. doi:10.1103/PhysRevA.89.012337.

[41] M. A. Solís-Prosser, O. Jiménez, A. Delgado, L. Neves, Enhanced discrimination of high-dimensional quantum states by concatenated optimal measurement strategies, Quantum Sci. Technol. 7 (2022) 015017. doi:10.1088/2058-9565/ac37c4.

[42] M. Ban, K. Kurokawa, R. Momose, O. Hirota, Optimum measurements for discrimination among symmetric quantum states and parameter estimation, Int. J. Theor. Phys. 36 (1997) 1269. doi:10.1007/BF02435921.

[43] A. Chefles, S. M. Barnett, Optimum unambiguous discrimination between linearly independent symmetric states, Phys. Lett. A 250 (1998) 223. doi:10.1016/S0375-9601(98)00827-5.

[44] C. H. Bennett, Quantum cryptography using any two nonorthogonal states, Phys. Rev. Lett. 68 (1992) 3121. doi:10.1103/PhysRevLett.68.3121.

[45] S. J. D. Phoenix, S. M. Barnett, A. Chefles, Three-state quantum cryptography, J. Mod. Opt. 47 (2000) 507. doi:10.1080/09500340008244056.

[46] J. M. Renes, Spherical-code key-distribution protocols for qubits, Phys. Rev. A 70 (2004) 052314. doi:10.1103/PhysRevA.70.052314.

[47] A. Delgado, L. Roa, J. C. Retamal, C. Saavedra, Entanglement swapping via quantum state discrimination, Phys. Rev. A 71 (2005) 012303. `doi:10.1103/PhysRevA.71.012303`.

[48] L. Roa, A. Delgado, I. Fuentes-Guridi, Optimal conclusive teleportation of quantum states, Phys. Rev. A 68 (2003) 022310. `doi:10.1103/PhysRevA.68.022310`.

[49] A. Peres, *Quantum Theory: Concepts and Methods*, Springer, Dordrecht, 1995.

[50] M. A. Nielsen, I. L. Chuang, *Quantum Computation and Quantum Information*, Cambridge University Press, Cambridge, 2000.

[51] A. K. Pati, P. Parashar, P. Agrawal, Probabilistic superdense coding, Phys. Rev. A 72 (2005) 012329. `doi:10.1103/PhysRevA.72.012329`.

[52] S. Wu, S. M. Cohen, Y. Sun, R. B. Griffiths, Deterministic and unambiguous dense coding, Phys. Rev. A 73 (2006) 042311. `doi:10.1103/PhysRevA.73.042311`.

[53] K. Banaszek, Optimal quantum teleportation with an arbitrary pure state, Phys. Rev. A 62 (2000) 024301. `doi:10.1103/PhysRevA.62.024301`.

[54] G. Brassard, P. Horodecki, T. Mor, TelePOVM—a generalized quantum teleportation scheme, IBM J. Res. Dev. 48 (2004) 87. `doi:10.1147/rd.481.0087`.

[55] J. B. Brask, A. Martin, W. Esposito, R. Houlmann, J. Bowles, H. Zbinden, N. Brunner, Megahertz-rate semi-device-independent quantum random number generators based on unambiguous state discrimination, Phys. Rev. Appl. 7 (2017) 054018. `doi:10.1103/PhysRevApplied.7.054018`.

[56] A. Shehu, *Quantum state discrimination and quantum cloning: optimization and implementation*, Ph.D Thesis, Graduate Center, City University of New York, 2015.
URL `https://academicworks.cuny.edu/gc_etds/1126/`

[57] Y. Eldar, A. Megretski, G. Verghese, Designing optimal quantum detectors via semidefinite programming, IEEE Trans. Inf. Theory 49 (2003) 1007. `doi:10.1109/TIT.2003.809510`.

[58] Y. Eldar, A semidefinite programming approach to optimal unambiguous discrimination of quantum states, IEEE Trans. Inf. Theory 49 (2003) 446. `doi:10.1109/TIT.2002.807291`.

[59] Y. Feng, R. Duan, Z. Ji, Condition and capability of quantum state separation, Phys. Rev. A 72 (2005) 012313. `doi:10.1103/PhysRevA.72.012313`.

[60] V. Dunjko, E. Andersson, Transformations between symmetric sets of quantum states, J. Phys. A 45 (2012) 365304. `doi:10.1088/1751-8113/45/36/365304`.

[61] A. Peres, D. R. Terno, Optimal distinction between non-orthogonal quantum states, J. Phys. A 31 (1998) 7105. `doi:10.1088/0305-4470/31/34/013`.

[62] Y. Sun, M. Hillery, J. A. Bergou, Optimum unambiguous discrimination between linearly independent nonorthogonal quantum states and its optical realization, Phys. Rev. A 64 (2001) 022311. `doi:10.1103/PhysRevA.64.022311`.

[63] L. Roa, C. Hermann-Avigliano, R. Salazar, A. B. Klimov, Conclusive discrimination among N equidistant pure states, Phys. Rev. A 84 (2011) 014302. `doi:10.1103/PhysRevA.84.014302`.

[64] G. Zhang, L.-B. Yu, W.-H. Zhang, Z.-L. Cao, Extracting remaining information from an inconclusive result in optimal unambiguous state discrimination, Quantum Inf. Process. 13 (2014) 2619. `doi:10.1007/s11128-014-0817-8`.

[65] W.-H. Zhang, L.-L. Lin, K. Zhang, W.-Y. Nie, Revisiting unambiguous discrimination, Quantum Inf. Proccess. 21 (2022) 4. `doi:10.1007/s11128-021-03328-1`.

[66] D.-W. Guo, W.-H. Zhang, Unambiguous correct discrimination among symmetric qudit states, Quantum Inf. Proccess. 22 (2023) 172. `doi:10.1007/s11128-023-03923-4`.

[67] M. A. Solís-Prosser, A. Arias, J. J. M. Varga, L. Rebón, S. Ledesma, C. Iemmi, L. Neves, Preparing arbitrary pure states of spatial qudits with a single phase-only spatial light modulator, Opt. Lett. 38 (2013) 4762. `doi:10.1364/OL.38.004762`.

[68] J. J. M. Varga, L. Rebón, M. A. Solís-Prosser, L. Neves, S. Ledesma, C. Iemmi, Optimized generation of spatial qudits by using a pure phase spatial light modulator, J. Phys. B 47 (2014) 225504. `doi:10.1088/0953-4075/47/22/225504`.

[69] E. R. de Carvalho, *Caracterização de um dispositivo de cristal líquido para implementação de operações programáveis sobre o estado de polarização da luz*, Master's dissertation, Departamento de Física, Universidade Federal de Minas Gerais, 2024.
URL `http://hdl.handle.net/1843/77833`

[70] I. Moreno, P. Velásquez, C. R. Fernández-Pousa, M. M. Sánchez-López, F. Mateos, Jones matrix method for predicting and optimizing the optical modulation properties of a liquid-crystal display, J. Appl. Phys. 94 (2003) 3697. `doi:10.1063/1.1601688`.

[71] M. A. Solís-Prosser, L. Neves, Remote state preparation of spatial qubits, Phys. Rev. A 84 (2011) 012330. `doi:10.1103/PhysRevA.84.012330`.

[72] L. F. Melo, O. Jiménez, L. Neves, Coherence based on positive operator-valued measures for standard and concatenated quantum state discrimination with inconclusive results, Phys. Rev. A 111 (2025) 012403. `doi:10.1103/PhysRevA.111.012403`.

[73] C. H. Bennett, S. J. Wiesner, Communication via one- and two-particle operators on Einstein-Podolsky-Rosen states, Phys. Rev. Lett. 69 (1992) 2881. `doi:10.1103/PhysRevLett.69.2881`.

[74] C. H. Bennett, G. Brassard, C. Crépeau, R. Jozsa, A. Peres, W. K. Wootters, Teleporting an unknown quantum state via dual classical and Einstein-Podolsky-Rosen channels, Phys. Rev. Lett. 70 (1993) 1895. `doi:10.1103/PhysRevLett.70.1895`.

[75] B. Dakić, Y. O. Lipp, X. Ma, M. Ringbauer, S. Kropatschek, S. Barz, T. Paterek, V. Vedral, A. Zeilinger, Č. Brukner, et al., Quantum discord as resource for remote state preparation, Nature Phys. 8 (2012) 666. `doi:10.1038/nphys2377`.

[76] S. Pirandola, Quantum discord as a resource for quantum cryptography, Sci. Rep. 4 (2014) 6956. `doi:10.1038/srep06956`.

[77] A. Streltsov, G. Adesso, M. B. Plenio, Colloquium: Quantum coherence as a resource, Rev. Mod. Phys. 89 (2017) 041003. `doi:10.1103/RevModPhys.89.041003`.

[78] T. Baumgratz, M. Cramer, M. Plenio, Quantifying coherence, Phys. Rev. Lett. 113 (2013) 140401. `doi:10.1103/PhysRevLett.113.140401`.

[79] F. Bischof, H. Kampermann, D. Bruß, Resource theory of coherence based on positive-operator-valued measures, Phys. Rev. Lett. 123 (2019) 110402. `doi:10.1103/PhysRevLett.123.110402`.

[80] E. Chitambar, G. Gour, Quantum resource theories, Rev. Mod. Phys. 91 (2019) 025001. `doi:10.1103/RevModPhys.91.025001`.

[81] L. Roa, J. C. Retamal, M. Alid-Vaccarezza, Dissonance is required for assisted optimal state discrimination, Phys. Rev. Lett. 107 (2011) 080401. `doi:10.1103/PhysRevLett.107.080401`.

[82] F.-L. Zhang, J.-L. Chen, L. C. Kwek, V. Vedral, Requirement of dissonance in assisted optimal state discrimination, Sci. Rep. 3 (2013) 2134. `doi:10.1038/srep02134`.

[83] L. F. Xu, F. L. Zhang, M. L. Liang, J. L. Chen, Assisted optimal state discrimination without entanglement, Europhys. Lett. 106 (2014) 50004. `doi:10.1209/0295-5075/106/50004`.

[84] Z.-X. W. Bo Li, Shao-Ming Fei, H. Fan, Assisted state discrimination without entanglement, Phys. Rev. A 85 (2012) 022328. `doi:10.1103/PhysRevA.85.022328`.

[85] O. Jiménez, M. Solís-Prosser, L. Neves, A. Delgado, Quantum discord, thermal discord, and entropy generation in the minimum error discrimination strategy, Entropy 21 (2019) 263. `doi:10.3390/e21030263`.

[86] O. Jiménez, M. Solís-Prosser, L. Neves, A. Delgado, Mutual information and quantum discord in quantum state discrimination with a fixed rate of inconclusive outcomes, Entropy 23 (2021) 73. `doi:10.3390/e23010073`.

[87] M. Namkung, Y. Kwon, Understanding of various type of unambiguous discrimination in view of coherence distribution, Entropy 22 (2020) 1422. `doi:10.3390/e22121422`.

[88] S. Kim, L. Li, A. Kumar, X. Chunhe, S. Das, U. Sen, A. Pati, J. Wu, Protocol for unambiguous quantum state discrimination using quantum coherence, Quantum Inf. Comput. 21 (2021) 11. `doi:10.26421/QIC21.11-12-2`.

[89] O. Jiménez, M. A. Solís-Prosser, A. Delgado, L. Neves, Quantum resources for assisted optimal state discrimination, Phys. Rev. Res. 6 (2024) 043303. `doi:10.1103/PhysRevResearch.6.043303`.

[90] Y. Yao, X. Xiao, L. Ge, C. P. Sun, Quantum coherence in multipartite systems, Phys. Rev. A 92 (2015) 022112. `doi:10.1103/PhysRevA.92.022112`.

[91] X. Yuan, H. Zhou, Z. Cao, X. Ma, Intrinsic randomness as a measure of quantum coherence, Phys. Rev. A 92 (2015) 022124. `doi:10.1103/PhysRevA.92.022124`.

[92] X. Yuan, Q. Zhao, D. Girolami, X. Ma, Quantum coherence and intrinsic randomness, Adv. Quantum Technol. 2 (2019) 1900053. `doi:10.1002/qute.201900053`.

[93] F. Bischof, H. Kampermann, D. Bruß, Quantifying coherence with respect to general quantum measurements, Phys. Rev. A 103 (2021) 032429. `doi:10.1103/PhysRevA.103.032429`.

[94] J. Ma, A. Hakande, X. Yuan, X. Ma, Coherence as a resource for source-independent quantum random-number generation, Phys. Rev. A 99 (2019) 022328. `doi:10.1103/PhysRevA.99.022328`.

[95] J. Ma, Y. Zhou, X. Yuan, X. Ma, Operational interpretation of coherence in quantum key distribution, Phys. Rev. A 99 (2019) 062325. `doi:10.1103/PhysRevA.99.062325`.

[96] J. Åberg, Quantifying superposition, arXiv:quant-ph/0612146 (2007).

[97] T. Theurer, N. Killoran, D. Egloff, M. B. Plenio, Resource theory of superposition, Phys. Rev. Lett. 119 (2017) 230401. `doi:10.1103/PhysRevLett.119.230401`.

[98] B. Groisman, S. Popescu, A. Winter, Quantum, classical, and total amount of correlations in a quantum state, Phys. Rev. A 72 (2005) 032317. `doi:10.1103/PhysRevA.72.032317`.

[99] E. Bagan, J. A. Bergou, S. S. Cottrell, M. Hillery, Relations between coherence and path information, Phys. Rev. Lett. 116 (2016) 160406. `doi:10.1103/PhysRevLett.116.160406`.

[100] N. Bohr, in: P. A. Schilpp (Ed.), *Albert Einstein: Philosopher-Scientist*, Library of Living Philosophers, Evanston, 1949, pp. 200–241.

[101] N. Bohr, The quantum postulate and the recent development of atomic theory, Nature 121 (1928) 580. `doi:10.1038/121580a0`.

[102] R. P. Feynman, R. B. Leighton, M. Sands, *The Feynman Lectures on Physics*, Vol. III: Quantum Mechanics, New Millennium Edition, Basic Books, 2011, (Originally published in 1965).

[103] W. K. Wootters, W. H. Zurek, Complementarity in the double-slit experiment: Quantum nonseparability and a quantitative statement of Bohr's principle, Phys. Rev. D 19 (1979) 473. `doi:10.1103/PhysRevD.19.473`.

[104] H. Rauch, J. Summhammer, Static versus time-dependent absorption in neutron interferometry, Phys. Lett. A 104 (1984) 44. `doi:https://doi.org/10.1016/0375-9601(84)90586-3`.

[105] A. Zeilinger, Complementarity in neutron interferometry, Physica B+C 137 (1986) 235. `doi:https://doi.org/10.1016/0378-4363(86)90328-1`.

[106] P. Mittelstaedt, A. Prieur, R. Schieder, Unsharp particle-wave duality in a photon split-beam experiment, Found. Phys. 17 (1987) 891. doi:10.1007/BF00734319.

[107] D. M. Greenberger, A. Yasin, Simultaneous wave and particle knowledge in a neutron interferometer, Phys. Lett. A 128 (1988) 391. doi:https://doi.org/10.1016/0375-9601(88)90114-4.

[108] L. Mandel, Coherence and indistinguishability, Opt. Lett. 16 (1991) 1882. doi:10.1364/OL.16.001882.

[109] G. Jaeger, A. Shimony, L. Vaidman, Two interferometric complementarities, Phys. Rev. A 51 (1995) 54. doi:10.1103/PhysRevA.51.54.

[110] B.-G. Englert, Fringe visibility and which-way information: An inequality, Phys. Rev. Lett. 77 (1996) 2154. doi:10.1103/PhysRevLett.77.2154.

[111] P. D. D. Schwindt, P. G. Kwiat, B.-G. Englert, Quantitative wave-particle duality and nonerasing quantum erasure, Phys. Rev. A 60 (1999) 4285. doi:10.1103/PhysRevA.60.4285.

[112] B.-G. Englert, J. A. Bergou, Quantitative quantum erasure, Opt. Commun. 179 (2000) 337. doi:https://doi.org/10.1016/S0030-4018(99)00718-X.

[113] S. Dürr, Quantitative wave-particle duality in multibeam interferometers, Phys. Rev. A 64 (2001) 042113. doi:10.1103/PhysRevA.64.042113.

[114] G. Bimonte, R. Musto, Comment on “Quantitative wave-particle duality in multibeam interferometers”, Phys. Rev. A 67 (2003) 066101. doi:10.1103/PhysRevA.67.066101.

[115] G. Bimonte, R. Musto, On interferometric duality in multibeam experiments, J. Phys. A 36 (2003) 11481. doi:10.1088/0305-4470/36/45/009.

[116] B.-G. Englert, D. Kaszlikowski, L. C. Kwek, W. H. Chee, Wave-particle duality in multi-path interferometers: General concepts and three-path interferometers, Int. J. Quantum Inf. 06 (2008) 129. doi:10.1142/S0219749908003220.

[117] M. N. Bera, T. Qureshi, M. A. Siddiqui, A. K. Pati, Duality of quantum coherence and path distinguishability, Phys. Rev. A 92 (2015) 012118. doi:10.1103/PhysRevA.92.012118.

[118] T. Qureshi, M. A. Siddiqui, Wave–particle duality in N-path interference, Ann. Phys. 385 (2017) 598. doi:https://doi.org/10.1016/j.aop.2017.08.015.

[119] E. Bagan, J. A. Bergou, M. Hillery, Wave-particle-duality relations based on entropic bounds for which-way information, Phys. Rev. A 102 (2020) 022224. doi:10.1103/PhysRevA.102.022224.

[120] J. Bergou, M. Hillery, M. Saffman, *Quantum Information Processing: Theory and Implementation*, 2nd Edition, Springer, 2021.

[121] P. Hausladen, R. Jozsa, B. Schumacher, M. Westmoreland, W. K. Wootters, Classical information capacity of a quantum channel, Phys. Rev. A 54 (1996) 1869. doi:10.1103/PhysRevA.54.1869.

[122] P. Hausladen, W. K. W. and, A 'pretty good' measurement for distinguishing quantum states, Journal of Modern Optics 41 (12) (1994) 2385–2390. doi:10.1080/09500349414552221.

[123] A. Varga, P. Adam, J. A. Bergou, Maximum information measurement for qubit states, Sci. Rep. 14 (2024) 11888. doi:10.1038/s41598-024-62446-9.

[124] D. L. Donoho, P. B. Stark, Uncertainty principles and signal recovery, SIAM J. Appl. Math. 49 (1989) 906. doi:10.1137/0149053.

[125] A. Márquez, I. Moreno, C. Iemmi, A. Lizana, J. Campos, M. J. Yzuel, Mueller-stokes characterization and optimization of a liquid crystal on silicon display showing depolarization, Opt. Express 16 (2008) 1669. doi:10.1364/OE.16.001669.

Appendix

APPENDIX A - FRIO optimization for two pure states via Lagrange multipliers

Following the approach of Ref. [56], for the optimization problem of minimizing $P_e = \eta_0 r_0 + \eta_1 r_1$ under the constraints that $Q = \eta_0 q_0 + \eta_1 q_1$ is fixed and the overlap obeys Eq. (1.31), we address the Lagrange multipliers method. Consider the function

$$\begin{aligned}\mathcal{Q} = \eta_0 r_0 + \eta_1 r_1 + \lambda \left[\alpha - \sqrt{(1-r_0-q_0)r_1} + \sqrt{(1-r_1-q_1)r_0} + \sqrt{q_0 q_1}\right] \\ + \mu \left[\eta_0 q_0 + \eta_1 q_1 - Q\right],\end{aligned} \tag{1}$$

where λ and μ are Lagrange multipliers. The partial derivatives $\partial Q/\partial r_j$ yield:

$$\frac{\partial \mathcal{Q}}{\partial r_0} = \eta_0 + \frac{\lambda}{2}\left(\sqrt{\frac{r_1}{1-r_0-q_0}} - \sqrt{\frac{1-r_1-q_1}{r_0}}\right) = 0, \tag{2a}$$

$$\frac{\partial \mathcal{Q}}{\partial r_1} = \eta_1 + \frac{\lambda}{2}\left(\sqrt{\frac{r_0}{1-r_1-q_1}} - \sqrt{\frac{1-r_0-q_0}{r_1}}\right) = 0. \tag{2b}$$

The equations in r_0, r_1 indicate that

$$2\eta_i\sqrt{r_i(1-r_i-q_i)} = \lambda\left[\sqrt{(1-r_0-q_0)(1-r_1-q_1)} - \sqrt{r_0 r_1}\right] \equiv D, \tag{3}$$

where D is a constant. For the partial derivatives $\partial Q/\partial q_j$, we find

$$\frac{\partial \mathcal{Q}}{\partial q_0} = \frac{\lambda}{2}\left(\sqrt{\frac{r_1}{1-r_0-q_0}} - \sqrt{\frac{q_1}{q_0}}\right) + \mu\eta_0 = 0, \tag{4a}$$

$$\frac{\partial \mathcal{Q}}{\partial q_1} = \frac{\lambda}{2}\left(\sqrt{\frac{r_0}{1-r_1-q_1}} - \sqrt{\frac{q_0}{q_1}}\right) + \mu\eta_1 = 0, \tag{4b}$$

which we can rewrite as

$$\frac{\lambda}{2}\left(\sqrt{r_0 r_1} - \sqrt{\frac{q_1}{q_0}}\sqrt{r_0(1-r_0-q_0)}\right) + \mu\eta_0\sqrt{r_0(1-r_0-q_0)} = 0, \tag{5a}$$

$$\frac{\lambda}{2}\left(\sqrt{r_0 r_1} - \sqrt{\frac{q_0}{q_1}}\sqrt{r_1(1-r_1-q_1)}\right) + \mu\eta_1\sqrt{r_1(1-r_1-q_1)} = 0. \tag{5b}$$

Note that because of relation (3), we conclude that $\eta_0 q_0 = \eta_1 q_1$, yielding solutions

$$q_i = \frac{Q}{2\eta_i}, \tag{6}$$

which is the individual inconclusive rates shown in Eq. (1.32a). The solution to the second-order equation (3) gives

$$r_i = \frac{1}{2}\left[(1-q_i) - C_i\right], \tag{7}$$

where

$$C_i = \sqrt{(1-q_i)^2 - \frac{D^2}{\eta_i^2}}. \tag{8}$$

By substituting solution (7) into the constraint (1.31), it is easy to show that

$$2(\alpha - \sqrt{q_0 q_1})^2 = (1-q_0)(1-q_1) - C_0 C_1 + \frac{D^2}{\eta_0 \eta_1}. \tag{9}$$

Isolating the term C_0C_1 in Eq. (9), squaring both sides of the resulting expression, and using Eq. (8), we obtain, after some algebra

$$D^2 = \frac{4\eta_0^2\eta_1^2\left[(1-q_0)(1-q_1) - (\alpha - \sqrt{q_0q_1})^2\right]}{(1-Q)^2 - 4\eta_0\eta_1(\alpha - \sqrt{q_0q_1})^2}. \tag{10}$$

Then, by substituting Eq. (10) into Eq. (8), it can be shown that

$$C_i^2 = \frac{\left[(1-q_i)(1-Q) - 2(1-\eta_i)(\alpha - \sqrt{q_0q_1})^2\right]^2}{(1-Q)^2 - 4\eta_0\eta_1(\alpha - \sqrt{q_0q_1})^2}. \tag{11}$$

By substituting the above equation into Eq. (7), we find the individual error probabilities to be

$$r_i = \frac{1}{2}\left\{(1-q_i) - \frac{\left[(1-q_i)(1-Q) - 2(1-\eta_i)(\alpha - \sqrt{q_0q_1})^2\right]}{\sqrt{(1-Q)^2 - 4\eta_0\eta_1(\alpha - \sqrt{q_0q_1})^2}}\right\}, \tag{12}$$

which, using $\bar{Q} = 1 - Q$ and Eq. (1.26), corresponds to Eq. (1.32b). Finally, using Eqs. (12), we obtain the minimum error probability for a fixed Q, as

$$P_e^{\min}(Q) = \frac{1}{2}\left[\bar{Q} - \sqrt{\bar{Q}^2 - (Q_0 - Q)^2}\right], \tag{13}$$

where we used relation $2\sqrt{\eta_0 q_0 \eta_1 q_1} = Q$ [see Eq. (6)].

APPENDIX B - Analyzing input–output overlaps in quantum state separation

The magnitudes of the overlaps between distinct pairs of states within the input set $\{|\alpha_j\rangle\}$ [Eq. (2.2)] and within the uniform set $\{|u_j\rangle\}$ [Eq. (2.7)] are given by

$$\alpha \equiv |\langle\alpha_i|\alpha_j\rangle| = \left|\sum_{k\in\mathcal{I}} a_k^2 \omega^{k\ell}\right|, \tag{14}$$

$$u \equiv |\langle u_i|u_j\rangle| = \left|\frac{1}{n}\sum_{k\in\mathcal{I}} \omega^{k\ell}\right|, \tag{15}$$

where $\ell = j - i \neq 0$. Thus, using these results and Eqs. (2.21a) and (2.22a), the magnitude of the overlap between distinct pairs of states in the successfully transformed output set $\{|\beta_j(\xi)\rangle\}$ will be given by

$$\beta(\xi) \equiv |\langle\beta_i(\xi)|\beta_j(\xi)\rangle| = |(1-\xi)z_\alpha + \xi z_u|\,, \tag{16}$$

where $z_\alpha = \langle\alpha_i|\alpha_j\rangle$ and $z_u = \langle u_i|u_j\rangle$. By applying the convexity of the modulus and noting that $\alpha > u$, we obtain[1]

$$\begin{aligned} \beta(\xi) &= |(1-\xi)z_\alpha + \xi z_u| \\ &\leq (1-\xi)\alpha + \xi u \\ &\leq \alpha, \end{aligned} \tag{17}$$

where the equality holds for $\xi = 0$. For $\xi > 0$, the inequality $\beta(\xi) < \alpha$ implies that the states in $\{|\beta_j(\xi)\rangle\}$ are more distinguishable than those in $\{|\alpha_j\rangle\}$.

It is easy to see from Eq. (17) that $\beta(0) = \alpha$ (no separation) and $\beta(1) = u$ (maximum separation). To analyze the behavior of $\beta(\xi)$ on the interval $\xi \in [0,1]$, let us write $f(\xi) = (1-\xi)z_\alpha + \xi z_u$. Then $\beta(\xi) = |f(\xi)|$ corresponds to the norm of a convex combination of the vectors z_α and z_u in the complex plane. The condition $\alpha > u$ (which arises from $a_k^2 \neq 1/n$ for at least one $k \in \mathcal{I}$) implies that $z_\alpha \not\propto z_u$, i.e., these vectors are not aligned, and therefore $f(\xi)$ traces the straight-line segment connecting z_α to z_u. As ξ increases from 0 to 1, the norm of $f(\xi)$ decreases monotonically from α to u. Thus, $\beta(\xi)$ is a decreasing function on the interval $\xi \in [0,1]$, meaning that the successfully separated states become more distinguishable as ξ increases.

---

[1] When $a_k^2 = 1/n$ for all $k \in \mathcal{I}$, we have $\alpha = u$. This case can be excluded because it corresponds to a scenario where no further separation of the input states is possible.

On the other hand, using Eqs. (2.21b) and (2.22b), we find the magnitude of the overlap between distinct pair of states in the failure output set $\{|\tilde{\beta}_j\rangle\}$ to be

$$\tilde{\beta} \equiv |\langle\tilde{\beta}_i|\tilde{\beta}_j\rangle| = \frac{|z_\alpha - na^2_{\text{min}} z_u|}{1 - na^2_{\text{min}}}. \tag{18}$$

Using the reverse triangle inequality, and the fact that $u/\alpha < 1$, we obtain

$$\begin{aligned}\tilde{\beta} &\geq \frac{|\alpha - na^2_{\text{min}} u|}{1 - na^2_{\text{min}}} \\ &> \alpha.\end{aligned} \tag{19}$$

Therefore, when the separation fails, the output states become less distinguishable than the inputs.

APPENDIX C - Calibration and configuration of the SLM for state separation

In order to characterize the optical modulation properties of the transmissive LCD used in the state separation stage, we resort to the standard approach developed by Moreno *et al.* [70]. First, to characterize the polarization modulation, the LCD is sandwiched by a polarization state generator (PG) and polarization analyzer (PA), the former composed of a linear polarizer followed by a quarter-wave plate (QWP) and the later of a QWP followed by a linear polarizer. With this arrangement, we measure the light intensities as a function of the gray level addressed to the display by preparing and analyzing the polarization in the bases $\{\mathsf{h}, \mathsf{v}\}$, $\{\pm 45^\circ\}$ and $\{\mathsf{R}, \mathsf{L}\}$, which generates 36 measurements,[2] each one for $\mathsf{gl} = 0, \ldots, 255$. Second, to characterize the phase modulation, we remove both PG and PA and illuminate each half of the LCD with a small vertically polarized beam generated by a double pinhole. This double beam is made to interfere at the focal plane of a spherical lens at the vertical output of a PBS, where the intensity pattern is recorded by a CMOS camera. By keeping the gray level at the left half of the LCD equal zero while changing it at the right half, we record 256 interference patterns.

The SLM is built by sandwiching the LCD between a HWP+QWP (before) and QWP+HWP (after) with fixed orientations. With the dataset from the LCD characterization outlined above we can predict the configurations of the wave plates to obtain the desired light modulation. In our case, the imposed constraints were twofold: first, a vertically polarized light passing through the SLM must not suffer any net rotation for $\mathsf{gl} = 0$ at the LCD and its intensity must decrease monotonically as gl increases; second, the phase shift introduced by the SLM as a function of gl must be equal at both outputs of a PBS. We made a numerical search for the configuration of the wave plates satisfying these constraints and found that only the HWPs were required before and after the LCD [see Fig. 12(a)] oriented at 28° and 29° from the vertical axis, respectively. The resulting modulation properties of this configuration are described in Appendix 6.

---

[2] In the master's dissertation of Erick R. de Carvalho [69], the reader can find a complete characterization of the polarization modulation properties of our LCD, using both the Mueller matrix and quantum operations formalisms.

APPENDIX D - Target separation angles and phase shifts on the LCD

In Sec. 3.1.2, it was shown that to perform the optimal state separation on the path-encoded symmetric states, the programmable SLM must, for a given gray level at the LCD, add a phase shift φ in the mode $|0\rangle$ and rotate its polarization according to Eq. (3.4). The parameter $\zeta(\theta') = \tan\theta \cot\theta'$ [see Eq. (3.2)] sets the relationship between the input and output separation angles (θ and θ', respectively) with the required rotation of the ancilla to achieve that separation. Based on this, we can obtain the target output separation angles as a function of the gray level, namely $\theta'(\mathsf{gl})$. From Eq. (3.4) we have

$$\zeta^2(\theta') = |\langle \mathsf{v}|\mathsf{p}(\theta')\rangle|^2 \equiv P_{\mathsf{v}}, \tag{20}$$

which is the probability of projecting the rotated ancilla onto the vertical polarization. The SLM is configured to implement this transformation as close as possible: unwanted effects such as depolarization [69, 125] prevents it from working exactly as we wish. In a simple model, this means that an input vertically polarized beam is actually transformed as

$$|\mathsf{v}\rangle \to \hat{\rho}(\mathsf{gl}) = (1 - \epsilon(\mathsf{gl}))|\mathsf{p}(\theta')\rangle\langle \mathsf{p}(\theta')| + \epsilon(\mathsf{gl})\frac{\hat{I}}{2}, \tag{21}$$

with a desirable $\epsilon(\mathsf{gl}) \to 0$ for $\mathsf{gl} = 0, \ldots, 255$. With this configuration we can extract $P_{\mathsf{v}}(\mathsf{gl}) = \langle \mathsf{v}|\hat{\rho}(\mathsf{gl})|\mathsf{v}\rangle$ (see the appendix of Ref. [41]) and, assuming that the SLM implements the exact rotation, we obtain

$$\theta'(\mathsf{gl}) = \arctan\left[\frac{\tan\theta}{\sqrt{P_{\mathsf{v}}(\mathsf{gl})}}\right]. \tag{22}$$

In Fig. 30(a), we plot $\theta'(\mathsf{gl})$ for different values of the input angle, $\theta = \theta'(0)$. For $\theta < 19.5^\circ$ (red dash-dotted curves), the accessible θ''s get below 45°, which makes it impossible to achieve maximum state separation. In this case, although FRIO could be implemented, we would not reach the MC measurement. On the other hand, for $\theta > 19.5^\circ$ (black dashed curves), although θ' reaches 45°, the accessible angles vary within decreasing ranges. The best scenario to overcome these issues is provided by the input $\theta = 19.5^\circ$, shown in the black solid curve, where the red markers "$\times$" indicate the target separation angles $\{\theta'_t\}_{t=1}^{7}$ (note that $\theta'_1 = \theta$). For this reason, we have implemented the optimal FRIO measurement starting with symmetric states with $\theta = 19.5^\circ$. Figure 30(b) shows the phase shift imprinted by the SLM as a function of the gray level on the LCD, obtained through interferometric measurements [70]. The red markers "$\times$" indicate the phases $\{\varphi_t\}_{t=1}^{7}$ corresponding to the gray levels used to achieve the target separation angles. The values of θ'_t and φ_t used in our experiment are also given in Table 1.

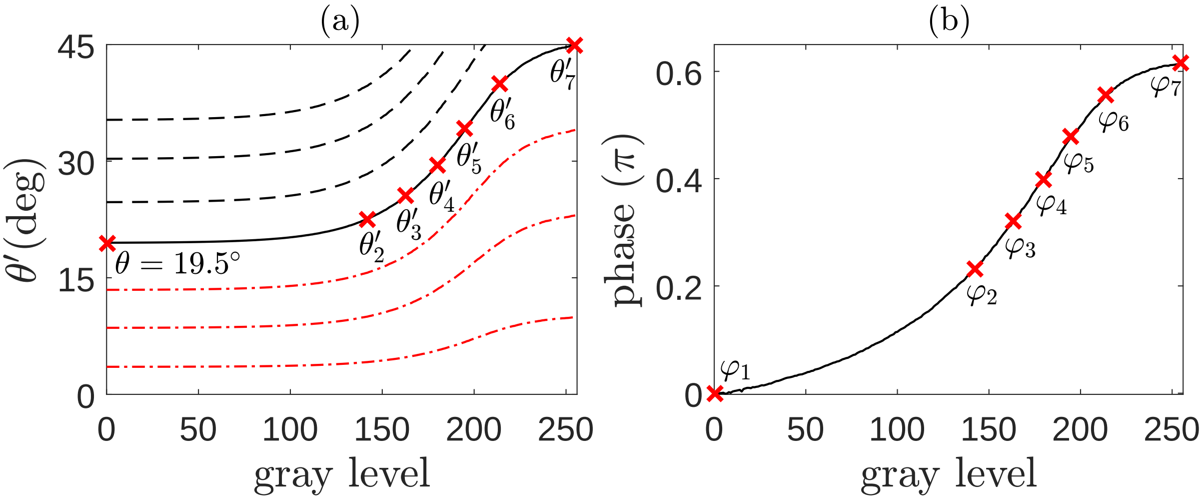

Figure 30 – (a) Target separation angle and (b) phase shift as a function of the gray level addressed to the LCD. In (a), each curve corresponds to a given input angle $\theta = \theta'(0)$, which sets the range of accessible θ''s (see text for details). The red markers "×" indicate the values of θ'_t and φ_t used in our experiment (they are also specified in Table 1).